SPACE SURVEILLANCE FROM A MICROSATELLITE

Metric observation processing from NEOSSat

SURVEILLANCE DE L'ESPACE À PARTIR D'UN MICROSATELLITE

Traitement d'observations métriques de NEOSSat

A Thesis Submitted to the Division of Graduate Studies
of the Royal Military College of Canada
by

Stefan Thorsteinson, B.Sc.

In Partial Fulfillment of the Requirements for the Degree of
Master of Science in Physics

June, 2017

For Violet

Acknowledgements

I would like to thank my supervisor, Dr. Donald Bédard for taking a chance and introducing me to DRDC, as well as Dr. Lauchie Scott.

Abstract

Thorsteinson, Stefan. M.Sc. Royal Military College of Canada, June 2017. *Space Surveillance from a Microsatellite: Metric observation processing from NEOSSat.* Supervised by Major Donald Bédard and Dr. Robert (Lauchie) Scott.

The Near-Earth Object Surveillance Satellite (NEOSSat) microsatellite is a dual mission space telescope that was launched on 25 February 2013 in a low Earth orbit (LEO) and which was designed to detect near-Earth asteroids and to conduct space surveillance observations. The microsatellite includes a 15-cm aperture optical telescope, two GPS receivers, and a high performance attitude control system. The space surveillance experimental mission, referred to as HEOSS (High Earth Orbit Space Surveillance), is designed to collect metric observations of Resident Space Objects (RSOs) in deep space orbits, primarily in the geostationary region. The HEOSS mission objectives are to evaluate the utility of microsatellites to perform Space Surveillance Network (SSN) catalog maintenance observations of RSOs and to perform optical space surveillance experiments which are difficult to perform from the ground.

An image analysis system was implemented that can automatically process NEOSSat's space-based track rate mode imagery. The image analysis software, known as Semi-QUIck Detection 3rd iteration (SQUID3) uses Fourier processing to identify the characteristics of star streaks in track rate mode images and a matched filter to detect image stars so that astrometry can be performed. The sequence of images taken on a given RSO is then processed in a stack of all frames, shifted to compensate for the RSO's motion between frames so that the signal is additive. Stacked image processing provides a method to reject false positive signals from the energetic cosmic ray background while enhancing the detectability of an RSO when compared to single image processing. Finally, detected observations are correlated against known objects in the SSN catalog.

An imaging campaign of GPS satellites was performed from September

2015 to February 2016 in order to assess the metric accuracy of HEOSS imagery. SQUID3 produced right-ascension and declination observations verified against reference orbits to a mean residual accuracy of 2.8 arcseconds level, meeting accuracy requirements of non-traditional sensors for SSN catalog maintenance.

The theoretical limiting magnitude of HEOSS imagery is presented and then verified from observations. Automated image processing of GPS satellites detected sources down to 15th magnitude. This is equivalent to detecting a 1.7 meter diameter RSO at geostationary range. An imaging campaign on Anik-A class satellites was taken on October 27 of 2015 at a range of solar phase angles. This produced imagery containing sources near and beyond NEOSSat's limiting magnitude. With manual verification of detected sources SQUID3 was able to produce observations down to 17th magnitude.

Résumé

Thorsteinson, Stefan. M.Sc. Collège militaire royal du Canada, juin 2017. *Surveillance de l'espace à partir d'un microsatellite: Traitement d'observations métriques de NEOSSat.* Thèse dirigée par la major Donald Bédard, Ph.D. et M. Robert (Lauchie) Scott, Ph.D.

Le Satellite de surveillance des objets circumterrestres (NEOSSat) est un microsatellite qui a été lancé le 25 février 2013 dans une orbite basse terrestre (LEO) et qui a été conçue pour détecter les astéroïdes à proximité de la terre ainsi que de mener des observations de surveillance de l'espace. Le microsatellite est équipé d'un télescope optique ayant une ouverture de 15 cm, deux récepteurs GPS et un système très précis pour contrôler l'orientation du satellite. La mission expérimentale de surveillance de l'espace, connue sous le nom de HEOSS pour "High Earth Orbit Space Surveillance", est conçue pour prendre des observations métriques de satellites et débris spatiaux ayant des orbites à haute altitude, soit principalement des orbites géosynchrones. Les objectifs de la mission HEOSS sont d'évaluer l'utilité des microsatellites dans le cadre d'une mission de surveillance de l'espace ainsi que de prendre des mesures qui sont soit difficiles ou impossible à prendre à partir d'un télescope situé sur la surface terrestre.

Cette thèse décrit le développement d'un système d'analyse d'image qui traite de manière automatique les données de surveillance de l'espace produite par le microsatellite NEOSSat. Ce logiciel, nommé "Semi-QUIck Detection 3rd iteration" ou SQUID3, utilise en premier temps une analyse de Fourier afin d'identifier les caractéristiques des lignes produites par les étoiles sur les images recueillies par NEOSSat. Par la suite, un filtre adapté est utilisé pour détecter la position précise de ces étoiles à des fins d'astrométrie. La séquence d'images prises pour un objet donné est alors traitée en groupe afin de compenser pour le déplacement de l'objet dans chacune des images. Le traitement d'image en groupe est une méthode efficace qui permit d'améliorer la détection d'objet en orbite terrestre tout en permettant de rejeter les faux signaux positifs qui

sont causés principalement par les rayons cosmiques. Finalement, le logiciel permet d'identifie l'objet détecté par NEOSSat en effectuant un corrélation entre cette détection et le catalogue, d'objets en orbite terrestre, produit par le United States Space Surveillance Network (US SSN).

Cette thèse décrit aussi une expérience d'observation de satellites GPS qui a été effectuée entre septembre 2015 et février 2016 et qui cherchait à évaluer la précision métrique des images produites dans le cadre de la mission HEOSS du microsatellite NEOSSat. Les résultats de cette expérience, obtenus en traitant les images avec le logiciel SQUID3, ont produit des observations métriques en ascension droite et en déclinaison ayant une précision résiduelle moyenne de 2,8 arc-secondes ce qui a démontré que NEOSSat répond aux exigences de précision des capteurs non-traditionnels fournissant des données au US SSN.

Finalement, en se servant des résultats obtenus des observations de satellite GPS, cette thèse présente les limites de détection des images produites produite dans le cadre de la mission HEOSS et les compare aux valeurs théoriques. Les résultats démontrent que NEOSSat peut détecter des objets de 15ème magnitude, ce qui équivaut à détecter un objet ayant un diamètre de 1,7 mètre en orbite géostationnaire. Une autre expérience d'observation est décrite durant laquelle des satellites de classe Anik-A ont été observés le 27 octobre 2015. Les images obtenues lors de cette expérience ont démontré que le logiciel SQUID3 est en mesure de traiter avec succès des images près de la limite de détection de NEOSSat. De plus, avec une intervention humaine, le système fut en mesure de détecter des objets de 17ème magnitude.

Mots clefs: Surveillance de l'espace, observations métriques, traitement d'image, photométrie de satellites, détermination d'orbite, connaissance de la situation spatiale.

Contents

List of Tables

List of Figures

Acronyms

AGI	Analytical Graphics, Inc.
CAF	Canadian Armed Forces
CASTOR	Canadian Automated Small Telescope for Orbital Research
CCD	charged-couple device
CVZ	continuous viewing zone
DEC	declination
DRDC	Defence Research & Development Canada
ECEF	Earth centred Earth fixed
EKF	extended Kalman filter
FITS	Flexible Image Transfer System
FOV	field of view
FWHM	full width at half-maximum
FSS	Find Star Streaks software
GEO	geostationary Earth orbit
HEO	highly elliptical orbit
HEOSS	High Earth Orbit Space Surveillance
GBO	Ground Based Optical
GPS	Global Positioning System
LEO	low Earth orbit
MEO	medium Earth orbit
MOST	Microvariability and Oscillations of Stars
MPS	Mission Planning System
MSX	Midcourse Space eXperiment
NEOSSat	Near Earth Orbit Surveillance Satellite
ODTK	Orbit Determination Toolkit
RA	right ascension
RAAN	right ascension of ascending node
RMS	root mean square
RSS	root sum square
RSO	resident space object

PSF	point spread function
SAA	South Atlantic anomaly
SBV	Space-Based Visible sensor
SGP4	Simplified General Perturbations ver. 4
SBSS	Space-Based Space Surveillance
SNR	signal-to-noise ratio
SPADOC	Space Defense Operations Center
SQUID2	Semi-QUIck Detection 2nd iteration
SQUID3	Semi-QUIck Detection 3rd iteration
SSA	space situational awareness
SSM	star stare mode
SSN	Space Surveillance Network
STK	Satellite Tool Kit
TLE	two-line element
TRM	track-rate mode
UCAC3	US Naval Observatory CCD Astrograph Catalog ver. 3

1 Introduction

Since the dawn of the space age, beginning with the launch of Sputnik in 1957, the near Earth environment as been steadily populated with an increasing number of man made orbiting objects, including active and defunct satellites, rocket bodies and associated pieces of debris. These Resident Space Objects (RSOs), each travelling with orbital velocities on the order of 3 to 7.5 km/s present a requirement to reliably and accurately measure their current positions and forecast future predicted locations in order to ensure the safety of active space assets, the manned orbit regime, and to predict and mitigate the danger of re-entry events.

Space surveillance includes such tasks as detecting and tracking RSOs, as well as cataloguing this information for further analysis. Due to incomplete modelling of atmospheric drag, solar radiation pressure, and asymmetric gravitational influences, the orbits of RSOs must be continuously refined through observations, typically either radar or optical. To keep orbital parameters accurate and prevent errors in cataloguing, observational updates to RSO orbital parameters must be done frequently, with intervals depending on orbit regime, from daily to no longer than a few days. With over 17,800 catalogued RSOs currently tracked [1], and many more added annually, this poses a vast and growing problem that is addressed by a wide and evolving array of sensors to ensure global coverage. The US Space Surveillance Network (SSN) maintains a catalog of all known RSOs, updating their orbital parameters with observations from contributing sensors. These parameters are available world

1

wide in the form of Two-Line Element (TLE) sets and are used by spacecraft operators to determine the timing of station passes and other orbit events.

This chapter will describe optical space surveillance beginning with a description of Earth orbits and their parameters, the force models that govern their motion, and orbits are maintained up to date with observations. Space surveillance sensor types and are described with a focus on optical systems from both ground based observatories and space-based space surveillance sensors.

1.1 Satellite Orbits

Bodies in closed orbits travel in elliptical trajectories. An orbit or 'state' is represented by element sets for which there are two main categories defined by the type of propagator used to determine how a future state determined from the present state [2, pg.103]. To fully describe an orbit at a given time six parameters are needed - either the Cartesian position and velocity or classical Keplerian orbital elements. Classical orbital elements use semi-major axis, inclination, eccentricity, to describe the shape of an orbit, Right Ascension of Ascending Node (RAAN) and argument of perigee to describe how the orbit is oriented about the Earth, and true anomaly to note the current position of the satellite about this orbit. State vectors simply list the Cartesian position and velocity of a satellite in a given reference frame, either the standard inertial frame J2000 where the coordinate system is fixed relative to the celestial sphere, or the Earth Centred Earth Fixed (ECEF) frame which is motionless with respect to the Earth.

Classical orbital element sets use analytical propagators - a new state is calculated from the old state from a set of equations derived from a simplified force model. State vectors require a numerical propagator to integrate the state through time using a detailed force model. The state vector approach is considered more accurate at the cost of increased computation time, while classical elements can be propagated quickly to a reasonable accuracy, useful

for basic satellite tracking tasks such as ground station antenna pointing. State vectors can also provide an estimate of an orbit's uncertainty in the form of a covariance matrix.

The SSN maintains a public catalog of TLEs which contain classical elements, and a limited access catalog of state vectors. The satellite community generally uses TLEs to compute orbital locations, pass times and access considerations. The term Two Line Element is an anachronism from the era of punch cards where it took two 72 character lines to fully list all of a TLE's parameters. The standard analytical propagator designed for use with the TLE format is known as Simplified General Perturbations version 4 (SGP4). It can quickly compute updates to orbital positions taking into account Earth oblateness effects, and observed historic drag behaviour of an RSO. TLEs are generally accurate to within about 1 km at epoch for a non-manoeuvring RSO, growing at about 1-3 km per day depending on orbit regime [3]. Appendix A describes the TLE format.

1.1.1 Orbital Regimes

Earth orbiting satellites typically fall into four different regimes [4], illustrated in Figure 1.1. Closest to the Earth is the Low-Earth Orbit (LEO) regime, populated with satellites with a wide range of missions from Earth observation to communications or scientific exploration, and associated pieces of debris such as rocket bodies. LEO orbits are nearly circular and conventionally extend up to an altitude of 2000 km. Above this is the Mid-Earth Orbit (MEO) regime, populated mainly with navigational satellite systems in inclined circular orbits. Further out, at an altitude of approximately 35,786 km is the Geostationary Earth Orbit (GEO) belt, objects for which have a 24 hour period and near zero inclination, making them appear stationary from the ground. The GEO belt is a highly regulated orbit regime densely populated with active communications and surveillance satellites. The Highly-Elliptical Orbit (HEO) regime consists of objects in geostationary transfer orbits or highly inclined

Molniya orbits, useful for missions involving high latitudes.
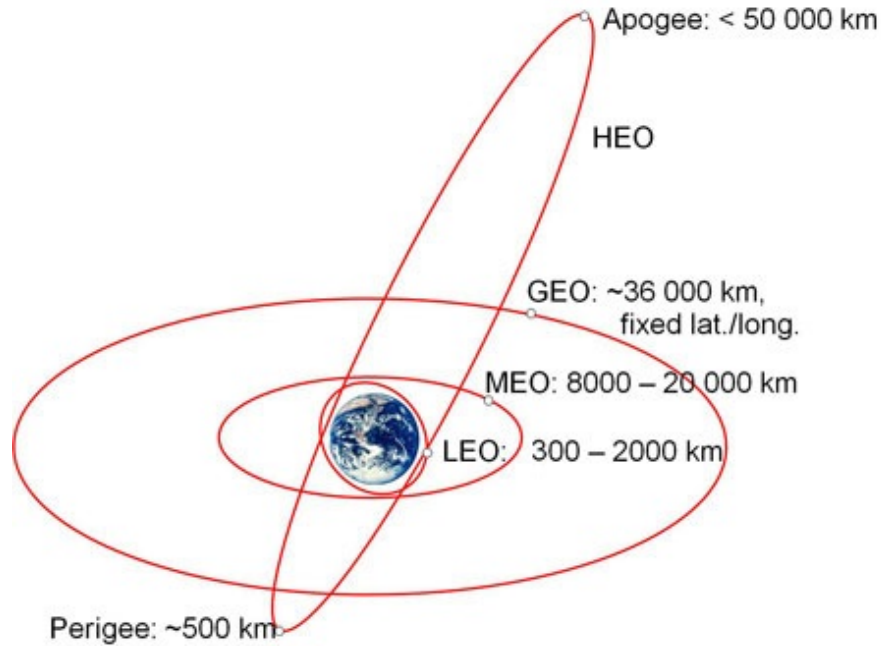
Figure 1.1: Orbit classification for space surveillance.

1.1.2 Orbital Perturbations

Different orbit regimes experience various perturbative influences that deviate an orbit from a simple two body solution. As the Earth is not a perfect sphere of uniform density, all orbit regimes cannot be accurately modelled with simplified two body gravitation. The Earth's oblateness causes motion of a satellite's orbital plane about the Earth. The Earth's non-uniform density and dynamic influences (from tides and a non-solid core) necessitate detailed gravity force models to be constructed for accurate orbit propagation. Third body gravitational influences, such as the Sun and the Moon must also be modelled. For the large part gravitational perturbations are well modelled and do not contribute substantially to orbit uncertainty during propagation.

Some perturbative influences are difficult to model, and their cumulative uncertainties pose a difficulty for space surveillance.

In the LEO regime satellite drag is a major unmodelled influence, with the Earth's atmosphere extending to an altitude upwards of 1200 km, which imparts a ballistic drag force on a satellite. Satellite drag is notoriously difficult to model as there is both a high degree of uncertainty of real time atmospheric densities and also a given satellite's attitude, let alone shape or mass, is typically unknown. This leads to low fidelity ballistic modelling and a propensity for LEO objects to have high uncertainties in their in-track positions (they arrive either early or later along their orbit track) depending on how much drag they experienced.

The MEO and GEO regimes are above the Earth's atmosphere, away from the influence of drag. The dominant unmodelled forces perturbing their orbits in these regimes is solar radiation pressure, which like drag requires a detailed knowledge of satellite attitude and construction to calculate. This force is not symmetric throughout an orbit, and over time, influences changes in an orbit's shape. Objects in HEO orbits experience the perturbative effects of low altitude drag near their perigees, and solar radiation pressure throughout the orbit.

While extensive models exist to account for any of the perturbating forces a satellite may experience a detailed knowledge of their inputs is unknown for the vast majority of RSOs. This necessitates frequent observational updates of every known RSO to be performed in order to ensure acceptable positional accuracy of catalogued elements.

1.1.3 Orbit Determination

As the force models behind orbit propagation are not completely determined, orbits need to be updated over time, or for the case of a newly discovered object, determined initially [2]. For maintenance of a space catalog, one must ensure that the accuracy of provided orbits meet a minimum standard. Propa-

gation errors cannot be allowed to grow to such a size that collision avoidance cannot be prevented, or tracking, whether from a ground station or space surveillance sensor, cannot be performed because the satellite is no longer visible at its predicted location. The position error of the a TLE is on the order of 1 km at epoch [5], and using the SGP4 propagator the error grows at about 1-3 km per day. This error growth rate presents a need to periodically refine and orbit so that an RSO is not too far from its predicted location that it cannot either be tracked or distinguished from other neighbouring RSOs.

An orbit is refined by tracking an RSO, observing its state, whether wholly or in part, and performing corrections to its orbit. The standard technique of orbit update is differential correction, otherwise known as batch least squares [2]. Incidentally, the least squares method has always been linked with orbit determination as the technique was first invented by Gauss to refine the orbit of Ceres.

When a wealth of observational data is obtained on an RSO, the time span over which an orbit is corrected may be large enough that the accuracy of the propagator used over the fit is less than the accuracy of the sensors used in tracking. Because of this, orbits are more accurately refined with an Extended Kalman Filter (EKF), which allows old observations to be discarded as the predicted accuracy of the propagator makes their contribution to the orbit solution detrimental [2]. Furthermore, with an EKF one can model propagator inaccuracy as a stochastic process, allowing for the estimation of unknown parameters such as satellite drag coefficient.

1.2 Observations

Space surveillance can be defined as the general practice of observing objects in orbit [2, pg.242]. This is done with sensors, either ground or space-based, that can measure something about an object in orbit. This section will describe the typical technologies used in space surveillance, with an emphasis on optical telescopes and how they image RSOs.

1.2.1 Sensor Systems and Data Types

Surveillance of space is conducted with a range of sensor technologies, each adapted to a particular role [6]. These include radars, optical telescopes, laser ranging systems, and radio frequency analysis of active satellites (Doppler ranging). Laser ranging is used for ultra precise tracking of calibration satellites, which allows for better modelling of the Earth's gravitational parameters. Radio frequency analysis allows for operators to refine orbits during station passes, but this data is specific to the frequencies and hardware of each payload.

In general, the bulk of surveillance of space data contributing to discovery, detection and cataloguing of RSOs is done by radar or optical sensors. Radar sensors track most of the LEO regime, where high-accuracy range measurements are used to determine orbits. While some of the most powerful radars can detect deep space objects, these are cost prohibitive. As radars are active sensors, which suffer from $1/r^4$ power loss over range, most deep space tracking is done with angles-only measurements derived from optical telescopes.

Optical sensors are best suited at tracking deep space RSOs as at LEO altitudes, RSOs move at high speed relative to the ground. But while radars struggle to reach deeper orbit regimes (Figure 1.1) the slower motion of RSOs make their optical signatures suitable for telescope detection.

This thesis focuses on optical space surveillance for which there are two classes of sensors, terrestrial ground based observatories and orbiting space-based optical platforms.

1.3 Ground-Based Optical Systems

Optical ground based space surveillance telescopes have been employed successfully for many years to detect deep-space RSOs. For example, the US Ground-based Electro-Optical Deep Space Surveillance (GEODDS) system [7] has been providing space surveillance data for decades with observato-

ries spread in equatorial regions around the globe. From a data collection and analysis point of view, a ground based observatory allows for substantial dwell time on deep space RSOs from a fixed observer platform location. Unlike space-based platforms, they are typically not limited by data bandwidth constraints, allowing an abundance of imagery to be taken. Furthermore, the availability of a shutter allows for the routine collection of dark frames, crucial for data reduction of astronomical images containing low signal light sources.

The Canadian Armed Forces (CAF) has a long history of investing and participating in ground based Space Situational Awareness (SSA) activities in support of NORAD commitments. Space surveillance activities in the optical realm began in the 1960s with telescopes at Cold Lake, Alberta and St. Margarets, New Brunswick, whose operations ceased in 1993. These observatories hosted large 0.5 metre Baker-Nunn telescopes with film based imagery. Afterwards, a low cost small aperture observatory was constructed at RMCC, the Canadian Automated Small Telescope for Orbital Research (CASTOR) [8]. This smaller, low cost architecture paved the way for the Ground Based Optical (GBO) [9] network of observatories. These small aperture telescopes proved adept at accurately obtaining metric observations (right-ascension, declination and time) of deep space RSOs. The GBO sensors at Suffield, Alberta and Valcartier, Quebec were used to provide metric data the SSN that was used to update orbital parameters and improve the accuracy of the SSN space catalog.

There are a few factors that limit the effectiveness of ground based optical SSA observatories. As they detect low levels of reflected sunlight, ground based optical systems may only operate at night and need clear skies to make observations. Cloud cover and twilight can prevent observations, while aerosols in the atmosphere reduce the effective sky coverage to higher elevations, typically more than 20 degrees above the horizon. They can also only see RSOs that pass over them during these ideal conditions, constraining the windows of opportunity to detect RSOs in certain orbits. For example a telescope

8

in the southern hemisphere would have difficulty detecting an RSO in a Molniya orbit whose apogee is over the northern hemisphere and travels quickly through the LEO regime on its southern perigee passes. With such constraints in mind, space surveillance requires a network of ground based sensors spread across all longitudes to detect and persistently track every deep-space RSO. Even with a wealth of sensors there is no guarantee that lighting or weather conditions will be suitable for providing observations in a timely matter when the need arises.

1.4   Space-Based Optical Systems

While ground based optical space surveillance systems are highly productive and allow for equipment maintenance and technical updates, there are specific advantages to using a space-based space surveillance platform. An orbiting space-based platform can provide complete sky coverage as its viewing restrictions are dynamic. For a platform in LEO the Earth, Sun and Moon obscure parts of the sky each orbit, but not continuously. As the platform orbits the Earth so do the RSOs to be observed. Viewing geometries for a platform in LEO typically provide multiple daily access windows to deep space RSOs that meet all lighting and relative motion constraints. For a platform placed in a Sun-synchronous orbit an anti-sunward region of the sky containing the geostationary belt is continuously observable. Figure 1.2 shows a sensor platform in LEO and viewing geometries to GEO and Global Positioning System (GPS) orbits, the Earth's shadow shows the general anti-sunward direction and the purple outline is the Continuous Viewing Zone (CVZ) that satisfies all viewing geometry constraints during a full orbit.

As a day evolves, each GEO longitude rotates into this viewing zone allowing for full daily GEO coverage. Furthermore, in anti-sunward directions the relative solar phase angle between the observing platform and the RSO is at a minimum, which maximizes the amount of reflected sunlight back to the sensor, improving the probability of detection of small RSOs. Responsive-

ness to short notice observation requests are independent of weather, and are instead dictated by ground station contact times and orbital alignment.
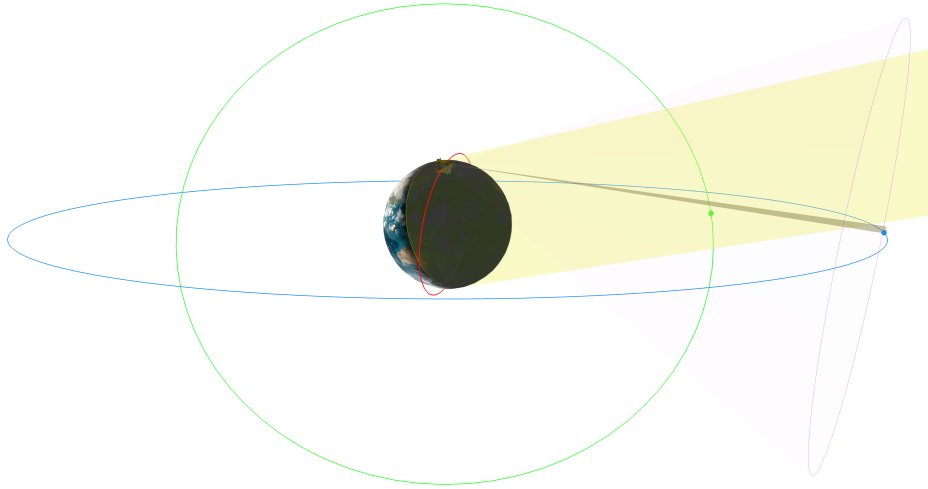
Figure 1.2: Viewing geometry from a LEO (red) space-based sensor relative to GEO (blue) and GPS (green) orbits. Earth shadow indicated in yellow.

1.4.1   Space-Based Metric Data

Angles-only metric observations are usually collected in the J2000 reference frame as Right Ascension (RA) and Declination (DEC) measurements. Right ascension is defined as a celestial longitude relative to the vernal equinox (Figure 1.3), and declination a celestial latitude.

The SSA data product, crucial to updating both the TLE and special perturbations catalogs from space-based optical sensors. is in a format knowns as B3 Type 9, a US Air Force observation format compatible with the SSN SPADOC system [11]. It is a formatted text file containing an entry for each observation that includes: the time and date of observation, RSO SSN catalog number, sensor identification number, right ascension, declination, optionally the range (not typically available for optical observations), and the ECEF
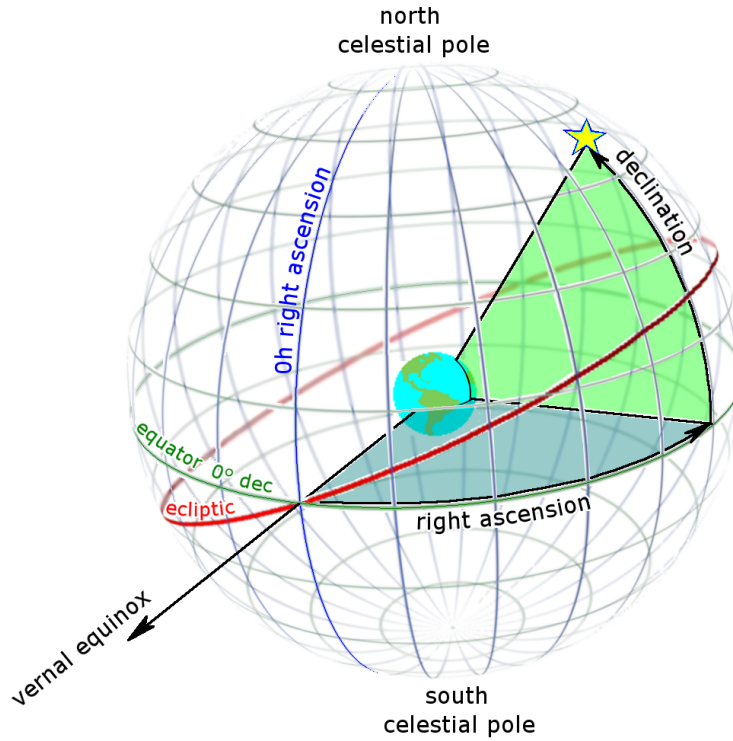
Figure 1.3: The Right Ascension (green) and Declination (blue) coordinate system [10].

reference frame position coordinates of the observing platform. The J2000 epoch used in USAF astrodynamic standards uses an epoch of 31 December 1999 in contrast to the astronomical community standard of 12:00 1 Jan 2000 [12]. This amounts to a small precessional difference that must be accounted for during coordinate transformations.

1.4.2 SBV and SBSS

The US military has been operating space-based space surveillance sensors since 1996, beginning with the Space-Based Visible sensor (SBV) [13] aboard the Midcourse Space eXperiment (MSX) satellite. The SBV sensor consisted of a visible band fixed telescope mounted off-axis on a large bus (Figure 1.4,

left). This configuration restricted MSX to imaging mainly in the geostationary region where large slews between observations could be minimized. That said, SBV provided a significant improvement in all sky geostationary coverage to the SSN and remained in operation until 2008.
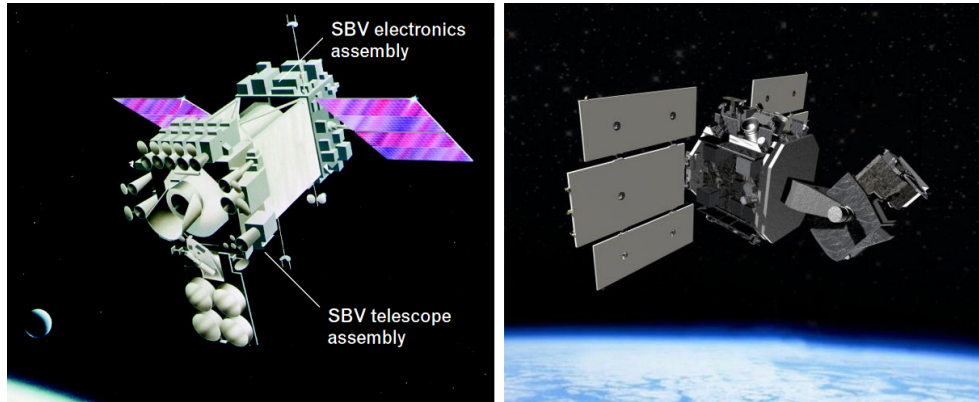
Figure 1.4: The Space-Based Visible sensor on the MSX satellite (left) [13] and SBSS satellite (right) (image credit: Air Force Space Command).

More recently the Space-Based Space Surveillance (SBSS) Pathfinder satellite (Figure 1.4, right) was launched in 2010, with a 30 cm gimballed optical payload capable of tracking RSOs at independent attitude rates from its bus [14]. Space-based sensors are continuing to be viewed for future space surveillance capabilities with the expected 2017 launch of ORS-5 SensorSat mission - a low cost follow on to SBSS, and by the CAF with the Surveillance of Space 2 project, currently awaiting implementation approval.

1.4.3 NEOSSat and SAPPHIRE

February of 2013 saw the launch of two CAF optical space surveillance assets: the SAPPHIRE satellite [15], which began an operational role of providing metric data to the SSN, and NEOSSat (Near Earth Orbit Surveillance Satellite) [16] a research platform designed to investigate the military utility of using a microsatellite for space surveillance activities. NEOSSat (shown after

assembly and just before lauch in Figure 1.5) is an experimental microsatellite space telescope jointly funded, procured and operated by the Canadian Space Agency (CSA) and Defence Research and Development Canada (DRDC) with Microsatellite Systems Canada Incorporated as the prime contractor. The spacecraft were launched aboard an Indian PSLV launcher in February 2013 into a 786 km dawn-dusk Sun-synchronous orbit. SAPPHIRE is a small satellite optical sensor contributing SSA data to the SSN in an operational role. NEOSSat is a microsatellite optical sensor with a non-operational research based SSA mission intended to evaluate the military utility of a low cost platform to perform SSA tasks. Both are designed with agile attitude control systems allowing them perform frequent slews to match the angular motion of RSOs against the background stars, increasing the dwell time of RSOs over a giving region of each image, enhancing their detectability.
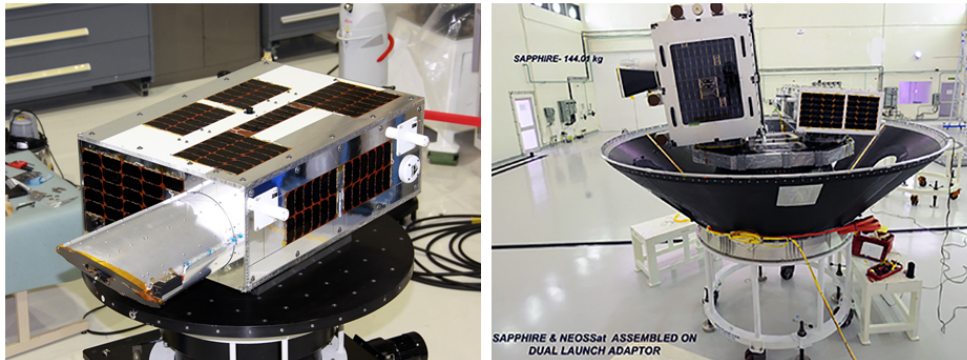
Figure 1.5: NEOSSat at David Florida Laboratory, Ottawa, ON (left). Photo courtesy of Janice Lang, DRDC Ottawa. SAPPHIRE and NEOSSat on the PSLV dual launch adapter (right). Photo courtesy of ISRO.

1.5 Optical SSA Imagery

Raw data from optical telescopes comes in the form of imagery, produced by a Charged Couple Device (CCD). Light sources of interest within the imagery are the RSO being tracked, and the stars in the background. Accurate posi-

tional knowledge of the RSO can be inferred relative to the well catalogued positions of stars through astrometric fitting of an image scene.

1.5.1 Optical Data Types

There are two common methods of tasking an optical sensor to track an RSO. The first is Star Stare Mode (SSM) where a telescope is slewed at the same rate as the background stars, which appear as point sources and the orbiting RSO is left to streak through the image at its current angular rate. Alternatively in Track-Rate Mode (TRM), a the telescope can be slewed to match the angular rate of the RSO, leaving it as an apparent point source while the background stars each appear as a streak of the same length and orientation. Figure 1.6 shows example NEOSSat imagery in both modes, SSM on the left and in TRM on the right.

Figure 1.6: NEOSSat imagery in SSM mode with an RSO streak (left) and in TRM with two RSO centroids (right).

Conceptually TRM is straightforward to achieve when tracking geostationary RSOs from the ground. As geostationary RSO rates are null from an Earth observer, one simply turns off sidereal motion control when pointing at the RSO, and any imagery taken will have the stars streaking through the

image at the sidereal rate of 15 arcsec/s. NEOSSat is designed to be capable of both fine pointing in SSM and fine slewing in TRM at rates of up to 60 arcsec/s. The strengths and weaknesses of imaging in either mode for SSA purposes is discussed in Section 2.2.

1.5.2 GBO Image Processing

While there was well established, robust image analysis software written for the GBO project, the needs of a space-based SSA imaging system differ significantly from those of a ground based system. The data reduction software for the GBO observatories is detailed in [17] and will now be described here. The software's main objectives were to develop an algorithm that detects and distinguishes between the stars and RSOs in a given image. The main algorithm chosen, image segmentation, does this through geometric classification, which sorts light sources in an image in two categories: either circular (stationary) or elliptical (moving relative to the telescope boresight). As an RSO is moving relative to the celestial background then depending on how the telescope was tasked to track (SSM or TRM), either the stars or the RSOs appear streaked. A limitation of image segmentation is that the geometric classification involves a Signal-to-Noise Ratio (SNR) cut-off to create a binary image for signal, any signatures below this cut-off are exempt from the possibility of detection. The potential for cloud cover, and the wish to reduce the probability of false positives in automated processing required a high SNR cut-off which limited the GBO analysis software to detecting RSOs having a bright (SNR > 8) limiting magnitude.

1.5.3 Space-Based Image Processing

For NEOSSat, the motivations for developing an image processing algorithm differed from GBO as it is a space-based platform. Constraints such as a limited time reserved for the HEOSS mission, and the total number of images that could be taken per day dictated by bandwidth and station passes,

provided motivation to find an algorithm that maximizes the detectability of RSOs in all available imagery. Furthermore, as GBO was a ground based system, the images were not routinely susceptible to corruption from energetic cosmic rays prevalent in space-based imagery. A method of distinguishing the random and possibly RSO like signatures of cosmic rays from true observations is lacking using existing methods. To achieve these ends, a new method of image analysis was desired for the HEOSS mission.

1.6 Aim of the Thesis

The primary aim of this thesis is to implement a method to produce metric observations of RSOs from NEOSSat's space-based space surveillance imagery in a manner which maximizes metric accuracy, utilizes all available imagery, and does not produce false positives from the energetic cosmic ray background. Precision metric observations, dependent on platform location information, required precise ephemerides for NEOSSat at all observation times. These were determined from ground processing of measurements made by on-board GPS units. For star detection a matched-filter based algorithm is used, seeded by Fourier transform derived streak signature modelling. For RSO detection an image stacking technique that combines signal in an additive way, from all available imagery and independent of unmodelled spacecraft motion is presented. This method will be shown to both maximize sensitivity through additive combination of RSO signal from all available frames while discriminating from false positive cosmic ray signatures.

The secondary aim of this thesis is to analyse the metric data that were obtained, by comparing NEOSSat observations created with this method to high accuracy reference GPS ephemerides, and thirdly to determine the limiting magnitude of this method by observing very faint RSOs.

1.7 Thesis Outline

Beginning with a technical description of NEOSSat and the HEOSS mission in Chapter 2, the imaging modes of NEOSSat are discussed and a description of a typical NEOSSat imaging sequence is presented.

Chapter 3 is a literature survey including optical SSA architectures with heritage in the CAF, both space and ground based. Their methods of SSA image analysis will be presented and their limitations discussed as applicable to NEOSSat's technical capabilities.

In Chapter 4 the considerations for developing an image processing algorithm given NEOSSat's hardware design, rapidly moving platform location, and lack of a shutter in a high noise environment are detailed. NEOSSat's stability in TRM slewing is analysed from which the metric error budget and limiting magnitude of the sensor are calculated.

Chapter 5 begins with a description of the inputs required to begin image analysis, along with a description of a highly effective method for background subtraction of an imaging sequence, removing thermal noise, column defects, and hot pixels, despite the absence of dark frames. Then a new image processing algorithm is introduced, combining the sensitivity of a matched filter based approach with a signature additive image stacking technique that simultaneously increases the detectability and therefore limiting magnitude of image sequences taken by NEOSSat while rejecting false positive cosmic ray signatures from the energetic space environment which appear randomly in an image. The full process of proceeding from raw NEOSSat images to measured RSO positions correlated with known RSOs in the SSN catalog is presented.

The metric accuracy of NEOSSat is analysed in Chapter 6, with results from several months worth of imaging campaigns focusing on GPS satellites. Highly accurate GPS ephemerides are used to measure the residuals from NEOSSat observations and their bulk statistics are presented and discussed. The limiting magnitude of NEOSSat is assessed from imaging campaigns on smaller Anik-A class geostationary satellites. These satellites were imaged

at a wide range of solar phase angles to vary their brightness and determine NEOSSat's detectability cutoffs.

Chapter 7 concludes this thesis with a summary of the results presented, discussions of possible unmodelled influences affecting the results and recommendations for future work to improve quality of observations produced with a microsatellite space surveillance sensor.

2 NEOSSat Mission and Spacecraft

In this chapter a summary of NEOSSat's dual science missions and technical capabilities are presented, with a focus on details relevant to space surveillance operations.

2.1 NEOSSat Mission

The NEOSSat satellite is classified as a microsatellite, massing only 74 kg and is approximately 1.4 x 0.8 x 0.4 meters in size. Built on a small inexpensive bus, NEOSSat was designed as a research platform adhering to the microsatellite philosophy. NEOSSat's payload is a 15cm Maksutov Cassegrain telescope [18] (Figure 2.1, left), sharing bus heritage with the MOST microsatellite telescope [19], but modified with its payload integrated along a different body axis to allow for imaging at low solar elongation angles, and uses field flattening optics. Precise fine pointing attitude estimation is achieved with a star tracker which shares the same focal plane as the science instrument, this controls reaction wheels providing 3-axis stability [20]. NEOSSat has two primary missions: asteroid detection, dubbed Near Earth Space Surveillance (NESS), and the High Earth Orbit Space Surveillance (HEOSS) mission. The HEOSS mission conducts SSA experiments by tracking satellites in deep space orbits (from mid-Earth orbit to GEO), with a goal to evaluate the suitability of a

microsatellite platform adapted to this job [21].
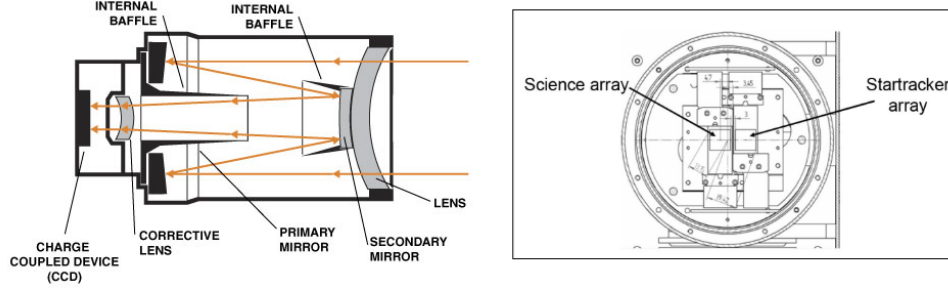
Figure 2.1: NEOSSat's Optical Configuration: Maksutov Cassegrain telescope (left) and Dual CCD locations (right) [18].

NEOSSat was designed to be a nimble telescope platform, slewing to a new section of the sky every few minutes, either sunward for NESS fields or anti-sunward for HEOSS tracks. Its downlink budget called for the ability to take up to 288 images a day [21], each day typically devoted primarily to either mission to avoid frequent large slews. To achieve both the NESS and HEOSS science missions NEOSSat had to meet several design requirements, the relevant ones to this thesis are listed in table 2.1.

Table 2.1: Selected HEOSS mission design requirements.

Quantity	HEOSS Requirement
Sensitivity	Limiting Mag of 13.5 Mv of streaked RSOs moving at 60 arcsec/s
Field of View	> 50x50 arcminutes
Pixel Size	3 arcseconds
Optical Point Spread Function	< 1.5 arcseconds measured at full-width half-max
Pointing stability	0.5 arcseconds 1σ over 100 seconds
Image transfer time	< 15 seconds

Some of these requirements were met through the telescope and CCD detector selection, while others required state of the art attitude control and determination software integrating all of NEOSSat's flight instruments.

NEOSSat's sun-synchronous polar orbit offers an excellent vantage point for imaging deep space RSOs, as a region of the geostationary belt is contin-

20

uously viewable for an entire orbit, and the entire geostationary belt orbits through this region on a 24 hour period. From NEOSSat's orbiting altitude of 786 km, the Earth takes up a region of 125 degrees in angular diameter of the viewable sky. In practice, NEOSSat's boresight is kept a minimum of ten degrees above the Earth limb to minimize stray light from the atmosphere. In addition to this obscuration NEOSSat's pointing is kept at least 45 degrees away from the Sun, which is straightforward for HEOSS's anti-sunward tasks. It is also kept at least 6 degrees away from the Moon and 3 degrees away from bright planets - Venus through Neptune.

2.1.1 NEOSSat Telescope and CCD Characteristics

NEOSSat's optical telescope is a 15cm diameter Maksutov Cassegrain design with two identical CCDs sharing the focal plane (Figure 2.1). One CCD is used for science purposes, while the other CCD is used as a star tracker to maintain arcsecond level pointing stability. NEOSSat's science detector, is an E2V manufactured back illuminated frame transfer CCD, model CCD47-20 [22]. Each pixel is a square of 13.3μm size with a peak quantum efficiency of 45% at 700 nm. Its unmasked imaging area is 1056 by 1030 pixels. Each pixel has a 3.0 arcsecond scale at the prime focus of the $f/6$ NEOSSat telescope giving an effective Field Of View (FOV) of 52.8 by 51.5 arc-minutes. The digitization for each pixel is performed at 16 bits. For scientific data acquisition, NEOSSat's CCD was tasked to either run in full frame 1x1 binning (1056 by 1030) pixels, or in 2x2 binning (528 by 515) pixels, where each binned pixel value is the sum of four unbinned pixels. Running in 2x2 binning has the advantage of a faster image download time from the CCD, which is about 21 seconds in 2x2 binning compared to 84 seconds in 1x1 binning.

Figure 2.2 shows the location of NEOSSat's payload and some instruments relative to the body frame axes. Note that the telescope is directly along +X axis (with the science CCD offset by 0.035 degrees from the centre of the telescope boresight. NEOSSat's largest solar arrays are on the -Z and -X

panels, which are kept pointed towards the Sun while the +Z panel has the payload radiator which cools the CCDs to below -30 degrees Celsius. When NEOSSat is commanded to point at a given look angle the spacecraft roll is selected to maximize the -Z panel exposure to deep space. In anti-solar HEOSS imaging the -X panel is mostly illuminated and the spacecraft roll is selected such that the instrument radiator avoids the Earth, maintaining low thermal dark current on the CCD.
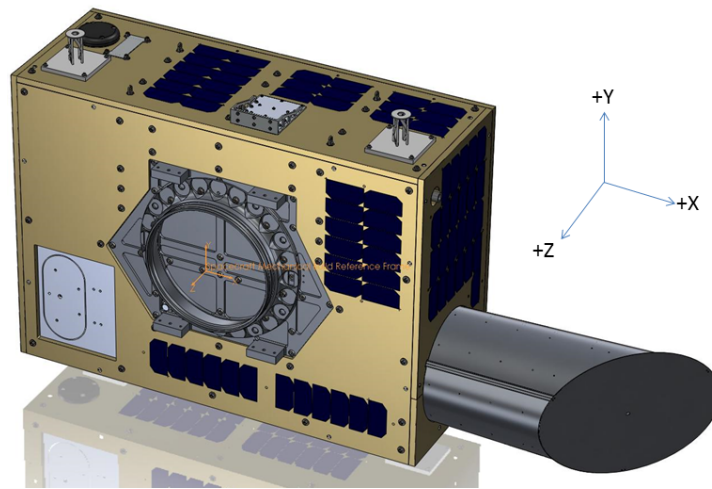
Figure 2.2: NEOSSat satellite body frame axes definition (image source: CSA).

2.1.2 On Orbit Performance

In an attempt to minimize costs a decision was made to use the flight spare CCDs from MOST. A technical assessment of the CCDs was conducted and concluded that the CCDs were still acceptable for the science team's needs. The telescope optics were tested separately from the CCDs and read-out electronics. Due to delays in the design and build of the spacecraft payload, the CCDs were originally tested using temporary, MOST derived, read-out electronics while the final read-out electronics were inserted into the testing late

in the project. The telescope, baffle, CCD, and read-out electronics were integrated only a short time before the imaging system as a whole was itself integrated into the spacecraft. To meet NEOSSat's launch date end-to-end testing of the fully integrated imaging system was conducted on orbit.

Once launched, NEOSSat's imaging performance experienced elevated readout noise levels that were not present during ground testing. This was thoroughly investigated and found to be caused by interference from NEOSSat's switching power supply inducing noise into the read-out electronics. To address this problem an intricate readout timing procedure was developed [23]. This procedure clocked the readout at frequencies which minimized the induced noise. To further reduce readout noise to acceptable levels the read-out electronics were programmed to read each pixel twice and average the result. This introduced a prolonged image download time to internal memory, with a full image taking 83 seconds to readout and a 2x2 binned image 20 seconds. NEOSSat's star tracker CCD suffered the same limitations, which meant that significant delays were experienced in achieving fine pointing of the satellite as an acceptable combination of frame rate, binning and noise cut-offs had to be found before NEOSSat's fine pointing and fine slewing algorithms could be fully tested.

In the first two years on orbit NEOSSat remained in a commissioning state, its operations managed by the CSA. Flight software was written incrementally, with a focus on ensuring spacecraft health while the science teams were engaged to evaluate imagery and stability performance. In September of 2015, after considerable effort, the operations team at the CSA completed and uploaded to the spacecraft flight software that allowed NEOSSat to reliably achieve fine point and perform fine slews meeting most of HEOSS's design requirements. This flight software was referred to as OPS6 and marked the beginning of data collection used in this thesis.

To compromise the on-board reality of NEOSSat's instrumentation with the limited lifespan of the spacecraft, the decision to proceed with HEOSS

imaging campaigns with the performance delivered by OPS6 was made. The main requirement impacted was the full frame image download time, increased from 15 seconds to 83 seconds (Table 2.1). This had significant impact on the length of TRM sequences that could be imaged without breaking fine slew and re-centering an RSO in the FOV.

The other requirement that was relaxed was the Point Spread Function (PSF) of under 1.5 arcseconds. The measured PSF on orbit was closer to 6 arcseconds under ideal conditions [24]. Furthermore, NEOSSat was seen to experience temperature dependent focus distortion at low satellite bus temperatures [24], despite its athermal design. Figure 2.3 illustrates an extreme example of this defocus, showing the signature of a bright star in a reasonably focused state, and in a completely defocused state.
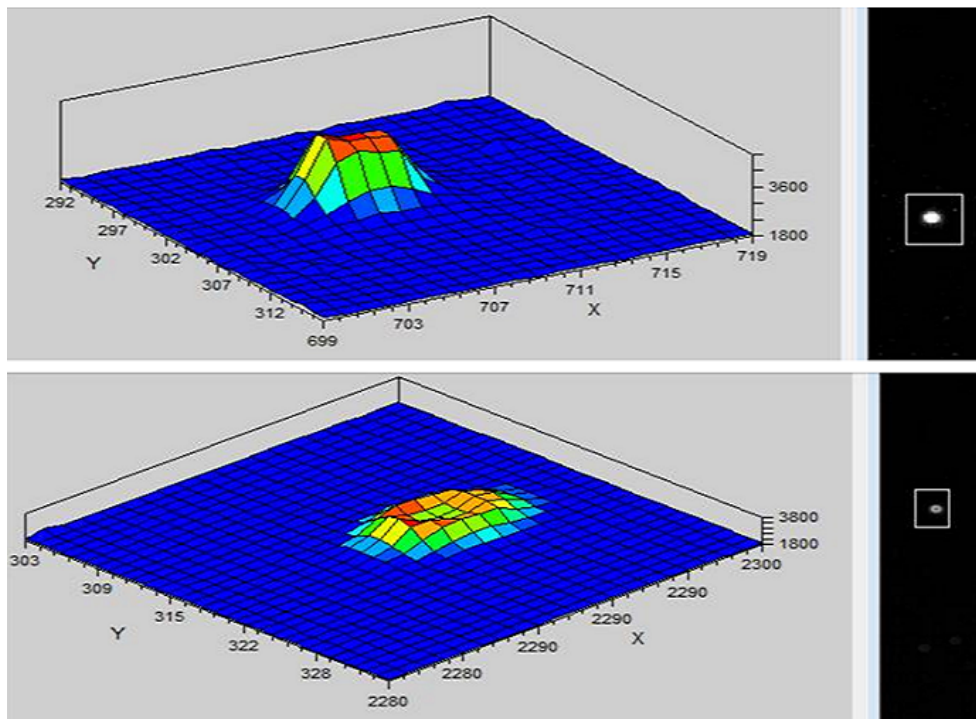
Figure 2.3: On-orbit focus levels of a bright star in a normal temperature configuration (top) and a completely defocued state (bottom).

This increased the effective PSF, mainly in anti-solar pointing directions, typical for HEOSS imaging where a smaller profile of the spacecraft is illuminated by the sun, lowering the overall bus temperature. From a detectability standpoint this defocus had a minimal impact as oversampled pixels are preferred for centroiding point source objects in NEOSSat imagery. From an automated image processing perspective, the PSF had to be modelled independently for each image (see Section 5.3).

2.2 HEOSS Imagery

HEOSS uses two imaging modes, Sidereal Stare Mode (SSM) and Track Rate Mode (TRM). In SSM NEOSSat is pointed at a fixed right-ascension and declination in the sky, and an RSO is left to streak across an image while the stars appear as fixed points. Right-ascension is analogous to celestial longitude in the inertial frame while declination is analogous to celestial latitude. In TRM NEOSSat is slewed to match the apparent motion of an RSO, which results in streaked stars and a point source RSO. Figure 2.4 shows examples of NEOSSat imagery of geostationary satellites in both imaging modes. There are pros and cons to each approach. SSM mode has the potential benefit of simpler attitude control during imaging as the satellite can set up and maintain an inertially fixed attitude without having to control a rate relative to the stars. SSM mode also has additional flexibility in being able to search an area of sky for unknown objects or RSOs with poorly known orbits where detected streaks signify their existence.

TRM imagery has the chief advantage that it maximizes the signal-to-noise ratio of RSO signatures on the detector, but requires a-priori trajectory information of the target object. Since the telescope follows the RSO during imaging, signal accumulates in a smaller area on the CCD relative to the more thinly distributed signal in RSO streaks resulting from SSM imagery. Higher SNR leads to more accurate RSO position determination, as well as better estimate of the RSO photometric brightness.
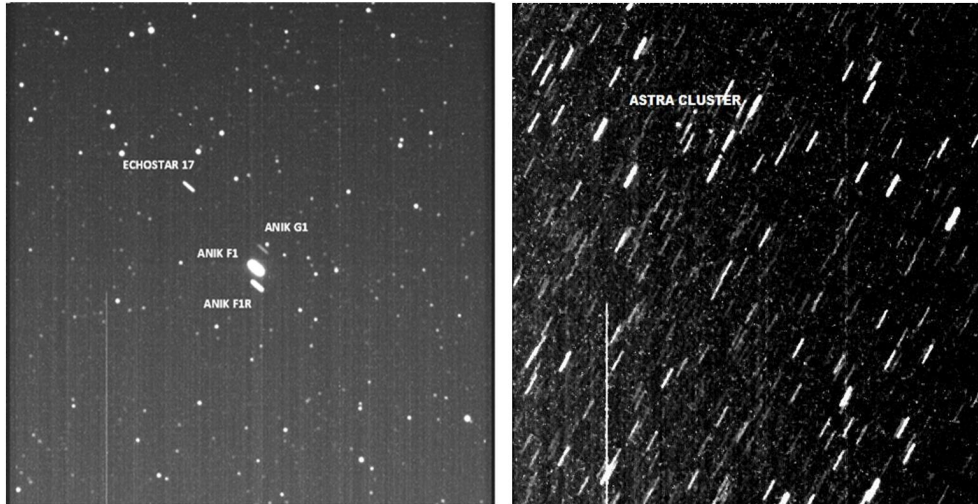
Figure 2.4: The first satellites intentionally imaged by NEOSSat (left) in SSM mode. The Astra cluster of geostationary satellites imaged in TRM mode (right).

SSM imagery was the primary observation method for the NESS mission, and was used by the HEOSS team for photometric calibration of the NEOSSat instrument using Landolt star fields [25]. For SSA data, HEOSS imaged nearly exclusively in TRM, as SSM metrics are less reliable due to streak endpoint uncertainties and the limiting magnitude is much lower (Section 4.4).

3 Literature survey

Several methods of image analysis with heritage in the Canadian SSA community were investigated for applicability to the unique challenge of reducing NEOSSat imagery to RSO observations. This chapter will discuss past and current optical systems, both ground and space-based, as well as the methodology and algorithms underlying how their imagery was analysed. The applicability of these algorithms to NEOSSat imagery, which is acquired primarily in TRM, will be discussed and an approach to processing images automatically will be proposed.

3.1 Ground Based SSA Imagery Analysis

Space surveillance imagery analysis techniques from two ground based systems were developed at RMCC and DRDC. At RMCC, the CASTOR observatory was constructed in the 1990s, and it eventually paved the way for the GBO network of Canadian space surveillance observatories that were built and operated by DRDC and ultimately contributed data to the SSN [9].

3.1.1 CASTOR Image Analysis

Analysis algorithms were written to process CASTOR sidereal stare imagery with RSO streak detection based on the Hough transform method [26]. The Hough transform is a line detection method that can locate streaks in an image. Linear features in an image can be thought of as traditional lines

with a slope (m) and intercept (b). The Hough integral transform takes an (x, y) image and transforms it into a line space (m, b) [27]. Regions of an image matching a linear profile will show up as maximums in the Hough transformed image and are easily detected.

For CASTOR data analysis the Hough transform was used to detect the trailing signature of any RSO moving through an image. While useful for line detection, the Hough transform is not maximally sensitive compared to other algorithms, and for space-based imagery the Hough transform method would not discriminate from elongated cosmic ray hits or CCD column or horizontal noise defects. While an effective detection method for SSM RSO streaks, the Hough transform is ill suited to detect a large multitude of star streaks in a TRM image as their parallel and often overlapping nature would obscure localisation. That said, the closely related Radon transform [27] is used to detect linear features of intermediary processed images in this work.

3.1.2 GBO Image Analysis

GBO consisted of two observatories located at Suffield and Valcartier, operationally contributing SSA data to the SSN [9] and a research observatory [28] (located at DRDC Ottawa). GBO took optical imagery of deep space RSOs, primarily in TRM, and converted their detected signatures into metric data that was then forwarded to the SSN. This data is known as 'angles only' as it does not contain range, and consists of RA, DEC and time measurements in topocentric coordinates from each site. The image processing software used an image segmentation technique that was developed by Wallace [17], and was named Semi-QUIck Detection 2nd iteration (SQUID2).

Image segmentation provides a fast and straightforward method of determining the centroids of stars and streaks in a given image. It is the process of partitioning an image into multiple connected segments from a binary image. The binary image has pixels above a noise floor cut-off set to 1 and 0 everywhere else. Each segment can be scrutinized geometrically to see if it matches

an expected signature. For TRM imagery this would be either a streaked star with high ellipticity or a round RSO. Figure 3.1 shows a background removed GBO image along with its binary segmented image. The streaked stars in the binary image will only be detected if they are contiguous, which only applies to the brighter stars in the image.
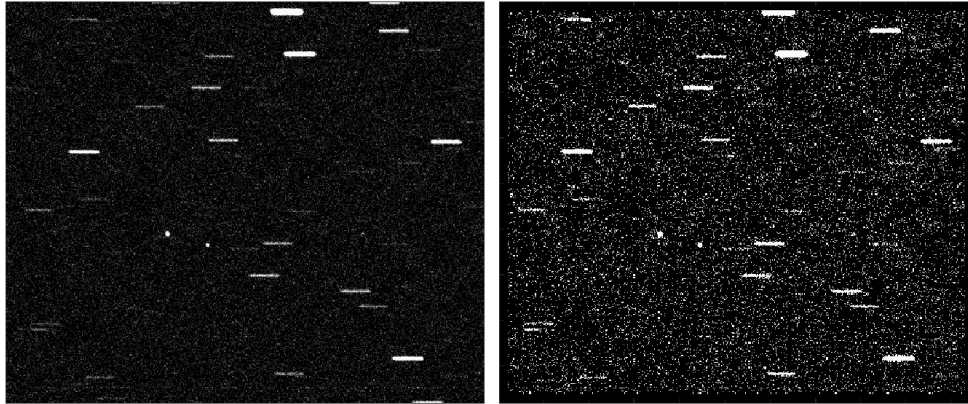
Figure 3.1: A sample GBO image in Track Rate mode (left) and its binary cut-off image (right).

The methodology for the software development SQUID2 according to [17] was focused on rapid development with frequent testing on new imagery as it became available. An emphasis was placed on the quality of the metric data, and the false alarm rate. While a lower priority has been the sensitivity and photometric accuracy of the system.

These priorities are in conflict with data from a space-based system, especially from a microsatellite with a limited lifetime. Such drawbacks, combined with SQUID2's high SNR cut-off, motivates a search for a better method of image processing for HEOSS. In order to maximize the probability of detection on every single image the image segmentation technique used for GBO imagery is not well suited for space-based detection. Image segmentation fails when too few stars are visible, and when the RSO signature is not significantly geometrically different from a star signature. For NEOSSat, a far more

sensitive algorithm for streak detection is needed, one that minimizes both the amount of images discarded from failed astrometric calibration, and also RSO SNR detection cut-off. Furthermore, as GBO was a ground based system its images were not routinely susceptible to corruption from energetic cosmic rays prevalent in space-based imagery; these signatures would be segmented in a similar way as RSOs and be difficult to discriminate. That said, image segmentation is used when appropriate in sub-routines implemented in this thesis, but not as the sole source extraction method.

3.1.3 DRDC Valcartier Streak Detection

At least two image detection algorithm were developed between 2005 and 2010 by Lévesque ([29], [30]) at DRDC Valcartier with a focus on maximizing signal extraction sensitivity. The Satellite Streak Detection [29] software package was developed to process SSM imagery using a matched filter algorithm. This integral transform based method allows one to detect very faint signatures. A properly tuned matched filter has the ability to extract extended streaked signals below an SNR of 2, provided one supplies the expected length and orientation of the streak(s) a-priori. For sidereal stare imagery the length and orientation can be calculated by propagating the RSO's available TLE to the observation time and computing the expected arc length and orientation of its motion during the image exposure interval in the image plane.

A similar technique for SSM imagery was developed by Koblick et al. [31] for future US space-based space surveillance sensors. In this technique a series of SSM images is analysed and a combination of image segmentation and a Fourier analysis approach, used to detect the repetitive streaked RSO signatures. This technique removes the requirement of a matched filter which needs the streak orientation a-priori.

The second technique developed by Lévesque [30] was focused on processing TRM imagery where a method of determining star streak length and orientation without knowledge of RSO TLE motion was created. As the multitude

of stars in a given TRM image all have the same streak length and orientation, a 2D Fourier transform of the image produces a pronounced profile relating to these streak parameters that can be detected in a straightforward manner. Details of the mathematics involved are presented in Chapter 5.3. This method is well suited to star detection in NEOSSat TRM imagery, for even though the RSO's TLE can be accurately propagated, there are no guarantees the NEOSSat's attitude determination and control system performed without error during a track. Having a method that can predict star streak length independent of NEOSSat's rates would further maximize the amount of detected stars, improving the chance an image gets solved for astrometry, and the astrometric solution quality.

3.2 Imagery From a Space-Based Sensor

As NEOSSat is a space-spaced sensor, it does not suffer from the typical imaging constraints and artefacts of a ground based observatory such as cloud cover or atmospheric attenuation. The dominant limiting factors are CCD noise, cosmic rays, and stray light from off axis sources. NEOSSat's tight point spread function makes RSO signatures difficult to discriminate from cosmic ray hits perpendicular to the CCD plane.

While energetic cosmic rays are present throughout the space environment they are particularly intense over a region of the Earth known as the South Atlantic Anomaly (SAA) [32]. Figure 3.2 shows two 1 second exposure NEOSSat images, taken while outside the SAA (left) and on taken directly above the SAA (right). The left frame is a dark frame (no stars visible), the only signatures present are a couple of cosmic ray hits as artefacts larger than one pixel and several single hot pixels. This is a typical level of cosmic ray artefact corruption seen in most HEOSS imagery. The right image in Figure 3.2 was taken in SSM and should have stars visible but cosmic rays have badly corrupted the image making stars indistinguishable from cosmic ray hits.

The image in Figure 3.2 represents an extreme case of the presence of
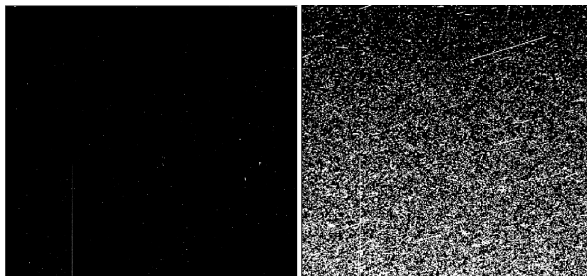
Figure 3.2: Two 1-second exposure frames taken outside the SAA (left) and over the SAA (right).

cosmic rays, however they are likely to be found in virtually every image collected by the NEOSSat sensor especially since the fixed readout time of NEOSSat science CCD is prolonged and independent of exposure duration. This is why the bottom of the corrupted image in Figure 3.2 contains more visible cosmic ray hits than the top, as the image is read from the top to bottom by the CCD's analogue to digital converter. Figure 3.3 shows the rate of cosmic ray corruptions encountered by SBV during a transit of the SAA. While a hundred fold production rate is seen through SAA passes, cosmic ray hits are still present randomly outside the SAA. A procedure for mitigating false positive observations from cosmic ray hits is one of the core motivations in the development of NEOSSat's image processing algorithms.

In SBV imaging, which was done primarily in star stare mode, a fast sequence of short exposure images were accumulated at a single viewing angle [33], and on-board processing was used to create a stacked image. At these short exposures the RSOs in any given image would be difficult to differentiate from a star source thus the entire sequence, framed at 16 times per second, was stacked in order to produce an image with a streaklet that could be effectively processed. This streaklet would have a portion of its signal in each individual frame, allowing for the discrimination of cosmic ray hits that did not satisfy this criteria [34]. As NEOSSat lacks the the ability to download raw images at high speeds, taking approximately 90 seconds for a full readout, this approach

is unsuitable for its image processor.

Susceptibility to cosmic rays from a space-based sensor was addressed by the Hubble team for wide field astronomical imagery in [35]. The Hubble team dealt with cosmic ray hits by combining images of the same field over multiple orbits, and then using a clipping algorithm to reject pixels corrupted by elevated signals far from their median value, indicating the presence of a cosmic ray hit. For NEOSSat, a similar approach is proposed where all images in a TRM sequence be stacked in such a way that the RSO signature is present at a common pixel location in all images (without being detected a-priori). Then all signals in the stacked image can be investigated for persistence throughout the sequence. Random cosmic ray hits would not appear in every image at the same location, allowing their signatures to be discarded safely.
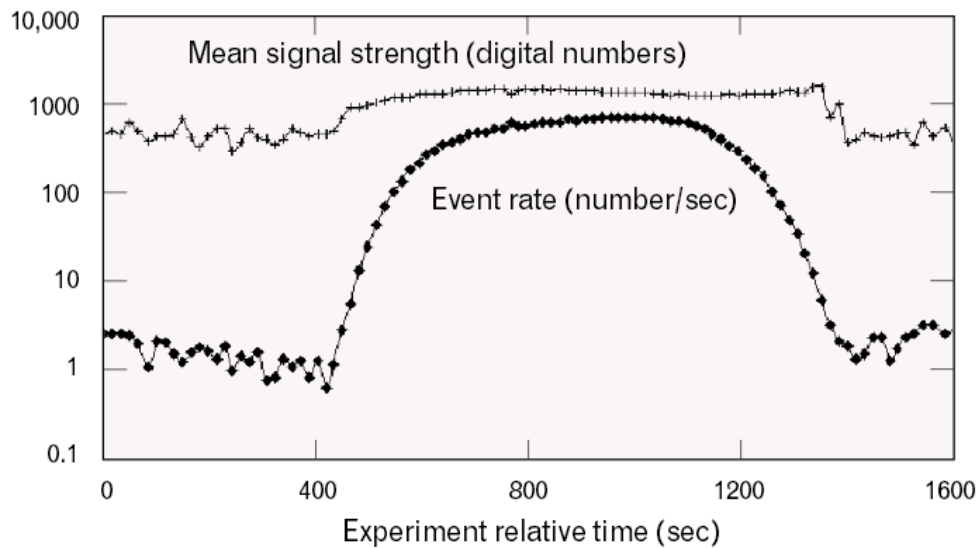
Figure 3.3: SBV image radiation events through the one pass of the SAA [13]. In this experiment SBV entered the SAA at about 420 s, exiting at 1400 s.

3.3 SSA Observations With MOST

The Microvariability and Oscillations of Stars (MOST) [19] microsatellite is a CSA mission that uses a spaced based optical platform to perform long term photometry of stellar sources. While designed for astronomy purposes, in October 2005 the MOST microsatellite was used in an space surveillance experiment by the HEOSS science team to image two GPS satellites in SSM [36]. The goal of this experiment was to test the feasibility of acquiring SSA imagery with a microsatellite. This experiment was used to validate that the NEOSSat mission objectives were attainable since the MOST and NEOSSat satellites share a common design [21]. This experiment was the first ever example of a Canadian satellite telescope taking space-based space surveillance imagery.
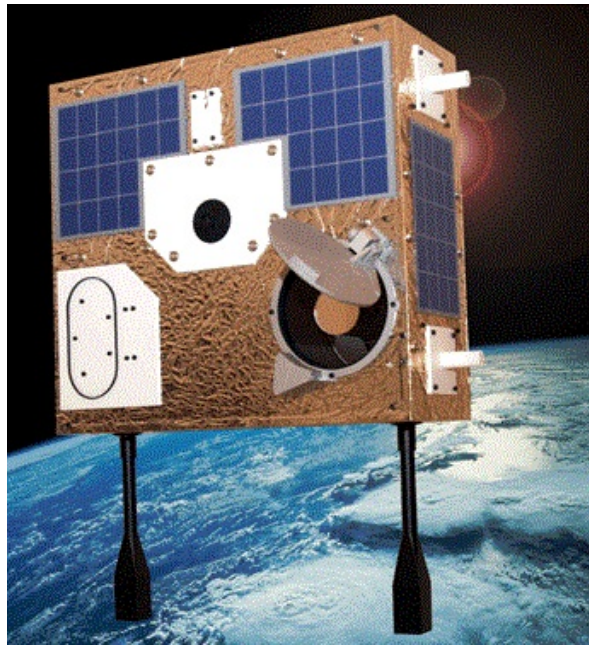
Figure 3.4: The MOST microsatellite (image courtesy of MSCI Inc.).

While MOST shares a telescope design and an identical science CCD with

NEOSSat, MOST was not designed to take full frame imagery and only a portion of the CCD frame was available, in a special engineering test mode, to acquire images. Nonetheless, on two attempts GPS satellites were successfully imaged with MOST (Figure 3.5). The two satellites imaged were Block IIR type GPS satellites.
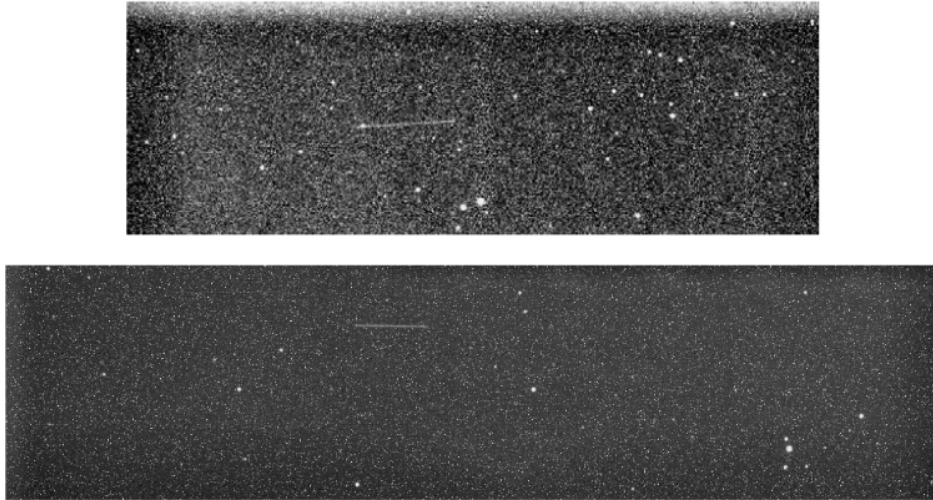
Figure 3.5: Imagery of two GPS satellites taken by MOST. SSN IDs of the GPS satellites are 28190 (top) and 26360 (bottom) [36].

Both of these images were able to be solved for astrometry and metric observations were produced by determining the coordinates of the endpoints of both streaks, resulting in four RA, DEC and time measurements. These measurements were subsequently compared with high precision GPS ephemerides to compute residuals (Table 3.1). The standard deviation (σ) of the four measurements were 5.4 arcseconds in RA and 11.8 arcseconds in DEC. While higher than SSN standards permit, this error was mainly due to uncertainty in the timing of the observations [36]. More precisely, MOST's on board clock is not fine tuned down to millisecond accuracy as this is not a requirement for its precise photometric astrosiesmology mission. The timing uncertainty was estimated to be approximately 0.1 seconds, which would result in an along

track error of about 8 arcseconds in the first track and 4 arcseconds for the second. The apparent magnitudes of each satellite were measured to be 12.1 and 11.5 respectively, consistent with ground based measurements of Block IIR GPS satellites [37].

Table 3.1: Residual metric accuracy of Oct. 2005 MOST observations [36].

Observation	Δ**RA (arcsec)**	Δ**DEC (arcsec)**
1st - 28190	-8.2	-6.0
2nd - 28190	2.1	15.3
1st - 26360	-9.9	-12.2
2nd - 26360	-2.9	0.9
Sigma	5.4	11.8

NEOSSat and MOST share the same Attitude and Control Determination System (ACDS) and this experiment was used to validate that the microsatellite ACDS system and imaging optics held technical promise for use in an SSA mission.

3.4 Space-Based Metrics

The SBV sensor was calibrated to provide operational quality angles only data to the SSN. A review of metric budget analysis and observation formation of SBV data is available in [38]. SBV's goal was to derive streak start and end point observations from SSM imagery with 4 arcsecond total metric accuracy. The post launch error budget for SBV is presented in Table 3.2. Its total error σ_{tot} is computed as the Root Sum Square (RSS) of the each contributing error component:

$$\sigma_{tot}^2 = \sigma_{ephemeris}^2 + \sigma_{timing}^2 + \sigma_{boresight}^2 + \sigma_{SEP}^2 \tag{3.1}$$

where the uncertainties are from SBV's ephemeris ($\sigma_{ephemeris}$), image exposure timing (σ_{timing}), the pointing of the telescope boresight ($\sigma_{boresight}$), and the selection of RSO streak endpoints (σ_{SEP}).

Table 3.2: SBV post launch error budget [13].

Error source	Nominal σ (arcseconds)
Ephemeris, 15 m	1.0
Timing, 1 ms	0.06
Boresight pointing	0.7
Streak endpoint detection	1.2
Total RSS error	1.7

SBV's metric calibration was done by comparing its observations to SSN precision orbits of GLONASS, GPS and LAGEOS satellites. Figure 3.6 shows the residuals from SBV observations of GLONASS satellites [13]. Figure 3.7 shows residuals to one GLONASS satellite broken down into RA and DEC components. NEOSSat's metric accuracy analysis will be presented in Chapter 6 by calculating the residuals between its B3 type 9 data and precision GPS ephemerides.
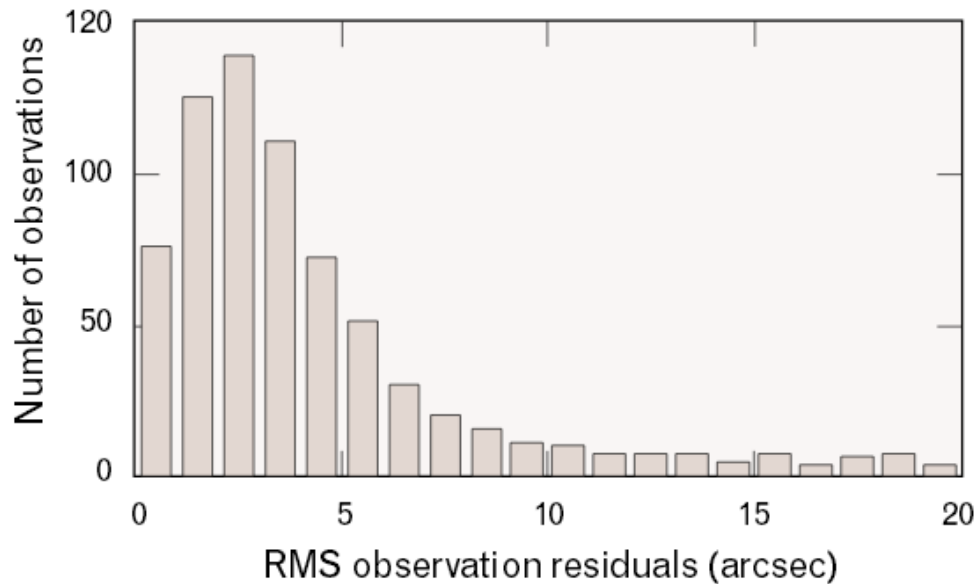
Figure 3.6: Metric residual histogram of SBV observations of GLONASS satellites [13].
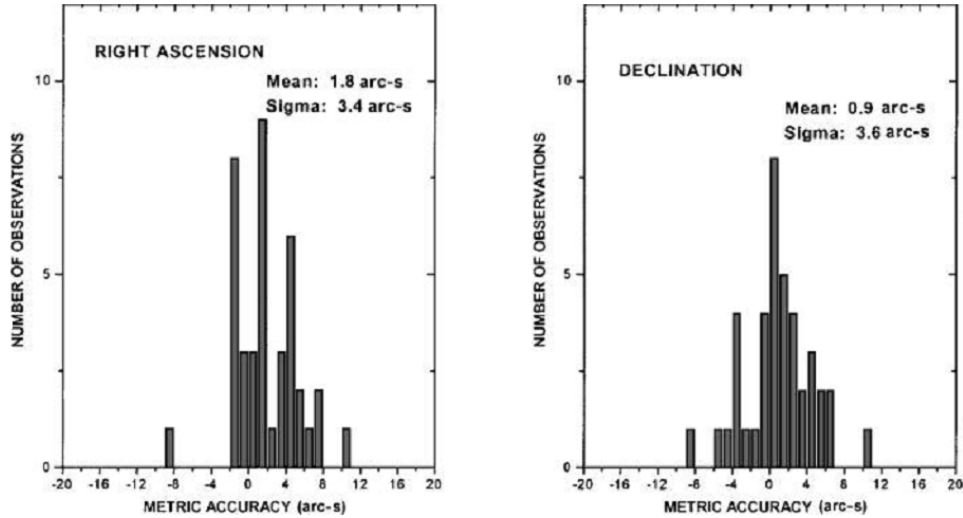
Figure 3.7: Metric residual histogram of Right Ascension (left) and Declination (right) for SBV observations of GLONASS satellite SSN# 23511 [38].

Despite a less sensitive sensor, NEOSSat has the advantage of having a smaller pixel scale of 3 arcseconds than SBV's 12 arcsecond pixels. Initial published metric assessment of SBV observations of GLONASS satellites indicated 1σ accuracy of 4.6 arcseconds [13], that is 68% of observations fall below this level. NEOSSat's on-board GPS sensor should also allow for better ephemeris generation, thus less observer platform position uncertainty than the station pass Doppler-range determined ephemerides produced for SBV. SBV's ~15 m position error created an uncertainty from 0.07 arcseconds at a geosynchronous range of 42,000km to 1 arcsecond for an RSO at a 3000 km range. Furthermore NEOSSat's GPS sensor combined with the E2V rapid frame transfer CCD allows for millisecond accuracy in the time tags of observations. For the characteristic angular rates of NEOSSat (0 to 60 arcsec/s during tracking, see Section 4.1.1) this would account for a maximum of 0.06 arcseconds of error.

3.5   RSO Detectability and Limiting Magnitude

The brightness of a celestial object, independent of its angular size and the imaging sensitivity is measured on a logarithmic scale of magnitudes. The visual magnitudes of RSOs (M_v)s, behave different from stellar objects in that they result from reflected sunlight, and thus vary in intensity with changes in RSO attitude and observing geometry. The Sun-RSO-observer geometry is illustrated in Figure 3.8, with the phase angle defined as the angle between the vector from the observer to the RSO and the RSO's Sun vector. The phase angle is responsible for large changes in the apparent visual magnitude of an RSO.
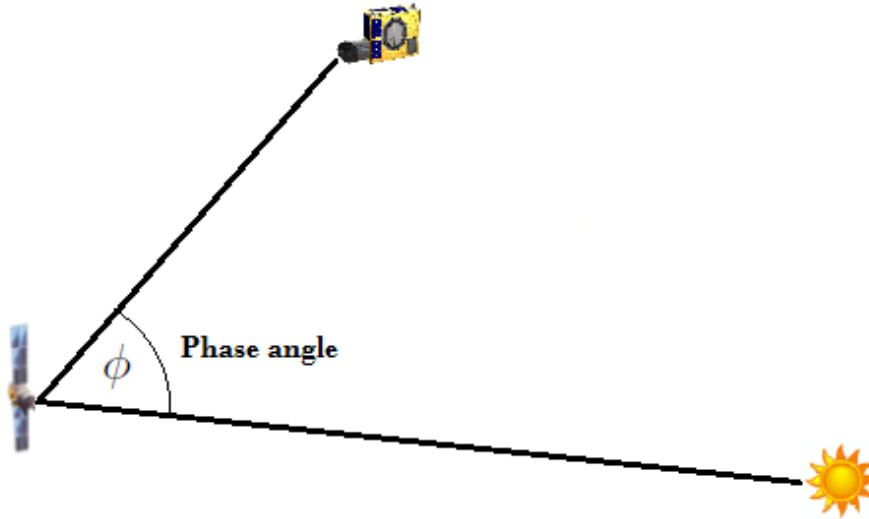
Figure 3.8: Solar phase angle defined.

Assuming a diffuse spherical RSO its detected magnitude can be estimated from the solar phase angle ϕ, its cross sectional area A, reflectivity ρ and range

R by [39]:

$$M_v = M_{Sun} - 2.5\log_{10}\left(\frac{\rho A F(\phi)}{R^2}\right) \tag{3.2}$$

where $M_{Sun} = -26.74$, the solar magnitude and the phase function $F(\phi)$ is given by:

$$F(\phi) = \frac{2}{3\pi^2}\left[(\pi - \phi)\cos\phi + \sin\phi\right] \tag{3.3}$$

Figure 3.9 shows how the visual magnitude of an RSO varies as a function of its phase angle. This relationship is approximately linear [40]. As no direct model is available for either a given RSO's attitude or its reflectivity then, in general, an RSO is brightest when the phase angle is at minimum. In this configuration a maximal amount of sunlight is then reflected back to the observer.
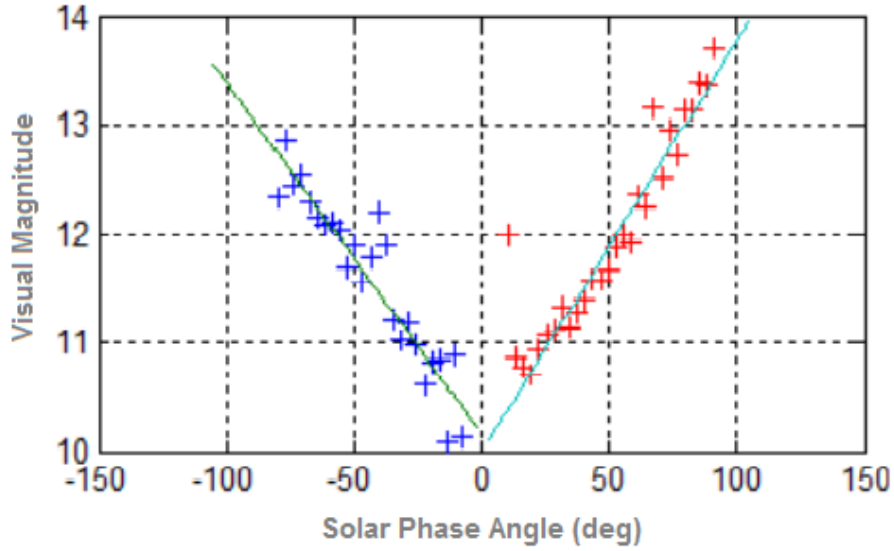
Figure 3.9: A linear fit of visual magnitude to solar phase angle [40].

For an astronomical image the apparent magnitude of a detected source is determined from that image's zero-point magnitude. The zero-point magnitude (V_0) of an image is by definition the magnitude that produces one count per second given the relationship between intensities of detected stars to their catalog magnitudes. While the zero-point magnitude is inherently linked to a sensor's aperture and quantum efficiency it can vary depending on background light levels and sensor dark current, so a unique zero-point magnitude is calculated for each frame. The zero-point magnitude is typically determined during astrometry by relating the intensities of stars in an image, measured in counts, to their catalogued visual magnitudes. Once V_0 is known the apparent visual magnitude (M_v) of any source in an image can be determined by [41]:

$$M_v = -2.5 Log \left(\frac{Total\,Intensity}{Exposure\,Time} \right) + V_0 \qquad (3.4)$$

For the SBV mission Equation 3.4 was used to determine apparent visual magnitudes of detected RSOs. The limiting magnitude of the SBV sensor was presented as the minimum detected magnitudes of all RSO observations. Figure 3.10 shows the histogram of SBV RSO observation magnitudes for the first year of operation [13], with objects of brightnesses down to magnitude 15 detected.

Using the characteristics of an optical sensor's CCD and some assumptions on the background light levels of the sky one can estimate the signal to noise ratio of an RSO of a given magnitude via the method described by Hejduk et al in [42]. In this analysis, we choose an idealized situation where TRM rates have perfect matching between the slew of a telescope and the angular velocity of an RSO across the image frame (so that the RSO signal accumulates centred on a single pixel), and in the absence of any jitter from the attitude control system. In these conditions then, at a given exposure length T_{Exp} the accumulated signal S (photoelectrons) from an RSO of visual magnitude Mv

can be expressed as:

$$S = A_{Eff} \cdot 10^{-0.4Mv} \cdot Q_E \cdot F_0 \cdot K_f \cdot T_{Exp} \qquad (3.5)$$

Where A_{Eff} is the effective light collecting area of the CCD, Q_E is the CCD quantum efficiency, F_0 is the photon irradiance of a 0th magnitude star, (in photons per second per square meter). The straddle factor K_f is the ensquared energy, or the percentage of energy from a point source illuminating the best pixel on the CCD array.

Over the same exposure interval T_{Exp} the noise accumulated N (photo-electrons) is a function of the shot noise N_{sys}, the sky background magnitude N_{BG} and dark current N_{DC}:

$$N = \sqrt{N_{sys}^2 + N_{BG} \cdot T_{Exp} + N_{DC} \cdot T_{Exp}} \qquad (3.6)$$

Once one has an estimate for both the signal strength and the noise accumulated the SNR is simply their ratio. For NEOSSat, the constants among these parameters are listed in Table 4.2 in Section 4.4. Some parameters such as the effective area and quantum efficiency come from the physical charac-
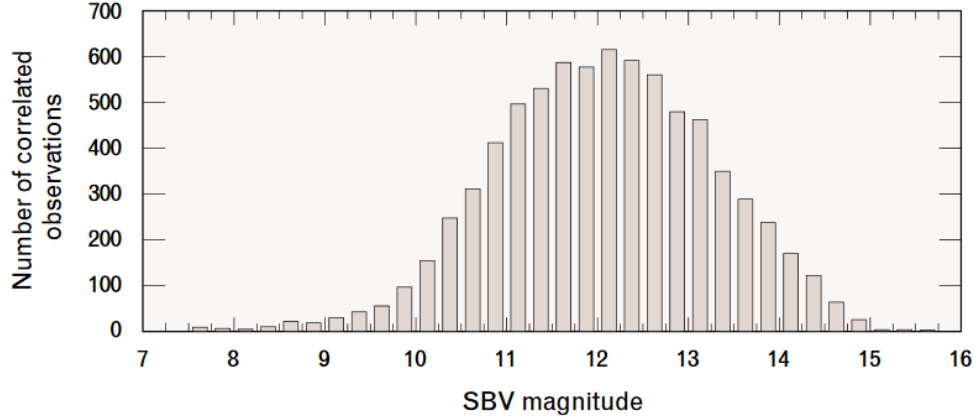
Figure 3.10: Apparent visual magnitude histogram of SBV detected RSOs [13].

teristics of the E2V CCD and telescope. Noise modelling parameters and the straddle factor K_f were measured on orbit through analysis of NEOSSat imagery.

To determine the limiting magnitude M_{Vlimit} of the platform, one has to choose an acceptable signal to noise ratio cutoff SNR_{cut} for signal detection. For example, at an SNR of cut-off value of 3, which is a low bound when detections are made in automated processing and no false positives are desirable. For a given value of SNR_{cut} cut, Equations 3.5 and 3.6 can be rearranged to isolate M_v. NEOSSat's theoretical limiting magnitude is then given by:

$$M_{Vlimit} = -2.5Log(SNR_{cut} \cdot N/S) \tag{3.7}$$

With these characteristics in mind, a need has obviously presented itself to develop an automated image processing system, based on new and legacy algorithms, that can process HEOSS imagery to detect RSOs that is sensitive down to the theoretical limiting magnitude of the satellite, while maintaining full metric accuracy.

3.6 Summary of Contribution to this Research

Up to this point, the chapter has described the previous body of work that was used as the starting point for this thesis research project. The remainder of the chapter will now describe the three main contributions that were developed during this thesis research project.

3.6.1 Automated Image Analysis

This research objective is to create an image processing system that can fully process NEOSSat's space-based track rate mode imagery, verifying its metric accuracy is in accordance with SSN standards, and its limiting magnitude is as close as possible to the theoretical limit. A suggested algorithm for star streak identification and RSO detection from a space-based platform is outlined in

[43] and fully implemented in this thesis. It suggests a matched filter based approach to star streak detection and an image stacking process to maximize RSO detectability. The matched filter based star streak detector developed in [30] must be adapted for NEOSSat TRM imagery in order to seed accurate astrometric calibration of each image. Once the pointing and slew rate of each image is known the motion of the targeted RSO relevant to this pointing must be computed from its TLE and the offsets accounted for in a common frame. This will enable stacking of all images in a sequence on a common reference pixel in the relative NEOSSat-RSO frame, making the signal from the RSO additive. Detection of all signals in this stacked image can then be performed and any signals that are persistent in these relative locations in all imagery will imply that the source comes from light travelling through the telescope, not a cosmic ray event. This method would allow for maximally sensitive signal detection of both RSOs and star streaks, which should meet the theoretical limiting magnitude derived in Section 4.4.

3.6.2 Metric Assessment

Once RSO detections are made, they can then be correlated against known objects in the SSN TLE catalog, and their true positions correcting for stellar aberration calculated. B3 Type 9 and photometric data products can then be produced. HEOSS observations will be calibrated for accuracy against well known GPS reference ephemerides, with the goal to meet or exceed SSN metric standards.

3.6.3 Limiting Magnitude

RSO detection sensitivity, derived in 4.4, is assessed through a survey of faint RSOs. Limiting magnitude models are verified and the performance of automated signal detection algorithms are compared with NEOSSat's theoretical limits. This assessment provides an estimate of the faintest detectable object using the NEOSSat system.

4 HEOSS Imagery Acquisition and RSO Detectability

This chapter will describe how NEOSSat was tasked to acquire TRM imagery. The implications of NEOSSat's unique method of acquiring TRM imagery relative to image processing, metric accuracy, and limiting magnitude are discussed. The tools described in this chapter were developed by the author, unless otherwise mentioned, as part of the work contributing to this thesis.

4.1 Track Rate Mode Sequences

To acquire a sequence of TRM images NEOSSat is commanded to perform a slew to the predicted location of an RSO, allowing for at least three minutes of settle time to ensure the star tracker has acquired the correct field and the spacecraft has achieved fine pointing. At the time the RSO is expected to be centred in an image, a fine slew is initiated matching the RA and DEC rates of the RSO which are calculated from that object's TLE. This fine slew proceeds until a specified destination RA and DEC are reached. Once NEOSSat reaches the destination point of fine slew it decelerates and remains in a fine pointing state ready for the next imaging task. NEOSSat can take up to 20 seconds to accelerate from fine point to its maximum TRM slew rates. When the acceleration period is finished and the desired TRM rates are reached a sequence of images are exposed. The imaging functions are commanded sep-

arately from the bus slewing and the operator must ensure they occur during the fine slewing window.

A limitation of the NEOSSat attitude and control system is that fine slews can only be maintained at a constant angular rate. This impacts the duration for which NEOSSat can track an RSO in track rate mode as the relative motion between the two objects is constantly changing. This presented a significant challenge for TRM acquisition since any mismatch between NEOSSat's slew rate and the RSO's motion across the sky would result in an elongation of the centroid of the RSO. As a consequence, this limits the detectability of faint objects as their signal would be spread out over a larger number of pixels, similar to the limitations of SSM. When the mismatch between NEOSSat's fine slew rate and the observed object's motion is such that the RSO's image is too elongated for a proper detection and centroiding, or when the RSO exits the field of view, then NEOSSat is programmed to exit the fine slew mode and re-acquire the object when observation conditions will be better.

To task NEOSSat in TRM, a method of determining the relative angular rates between NEOSSat and RSOs during acceptable access windows was created at DRDC is and is explained in the next section.

4.1.1 HEOSS TRM Planning Tool

The NEOSSat Mission Planning System (MPS) was designed to automatically calculate, with little user intervention, TRM imaging sequences and their corresponding macro commands to be sent to the NEOSSat spacecraft. However, the commissionning phase for the NEOSSat spacecraft lasted much longer than originally anticipated and as a result, the MPS could not be used to schedule HEOSS imaging tasks. This is because NEOSSat's capabilities were being frequently updated while the MPS's scheduling algorithms had more static considerations. In order to schedule HEOSS imagery a tool was developed at DRDC, by Dr. Robert Scott and the author, that determines NEOSSat look angles and TRM rates to a given RSO and creates a macro

command listing for the satellite to execute.

The HEOSS planning tool computes the relative rates of RSOs from NEOSSat using the latest TLEs of both objects and Analytical Graphics Inc. (AGI)'s Systems Tool Kit (STK) software, version 10. The planning tool consists of a Microsoft Excel spreadsheet controlling Visual Basic macros which command STK and parses its reports. For a given RSO, the tool computes the RA and DEC look angles and their rates at times when all viewing geometry constraints of NEOSSat were met. It then creates macro commands to initiate a coarse slew with enough lead time to settle at target, accelerate to a fine slew rate that matches the RSO's motion during the middle of the entire sequence, and collect a series of images at exposure lengths commensurate with the TRM velocity.

Figure 4.1 shows the range and relative angular velocity (rate needed to perform a TRM slew) to an object in GEO (Anik F1) during a prolonged access window. While the total possible observation period lasts almost an hour, the relative angular rates vary from up to 50 arcsec/s, at approximately 04:10 UTCG to near stationary at 04:25 UTCG.

Access windows to MEO objects, such as a GPS satellite are typically much shorter than to GEO objects. This is partially due to line of sight constraints but mainly due to the maximum TRM angular rate cutoff of 60 arcsec/s. Objects in these orbits can have a peak angular rate of around 195 arcsec/s with respect to NEOSSat. On orbit it was determined that NEOSSat could reliably achieve 90 arcsec/s, outperforming its design requirement of 60 arcsec/s fine slews. That said, for scheduling purposes the original cutoff was implemented because the closer range geometries that resulted in rates higher than 60 arcsec/s varied in speed too fast to allow NEOSSat to complete a full TRM sequence before rate mismatches were too high. Figure 4.2 shows the range and angular rate to GPS SVN #61 of a single access window.

Given that NEOSSat is limited to constant angular rate fine slews and an RSO's relative rate varies continuously, the relative rate at the middle of the
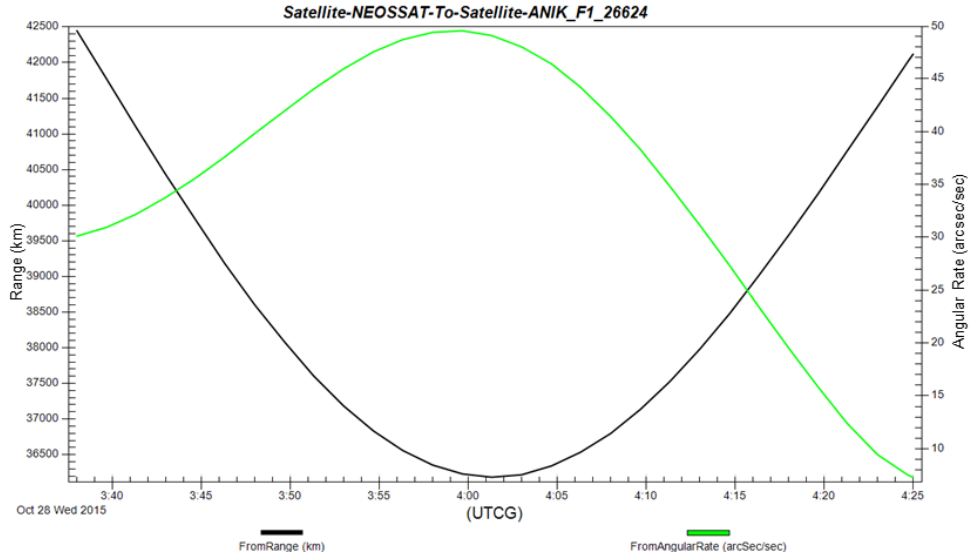
Figure 4.1: Range and relative angular rate from NEOSSat to the Anik F1 geostationary satellite during an uninterrupted access window on 28 Oct. 2015.
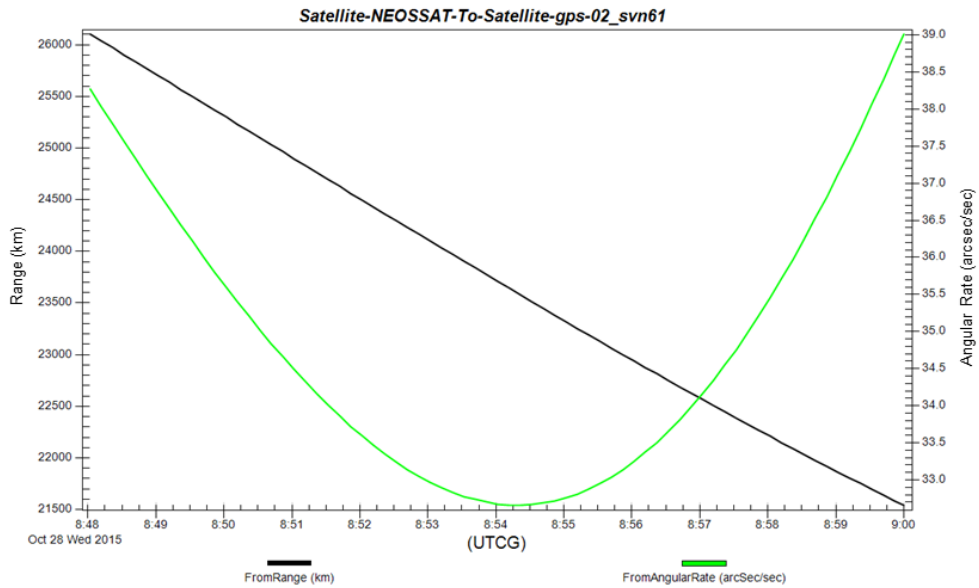
Figure 4.2: Range and relative angular rate from NEOSSat to a GPS satellite during an uninterrupted access window.

48

sequence observation time is chosen for the fine slew rate to minimize rate discrepancies throughout acquisition.

Typically for 1x1 binned images, TRM sequences consist of four images with an interval 90 seconds between exposure start times to allow for image readout. For 2x2 imagery, which has a faster readout time, sequences of 8-10 images are taken at an interval of 30 seconds. The exposure duration is the same for each image and is chosen depending on the angular rate to ensure that star streaks are kept to a length of less than 100 pixels in 1x1 binning. Each of these series of images, acquired at a constant rate are considered to be a single sequence and are thus processed together as a batch.

It is noted here that since TRM fine slew rates are constant, an emphasis is placed on scheduling when an RSO's relative rates do not vary too greatly. Moreover, to maximize the signal to noise ratio, images were scheduled as close as possible to minimum solar phase angle. A minimum angular rate limit of 10 arcseconds per second was also enforced so that star streaks could be easily distinguished from RSO, as a zero angular rate is effectively a SSM image.

A sample macro command listing for a TRM sequence of four images of a GPS satellite is shown in Figure 4.3. The RA, DEC and ROLL to settle in for fine point is at (32.161, -24.139, 27.649) degrees. A fine slew is initiated with the command TRM_Slew to a destination RA and DEC of (28.588, -23.271, 25.2288) at a velocity of 34.44 arcsec/s. This task was for full frame imagery at 1x1 binning with an exposure length of 6 seconds, leaving a buffer time of 90 seconds between each exposure. For this task the angular rate chosen for the fine slew was 34.4 arcsec/s, which was the average rate during the sequence, but at the start the RSO was moving at 41.9 arcsec/s and finished at 27.6 arcsec/s.

Figure 4.4 shows the RSO detected in each image taken with the macro commands above. One can see that the middle two images had a compact centroid while NEOSSat was moving close to the relative rate of the RSO,

49

```
gps-29_svn57:  Start,  Average,  End RSO  rates:
              41.919,  34.438,  27.649   (''/s)
Slew          2015-301-01:05:00.000    32.161  -24.139  26.647
TRM_Slew      2015-301-01:10:00.000    28.588  -23.271  25.2288  34.44
Exposure      2015-301-01:10:40.000    6000
Exposure      2015-301-01:12:10.000    6000
Exposure      2015-301-01:13:40.000    6000
Exposure      2015-301-01:15:10.000    6000
```

Figure 4.3: Sample macro command listing for a TRM sequence of four images of a GPS satellite.

but the outlying images had rate mismatches of about 10 arcsec/s each. For a 6-second exposure this is about 60 arcseconds, or 20 pixels. As GPS satellites are relatively fast moving compared to RSOs in geostationary orbit this represents an example of the worst sort of rate mismatch that was tolerated in HEOSS tasking, however one can see how the prolonged image download time mentioned in Section 2.1.2 limited the effective number of images that NEOSSat could take in a given TRM sequence. While attempts are made to limit the elongation of RSO signatures in TRM sequences, the image stacking algorithm discussed in Section 5.5 considers elongated point sources valid if they meet all other source criteria.
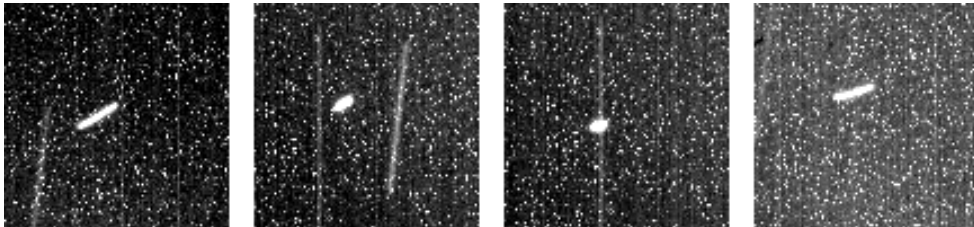
Figure 4.4: A GPS satellite in the four frames of the TRM sequence in Figure 4.3. The signature is elongated when NEOSSat's constant angular slew rate differs from the relative rate of the GPS satellite.

4.1.2 TRM pointing stability

As discussed in Section 3.6.1, a matched filter will be used to detect stars in a TRM image. The matched filter algorithm requires the length and orientation of each star streak to be known [29] to seed detection. Theoretically this could be supplied by the OPS6 ADCS software on-board NEOSSat (see Section 2.1.2), but any deviations between the expected TRM rates NEOSSat was commanded to perform and the true rates achieved against the sky would result in a miscalibrated matched filter and star detection performance would suffer.

To quantify the performance of OPS6 ACDS software, NEOSSat's pointing stability in TRM was analysed independently of the readouts of the ACDS system by investigating NEOSSat's motion relative to stars in its imagery. Figure 4.5 shows NEOSSat's commanded constant slew rates from two TRM tasks (the red line), and the rates achieved by measuring the star streaks visible in each image (points). In each case, the time axis begins at the exposure time of the first image in a sequence. Rates were calculated from the median length of star streaks detected in each frame. This value is measured in pixels, and converted to angular rate given NEOSSat's 3.00 arcsecond pixel size and the image exposure time. It should be noted here that the total angular rate measured (top graphs in Figure 4.5) is in the body frame and the individual RA and DEC rates are measured in the spherical celestial frame. This accounts for the RA rate having a higher value than the total rates, given the declination of either image was far from the equator. In all, Figure 4.5 shows that the NEOSSat spacecraft can reliably achieve commanded TRM slewing rates, providing imagery that can be processed with the algorithms that will be explained in Chapter 5.

Figure 4.5: NEOSSat TRM fine slewing stability of two GPS tracks from full scale imagery (left) and 2x2 binned imagery (right). Red line indicates commanded rate while rates observed in each image are points.

4.2 NEOSSat Ephemeris Generation

To perform the HEOSS metric data mission, accurate knowledge of the surveillance sensor location at the time of each observation is required. While not used for scheduling or task generation, NEOSSat's MPS still processes numerous telemetry products and raw imagery received from the satellite. Crucial to maximizing the accuracy of SSA metric data is precise timing and location knowledge of the observing platform, namely the NEOSSat spacecraft. NEOSSat ephemeris uncertainty requirements must be within 50 m at any time, and timing accuracy of image exposures must be on the order of one mil-

52

lisecond to meet US Space Surveillance Network metric standards. To achieve this, NEOSSat is equipped with two identical Novatel OEMV-1G GPS receivers, located on opposite side of its bus on the +Y and -Y faces, typically with only one in operation at a given time. One receiver is visible as the round object at the back of the bus in Figure 1.5. Navigation solution (navsol) files are generated daily from telemetry by the operations team at the CSA and sent to the MPS. Each navsol file contains time, position and velocity data at a 5-second temporal resolution. The on-board GPS is also used to regulate NEOSSat's computer clock, providing precise image exposure times.

For each navsol file the MPS receives it runs an Extended Kalman Filter using AGI's Orbit Determination ToolKit (ODTK) to produce an orbital ephemeride for the NEOSSat satellite. Figure 4.6 shows the measurement residual ratios of navsol data points processed by ODTK's filter with a measurement noise 1-sigma of 10 meters. The residuals are differences between the observations and the state vector solution produced by the filter, propagated through all observation times. The filter only processes position and time measurements from the navsol file as the velocity measurements in the navsol are derived from the other two quantities and do not add any new information to the filter.

The residuals in Figure 4.6 are periodic with each orbit and largest nearest the poles. This is because at high latitudes a lower number of GPS satellites contribute to its navigation solution, degrading the quality of the position measurement. The ODTK filter is easily able to handle such cases: when the observations are outside of a 3-sigma limit between the sensor uncertainty (10 meters) and the state covariance matrix, the filter rejects the measurement and processes the next one.

Figure 4.7 shows the position uncertainty of the ephemeris produced from the observations in Figure 4.6. The ODTK filter produces consistent NEOSSat ephemerides with 1-sigma positional uncertainty below one meter. These ephemerides are used to interpolate NEOSSat's Cartesian position for all
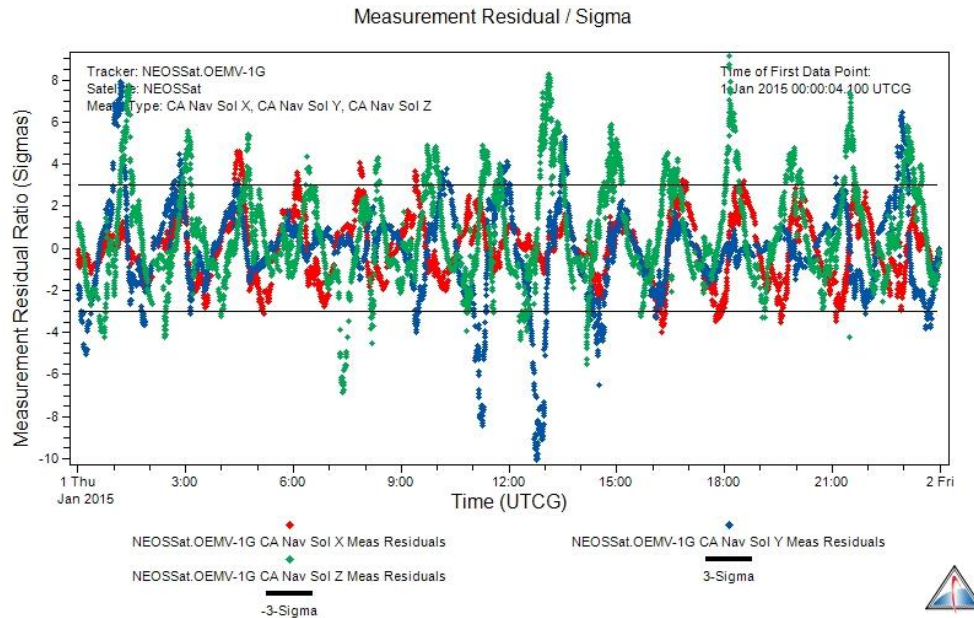
Figure 4.6: Kalman filter residual ratios of NEOSSat GPS navsol data for January 1st, 2015 as processed by NEOSSat's Mission Planning System.

HEOSS observations.

Once a navsol file is processed by the MPS, the astronomical images are then sent to the MPS and their header entries updated with NEOSSat positions and velocity in both the J2000 and ECEF frames for the exposure start, middle and end times. The position data is used in relative viewing geometry calculations in the image stacking algorithm (Section 5.5), the observation correlator (Section 5.6.1), and in creating B3 Type 9 metric data products. The velocity data is used to correct for the apparent shift in background stars due to stellar aberration effects (Section 5.6.2).

54
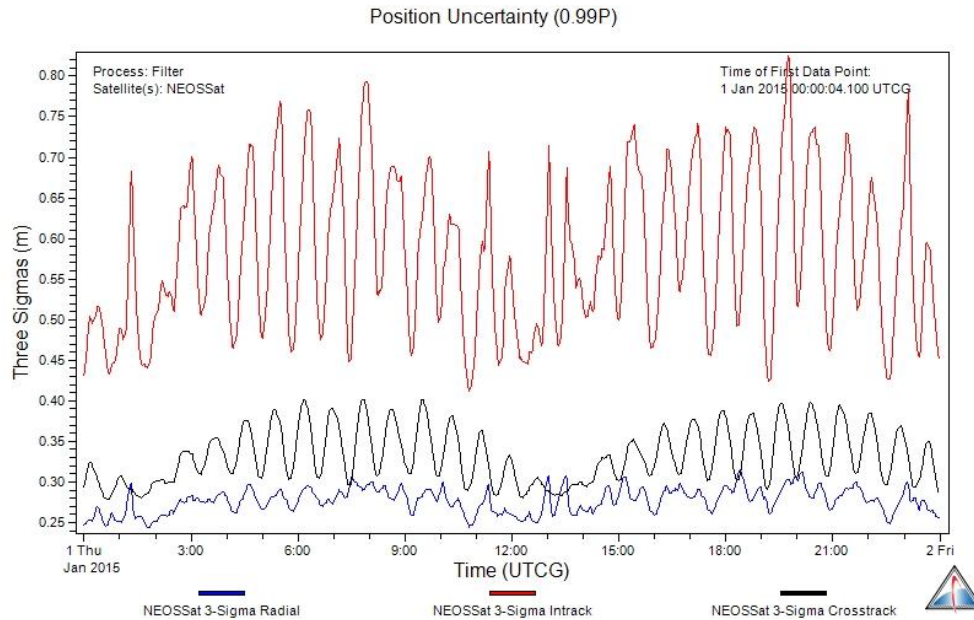
Figure 4.7: NEOSSat ephemeris position uncertainty (3-sigma) for January 1st, 2015.

4.3 HEOSS Metric Error Budget

This section presents the metric error budget for HEOSS TRM observations. The metric error of an observation is the positional uncertainty of the measured RA and DEC of a detected object in the CCD image compared to its true position, expressed in arcseconds.

Table 4.1: NEOSSat error budget for TRM imagery in 1x1 and 2x2 binning.

Error source	σ (arcseconds)	
	1x1	2x2
Ephemeris, 1 m	0.01	0.01
Timing, 1 ms	0.06	0.06
RSO centroid	1.2	2.1
Boresight pointing	1.3	2.3
Total RSS error	1.75	3.12

55

The predicted HEOSS metric error budget is an estimate of metric observation accuracy from all known sources of uncertainty. Similar to the SBV error budget presented in Section 3.4, using equation 3.1 we can predict the expected accuracy of HEOSS metric observations. Table 4.1 shows the contributions of each source of error contributing to the RSS total error budget. Values are calculated for both 1x1 and 2x2 binned imagery.

The ephemeris and timing errors were discussed previously in this chapter. The boresight pointing and associated astrometric uncertainty is modelled in Section 5.4. Centroiding methods and error is presented in Section 5.5.2.

4.4   RSO Detectability for NEOSSat

Using the theories introduced in Section 3.5 we can compute the theoretical limiting magnitude of RSOs detectable in HEOSS imagery. For NEOSSat, the constants among the parameters in Equations 3.5 and 3.6 are listed in Table 4.2. The straddle factor K_f is taken as the best case value from an ideal NEOSSat focus, where the optical point spread function has a Full-Width Half Max of (FWHM) of 6.25 arcseconds.

Table 4.2: Detectability modelling parameters.

Parameter	Value	Definition
A_{Eff}	0.01308 m^2	Effective light collecting area
Q_E	0.3048	Solar weighted quantum efficiency
F_0	5.6 x 10^{10} ph/s/m^2	Photon irradiance of a 0th magnitude star
K_f	0.1858	Straddle factor
N_{sys}	20 e-	System noise (CCD read noise)
N_{DC}	0.2 e-/s	Dark current per pixel at -30 deg Celcius
N_{BG}	1.05 e-/s	Background sky noise at 23.2 $M_v/arcsec^2$

Using the parameters listed in Table 4.2 and an exposure time of 5 seconds a limiting magnitude of 16.3 can be expected from NEOSSat at an (SNR_{cut}) detection cut-off of 3. This is under ideal background lighting and dark current

conditions. The full curve of limiting magnitude as a function of exposure time under ideal conditions is given in Figure 4.8, where NEOSSat's operating exposure range is between one and ten seconds for HEOSS imagery. For star stare mode, one can see that the limiting magnitude is substantially less than for track rate mode. This is due to the fact that an RSO will spread its signature over new pixels as the image exposes, effectively making the signal constant over time while the noise sources, N_{DC} and N_{BG}, accumulate over time. This SNR advantage is the primary motivator for using TRM as the main imaging mode for HEOSS.
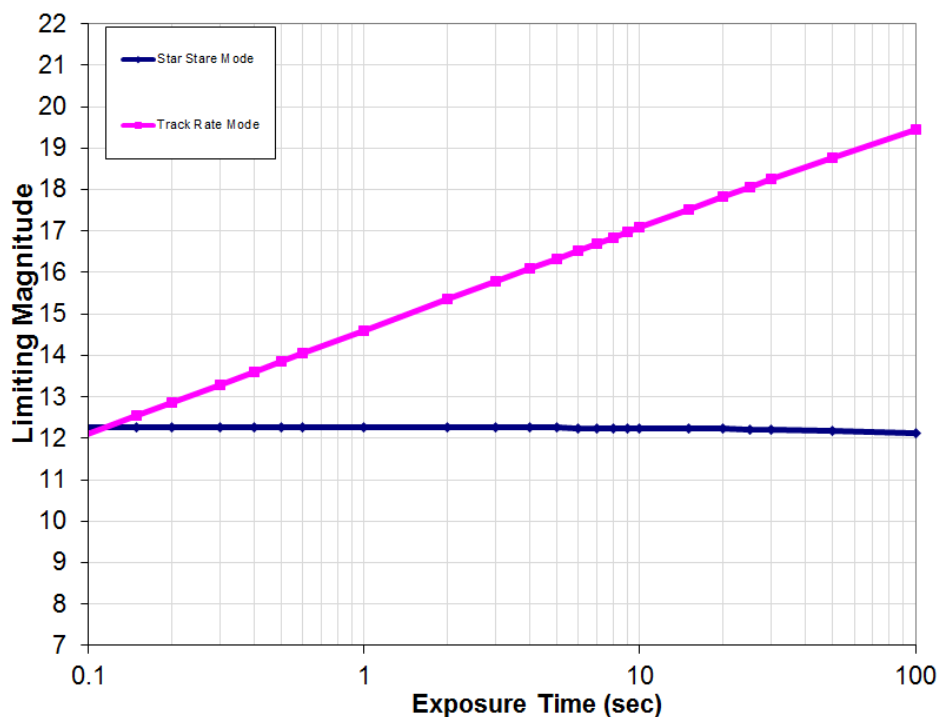
Figure 4.8: Expected limiting magnitude of NEOSSat under ideal conditions (SNR = 3).

Figure 4.9 further illustrates this concept: it shows a 3D plot of a sub-portion of a NEOSSat image in TRM matching the rate of an RSO. In this

figure the stars are streaked, spreading their energy over many pixels while the stationary RSO accumulates signal. In SSM imagery the roles are reversed, leading to the poorer RSO brightnesses expected from Figure 4.8.
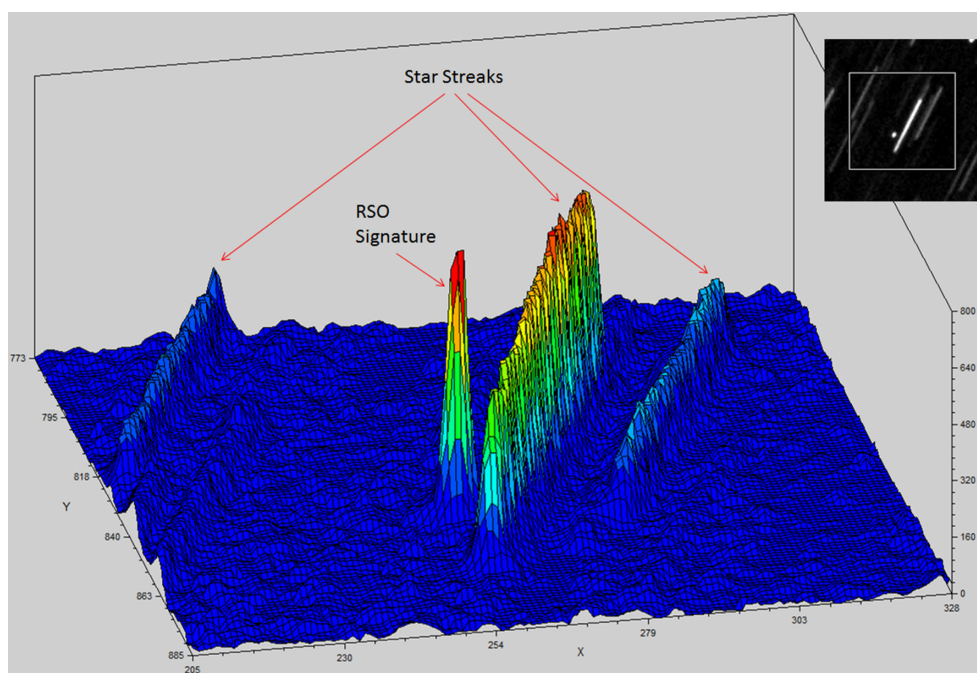
Figure 4.9: RSO and star signature intensities of a sub-portion of a HEOSS TRM image (inlaid top right).

5 Image Processing (SQUID3)

This chapter describes the methodology and algorithms that were implemented by the author, based on algorithms in [43], to process raw NEOSSat TRM imagery in order to successfully detect the RSOs and stars in each image, correlate them with known RSOs in the SSN catalog and create metric data products.

NEOSSat images are delivered uncompressed in the Flexible Image Transfer System (FITS) file format [44]. The FITS format allows for a binary array of imaging data preceded by a text header portion of keywords detailing information about the image. Typical header information for example includes exposure time, CCD temperature, targeted RA and DEC, imaging mode (SSM or TRM), precision timing information and binning mode. As discussed in the previous chapter, the MPS adds NEOSSat ephemeris information to the FITS headers after which they are considered a complete data product and sent to the HEOSS science users.

Once images are delivered by the MPS, they are ready to be processed. Images are sorted by their 'OBJECT' header in the FITS image, which identifies the intended RSO to be tracked in each image by SSN catalog number. They are then grouped into tracking sequences by time duration in batches of under 300 seconds, which is above the maximum amount of time spent on an RSO track, and below the minimum amount of time to move between two successive tracks. Any images taken in SSM are processed with the Satellite Streak Detection (Section 3.1.3) matched filter streak detector. As discussed

in 4.4, HEOSS generally avoided the collection of SSM images, the bulk of the image processing was done on TRM imagery by the image stacking algorithm.

5.1 Pre-processing

Optical telescope imagery is usually corrected for thermal background noise with dark frames, images taken at the same exposure length and temperature of a light frame but with the shutter closed. These frames only consist of thermal and readout noise, which can then be subtracted from a light frame to produce an enhanced signal image.

Before images are processed, an attempt is made to reduce the image background via dark frame subtraction. NEOSSat's shutter is inside the telescope housing near the corrective field flattener (Figure 2.1) and is not intended to be open or closed routinely. This makes routine dark frames at the same exposure times and CCD temperatures close to TRM sequences unavailable. This presents a very large challenge to image processing because of the elevated noise levels and hot pixel counts quantified during commissioning [23]. The E2V 47-20 CCD used for science imagery has a measured dark current of 0.2 e-/s at a nominal operating temperature of -30 degrees Celsius. In practice NEOSSat's CCD temperatures are closer to -25 degrees Celsius for HEOSS imagery as frequent changes in attitude often prevented optimal cooling of NEOSSat's CCD radiator, which passively cools the payload electronics. On a typical orbit, the CCD would experience temperature fluctuations of about 6 degrees Celsius. This variable thermal environment and frequently changing exposure durations essentially requires a new dark frame to calibrate each TRM sequence. This is not possible with the existing shutter, not only because repeated use is feared to eventually cause a malfunction, prematurely ending NEOSSat's mission, but also because use of the shutter obscures the co-boresighted star tracker CCD, which would drop NEOSSat out of a fine pointing state and add extra time to re-acquire a star lock between tasks.

5.1.1 Minimum Dark Frames

To overcome the lack of a shutter, a method of creating an ersatz dark frame from the minimum pixel values of an entire TRM sequence is used. Since all frames in a sequence share an equal exposure length and similar CCD temperature, it can therefore be confidently assumed that the images have nearly all the same level of dark current. Also, since the light of the stars is in motion in each frame and the expected RSO position changes between frames then there stands a good chance of one pixel to be free of any outside light source in at least one of the frames. In [45] the use of a median image of a TRM sequence is suggested to enhance visibility of RSOs in ground based imagery. This method was considered, but given NEOSSat's short sequence length of four frames, the risk of RSO signal being in the median image was high. Consequently, it was decided to use a minimum dark image, reducing the possibility of signal corruption.

A minimum dark frame is constructed by taking the minimum value for each pixel throughout the sequence. This minimum dark frame is then subtracted from each frame creating a background reduced image. This method effectively reduces hot pixel noise and column defects while minimally effecting light signals in each image.

Figure 5.1 shows a four image TRM sequence of a GEO satellite cluster without any pre-processing. Some stars are visible, and the RSOs even less so, under the presence of numerous hot pixels and an un-removed dark current. The rms noise level present in an empty region of the first image is a very large 509 counts.
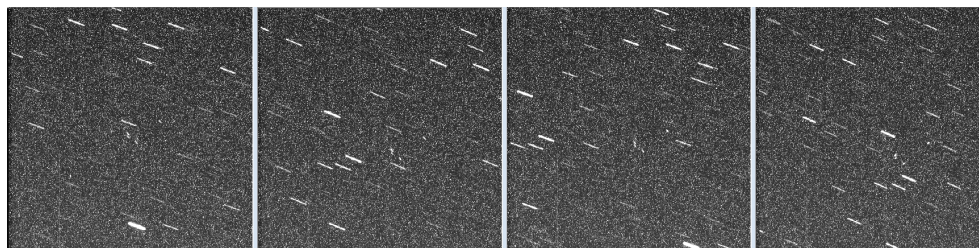
Figure 5.1: Four raw images of a TRM sequence in 2x2 binning.
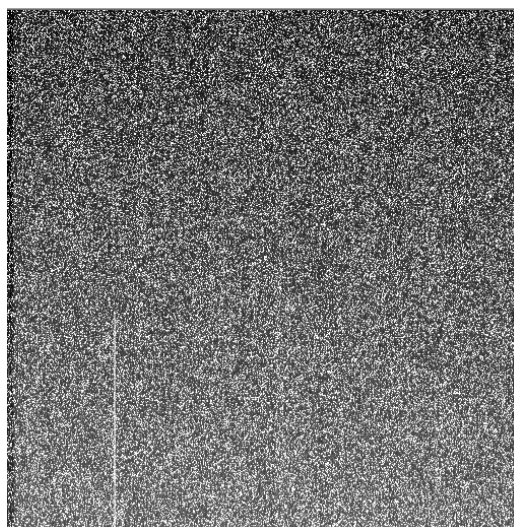
Figure 5.2: The minimum dark image from the four images in Figure 5.1.
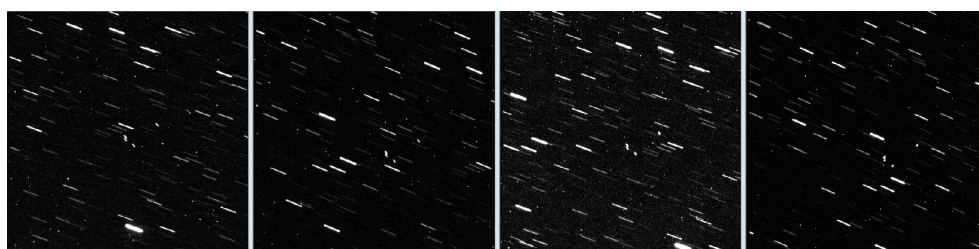
Figure 5.3: The four images from Figure 5.1 after minimum dark frame subtraction.

By creating a 3 dimensional array of size (X,Y,N) where X and Y are the size of each individual image and N the number of images in the sequence, the minimum dark frame is an image of size (X,Y) with each entry having the value of the minimum of the N pixels in the vertical dimension. Figure 5.2 shows the minimum dark frame derived from the four frames in Figure 5.1. Its rms noise level in the same region as before is now at 513 counts, virtually all of it containing signal from the dark current and hot pixels.

Once the minimum dark frame is subtracted from each individual image, a pronounced enhancement is visible (Figure 5.3). The rms noise in the same region as previously mentioned is down to only 37 counts. Many more stars can now be detected, improving both the chance and accuracy of successful astrometry. The RSOs are more clearly defined and their centroids less likely to be skewed by hot pixels. Finally, even the energetic cosmic ray contribution is now clearly visible. This is expected as they appear in random locations in each image and are unlikely to be the minimum signal contribution from any one image. All sources now clearly visible, the RSOs and cosmic rays can be detected and distinguished with the stacking technique described in section 5.5.

Table 5.1 shows the image statistics of a visibly empty region (no star streaks) of 50 by 50 pixels in the first frame before and after subtraction, as well as the minimum dark frame itself.

Table 5.1: Image statistics from frames in Figures 5.1 to 5.3.

	Raw Frame	Min Dark	Calibrated Frame
Maximum	7719	7579	318
Minimum	1843	1807	0
Average	2217	2185	46
RMS	508	513	36

It must be noted here that this technique can fail in the presence of stray light from the Earth limb, Moon or a very a bright star, which will modify the background levels of each image independent of the dark current. Such a

scenario is identified by checking that the majority of pixels in the minimum dark frame do not come from one single image (that with plausibly the least amount of stray light) but instead are distributed more evenly through each image in the sequence. In cases where a minimum dark frame is unsuitable for subtraction, analysis is performed on raw frames using standard background removal techniques described in [29].

5.1.2 Relative positions of NEOSSat and RSO

A custom version of the SGP4 algorithm described in [5], written in C++, was used to compute orbital positions of RSOs from their TLEs. This version was originally developed and verified for the Ground Based Optical system. It was modified for use in SQUID3 by switching the observer platform from topocentric latitude and longitude coordinates to J2000 Cartesian position and velocity coordinates. To seed the SGP4 algorithm, the RSO's most recent TLE is obtained from the Space-Track online database [46]. The observer location is NEOSSat's ephemeris position and velocity coordinates at the time of observation, retrieved from the image FITS header.

Sensor centric RA and DEC of the RSO, and their derivative velocities, are computed at the time of each observation. The SGP4 algorithm computes positions in a pseudo-inertial True Equator Mean Equinox frame of reference [5]. These positions are then corrected for precession, nutation and polar motion into the inertial J2000 reference frame.

5.2 SQUID3

The SQUID3 image processor is the primary system for analysing HEOSS scientific imagery and was developed by the author from the algorithms presented in the Sections 3.1.2, 3.1.3 and 3.6.1. Put simply, it takes TRM image sequences as inputs and outputs RSO detections from each image in RA and DEC format.

64

The flow of operations for HEOSS images by SQUID3 is given in Figure 5.4. Depending on the type of imagery received, either SSM, a single TRM image, or a stackable TRM sequence the appropriate RSO detection algorithm is chosen. SSM images are processed with the matched filter detection described in [29], and a single TRM, if necessary, processed with the FindStar algorithm [30]. In almost all HEOSS operations stackable TRM sequences were taken and the algorithm used to process them was image stacking, which will be described in detail here. Once RSOs are detected the observations are then correlated (Section 5.6.1) with an object in the SSN TLE catalog, and metric (B3 Type 9) and photometric products are created.

Inside SQUID3 the steps taken to detect RSOs in a TRM image sequence (image stack portion of Figure 5.4) are the following:

1. Compute relative rates with SGP4 (Section 5.1.2)
2. Detect the star streaks with FSS (Section 5.3)
3. Solve images for astrometry (Section 5.4)
4. Compute drift compensation (Section 5.5)
5. Shift and stack image onto a common pixel
6. Detect potential RSOs in stacked frame (Section 5.5.1)
7. Detect actual RSOs in each image frame (Section 5.5.2)

5.3 Star Streak Detection

For each individual image in a TRM sequence, the Find Star Streaks (FSS) streak detection software package [30] is used to locate the centroids of streak stars, and erase their signal contribution to the image. A matched filter is used to identify star streaks so that astrometry can be performed on the image. In order to identify the length and orientation of the star streaks to seed the matched filter, a 2D Fourier transform of the image is first taken, shown in Figure 5.6. The streaked stars in the original image can be represented as a rectangle function, giving the Fourier image a squared sinc pattern with an
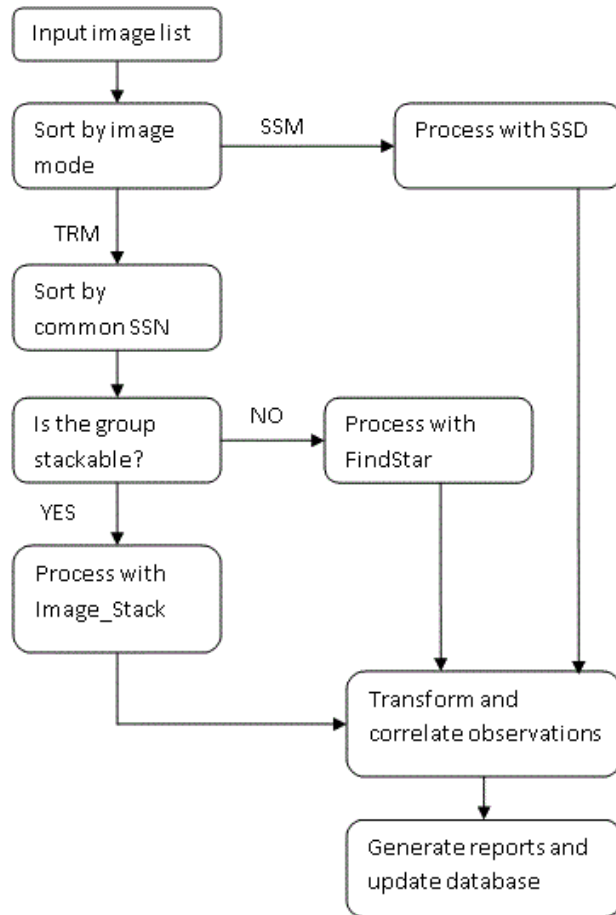
Figure 5.4: SQUID3 image processing decision tree.

orientation at 90 degrees to that of the stars and with a frequency related to the length of the star streaks.

The star streaks are obviously all aligned, which makes them a repetitive pattern easy to detect with Fourier processing. However, all individual streaks are at random positions. From a signal processing standpoint, a streak is like a rectangle function, where the signal is constant over a certain range and zero elsewhere. The Fourier transform of this rectangle function has a $sin(u)/u$ shape in frequency domain u. By using the modulus of the two dimensional Fourier transform, the shape of the $sin(u)/u$ function is preserved, and the phase can be discarded as it represents the random position of the streaks. Hence, the modulus of the Fourier transform is a clear indicator of the shape of the star streaks. Figure 5.5 shows an example of streaks in a TRM image along with the modulus of its 2D Fourier transform shown in Figure 5.6.

A Radon transform [27] is used to infer the orientation of the pronounced $sin(u)/u$ pattern, which is oriented at 90 degrees to the star streaks in the original image. The Radon transform of the image has a maximum at the same value of the angle of the $sin(u)/u$ pattern. Perpendicular to this angle, and crossing the middle of the Fourier transformed image, a profile of the $sin(u)/u$ pattern is extracted and investigated to determine its frequency (f). By squaring this profile (Figure 5.7), all detectable extremes (minima and maxima) can measured and averaged to provide a highly accurate estimate of streak length (l). The $sin(u)/u$ profile, represented by $G(f)$ is given by:

$$G(f) = Cl\frac{sin(\pi f l)}{\pi f l} \tag{5.1}$$

Where C is an unmeasured constant. By determining the frequency f of the fringe pattern the streak length l (in pixels) can be calculated simply by:

$$l = \frac{f}{2W} \tag{5.2}$$

Where W is the width of the image in pixels. Figure 5.7 shows the squared $sin(u)/u$ profile of orthogonal to the pattern in Figure 5.6 detected by the
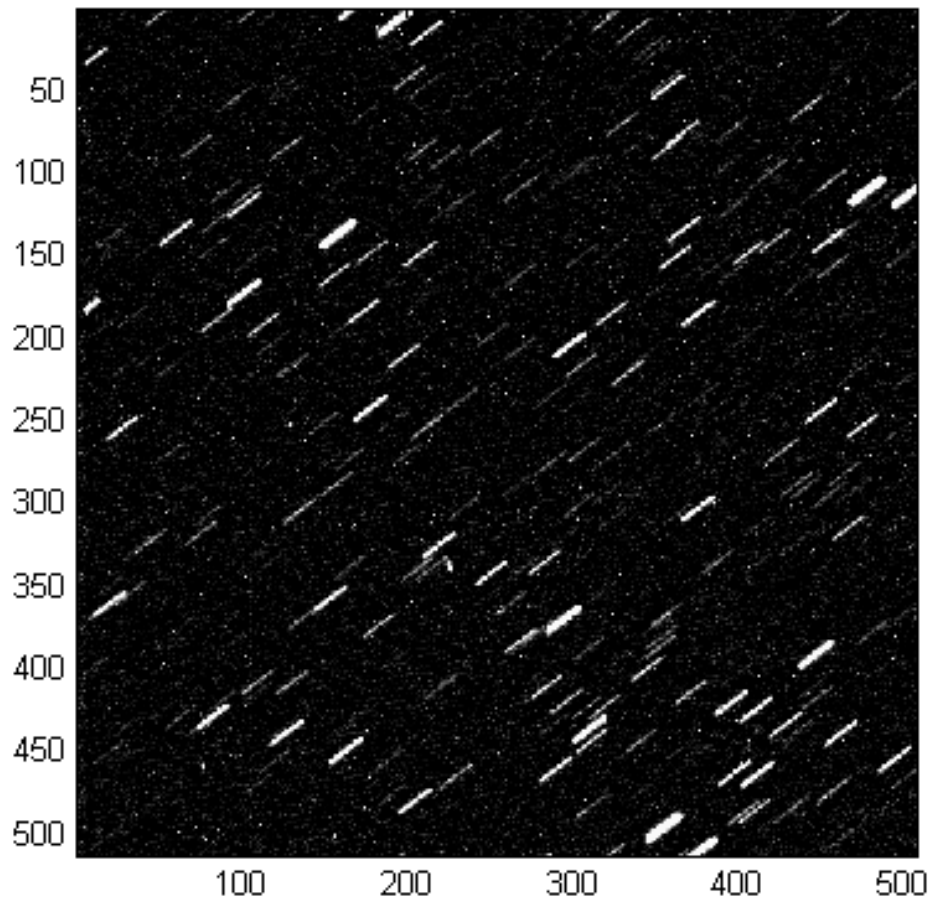
Figure 5.5: A NEOSSat TRM 2x2 binned image after minimum dark frame removal.
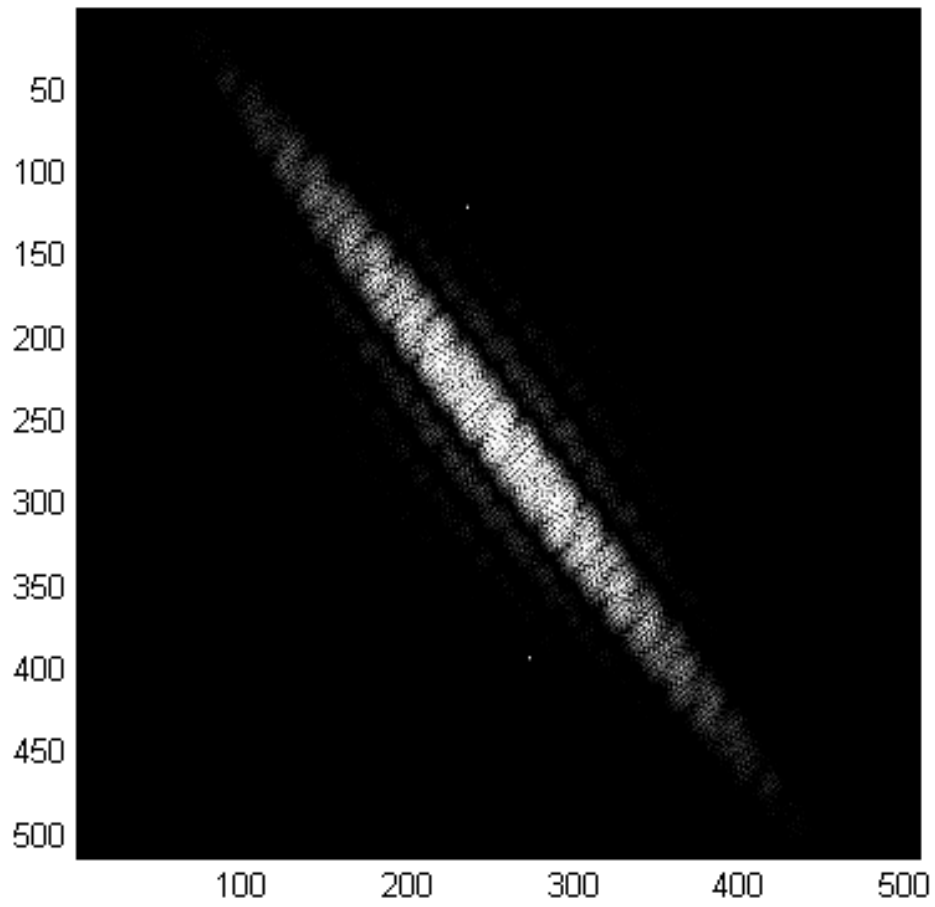
Figure 5.6: The modulus of the Fourier transform of Figure 5.5.

maximum of the Radon transform. This profile's central peak is located and its frequency is determined by averaging the distance between maxima and minima detected at either side of the peak. From analysis of the Fourier image, both the length and orientation of the star streaks in the original image are now known. At this point the iterative matched filter from [29] can be applied to extract the centroids of all star streaks. While this matched filter can detect streak signatures down to an SNR of 1, an SNR cut-off of 2 is used for detecting star streaks as very low magnitude detections have a greater centroiding error and would not contribute to the accuracy of the astrometric solution of the image.
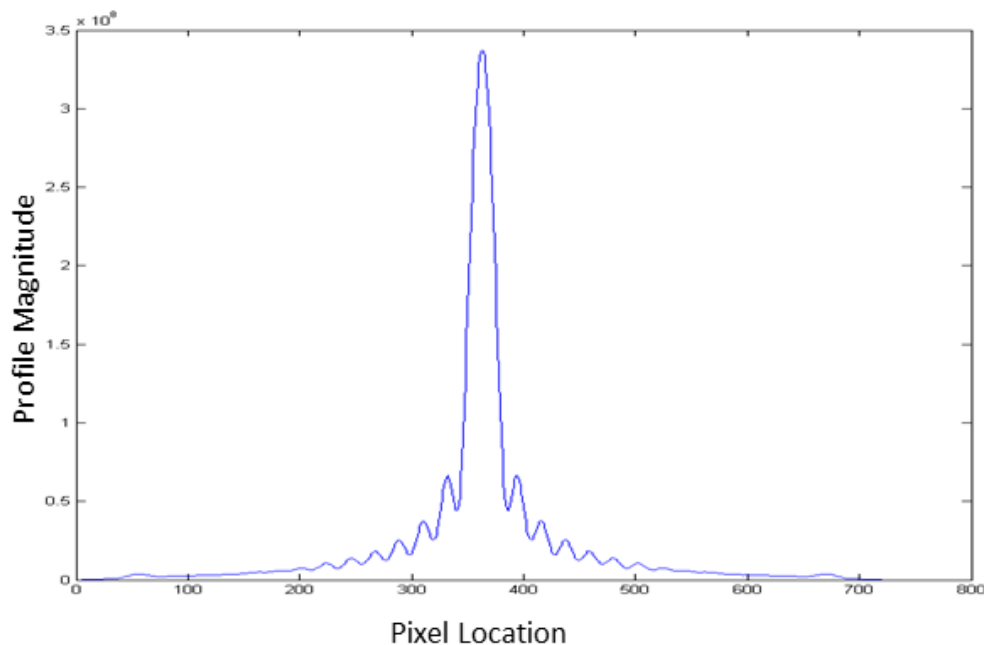
Figure 5.7: Profile of the squared 2D FFT image orthogonal to its Radon maximum.

The output of the FSS software is a list of the centroids of all detected stars, with their corresponding positions, brightnesses and detection confidence levels. The current PSF of the sensor is also determined in each image through

70

analysis of the star streak signatures. This PSF is calculated repeatedly for each new image en-lieu of using a fixed value because of the optical distortions NEOSSat can experience under different thermal loads [24]. Accurate knowledge of the PSF allows for further discrimination of RSO signatures against possible cosmic ray hits. The FSS software also outputs a star streak free image produced from detailed modelling of detected star streak signatures.

5.4 Astrometry

The star catalog chosen to perform astrometric matches of detected image stars to catalog stars is the 3rd version [47] of the US Naval Observatory CCD Astrograph Catalog (UCAC3) [48]. The UCAC3 catalog is an all-sky astrometric catalog containing star positions from magnitudes 8 to 16 with a passband between V and R, matching NEOSSat's peak sensitivity. The catalog includes proper motions giving a position accuracy of 20 milli-arcseconds down to 14th magnitude and 70 milli-arcseconds to 16th magnitude. An all sky catalog is needed due to NEOSSat's space-based mission, whereas a catalog limited to above -30 degrees in declinations (USNO A2 catalog) was used for GBO image astrometry [9].

The astrometic software package PinPoint is used to perform matches of star positions in a CCD image to catalog stars. Pinpoint is a commercial software developed and commercialized by DC-3 Dreams, SP [49] and can be scripted from MATLAB to match detected image sources to the UCAC3 star catalog. While the UCAC3 catalog contains full sky star coverage of all stars from 8th to 16th magnitude, the catalog is only sampled to 14th magnitude as fainter stars are rarely detected when streaked and the software performs both more quickly and accurately when extra catalog stars are not present in a candidate match field. If a star match is not obtained, astrometry is attempted again with the smaller and slightly less positionally accurate Hubble Guide Star catalog. The Hubble Guide Star catalog is also an all sky catalog, with fewer stars (limited to 15th magnitude) than the UCAC3 catalog.

As NEOSSat imagery is acquired in track rate mode, the stars are streaked and not natively detectable by PinPoint. Instead, a list of X,Y centroid positions of star streaks and brightness values compiled by FSS is fed as a text file to PinPoint for each image. If a catalog match is found with the appropriate pixel scale (3.0 times the binning in arcseconds) then the solution is accepted and the image is flagged for further processing. If no match is found, typically due to stray light corrupting the image, the image is dropped from the sequence.

The quality of the astrometric fitting process is shown in Figure 5.8. These figures show the residuals of star centroid positions detected in NEOSSat imagery to the locations of stars in the UCAC3 catalog (corrected for proper motion). For each point in Figure 5.8, a star was both detected in NEOSSat imagery and matched to a star in the UCAC3 catalog, contributing to the astrometric solution of its image. In practice, from 10 to about 50 stars are matched in a given HEOSS image. These matched stars are typically the brightest ones detected in an image and only represent a fraction of all detected star streaks as many are purposely rejected due to low SNR decreasing centroiding accuracy. In forming the plate solution from matched stars, a maximum residual criteria (3 arcseconds per binning level) is enforced, creating the circular pattern in Figure 5.8. The total residuals follow a Rayleigh distribution arising from the combination of the independent RA and DEC Gaussian distributed components.

Table 5.2 shows the statistics of the data star matching data compiled for Figure 5.8. The mean RMS position residuals contributing to the astrometric portions of NEOSSat's metric error budget is 1.26 arcseconds for 1x1 imagery and 2.31 arcseconds for 2x2 imagery.

A key output of astrometric processing is the ability to map the image plane's X-Y coordinates to the sky plane's RA-DEC coordinate system. When an image is solved with a valid star match, PinPoint creates a gnomic tangent plane projection map of the flat 2D X,Y coordinate system into the spherical
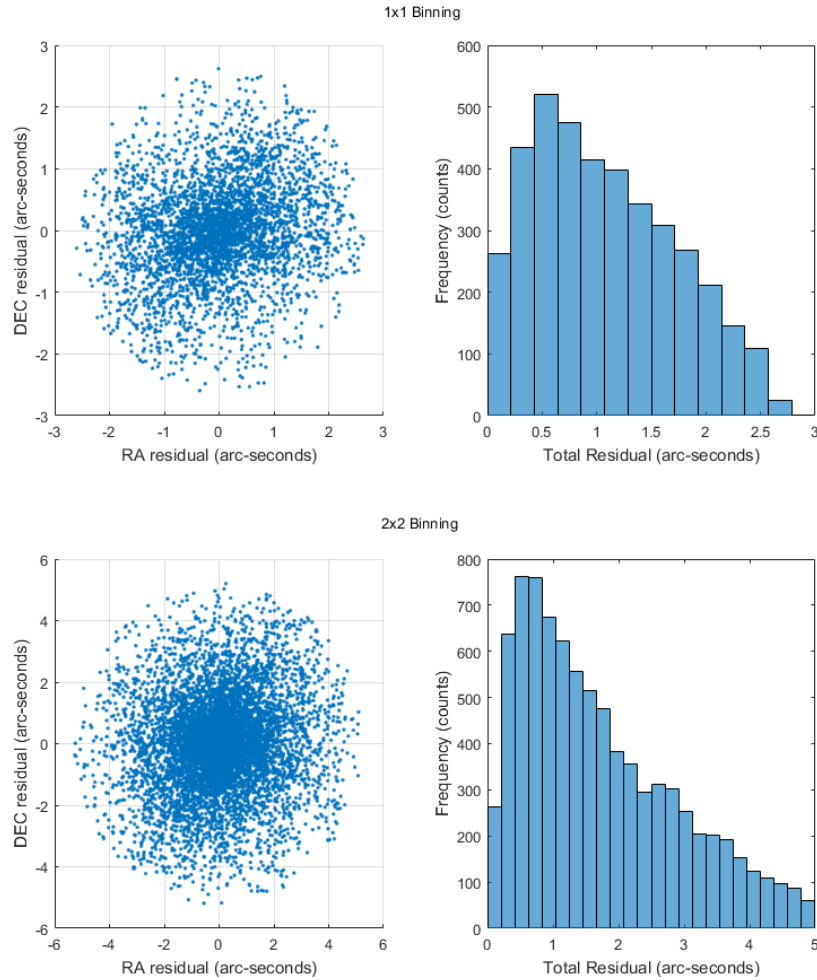
Figure 5.8: Left: star centroid RA and DEC residuals for 1x1 (top) and 2x2 (bottom) TRM imagery. Right: histograms of total residual errors.

Table 5.2: Details of astrometric fitting.

Binning mode	1x1	2x2
Number of images	243	353
Number of matched stars	3915	8460
Total RMS error (arcseconds)	1.26	2.31

RA and DEC J2000 sky coordinates. The PinPoint software computes this map adhering to FITS image definition World Coordinate System standards [50] and embeds the transformation constants into the images FITS header. The software also provides scriptable functions that are used by SQUID3 for transforming positions between the two frames and estimating the background levels and other image statistics. The catalog magnitudes of the matched stars create an estimate of the zero-point magnitude of each image, used in photometric processing.

5.5   Drift Compensation

Once astrometry is available, the relationship between the image plane and NEOSSat's motion during the image sequence can be determined. To maximize the detectability of low SNR signals the stacking algorithm compensates for position drift of the RSO in successive images so that the signal contribution from each image is additive. This drift comes from the imprecise pointing of the telescope and from the RSO's motion not being perfectly tracked by NEOSSat's constant slew rates. The RSO's relative motion to NEOSSat is approximated very accurately with the RSO's supplied TLE, but less accurately with the slewing capabilities of NEOSSat. The size of the drift errors is calculated for each image at the precise exposure time. The images are then shifted by a compensating number of pixels so that the stacked RSO signal is additive (Figure 5.9).

Equations to calculate the drift compensation of an RSO between frames of a TRM sequence are detailed in [43] and are presented here. Let p_{ex} be the X position of the expected RSO location from its TLE , p_{ey} be the Y position of the expected RSO location from its TLE, p_{tx} be the true pointing of the XY frame (centre pixel) X position and p_{ty} be the true pointing of the XY frame (centre pixel) Y position. Then this brings us to the drift matrix D, which has N rows, one for each astrometrically solved image, and two columns for X and Y direction. The amount to translate each image by to compensate
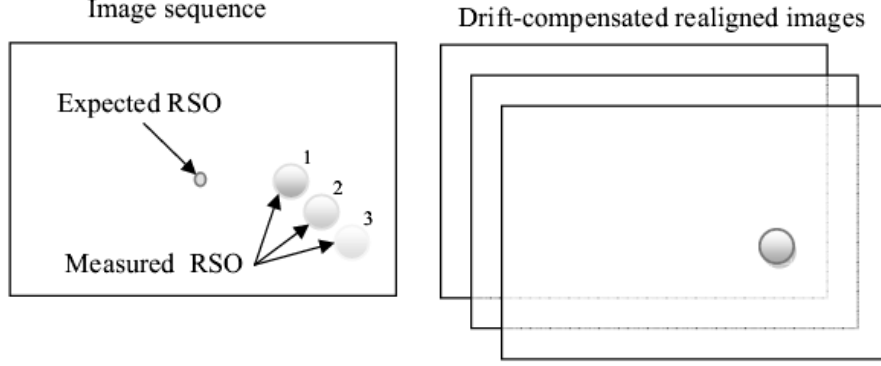
Figure 5.9: RSO positions in original image frames (left), and in the stacked frame (right) [43].

for the difference between RSO and spacecraft motion between each frame is given by the rows of D:

$$D_{i,x} = (p_{ex}^i - p_{tx}^i) - (p_{ex}^1 - p_{tx}^i) \text{ for } i = 1..N \tag{5.3}$$

and

$$D_{i,y} = (p_{ey}^i - p_{ty}^i) - (p_{ey}^1 - p_{ty}^i) \text{ for } i = 1..N \tag{5.4}$$

The entries in the first row of D are zero as the first image is the basis onto which all others are stacked. The rest of the images are each shifted by a linear transform, down to the sub-pixel to create translated frames that have the shifted coordinates as their central pixel. This is done using the MATLAB Image Processing Toolbox algorithm 'imtransform', supplied with the offsets in the x and y direction $D(i,1), D(i,2)$. Each FSS processed star streak free image (I_{ns}^i) is shifted to a translated image (I_{tr}^i) by:

$$I_{tr}^i = \text{imtransform}(I_{ns}^i, D(i,1), D(i,2)) \tag{5.5}$$

The stacked image I_{st} is then simply the sum of all the translated images as follows:

$$I_{st} = \sum_{i=1}^{N} I_{tr}^{i} \tag{5.6}$$

Figure 5.10 shows the sum of four TRM images of a GPS satellite, stacked with and without drift compensation. By applying relative motion drift compensation the RSO signature from each image is additive. The resulting signal (red circle in the right hand image of Figure 5.10) becomes more pronounced in contrast to cosmic ray hits and other noise artefacts (highlighted in the green circles). This is done without having a-priori knowledge of the RSO location in each image.
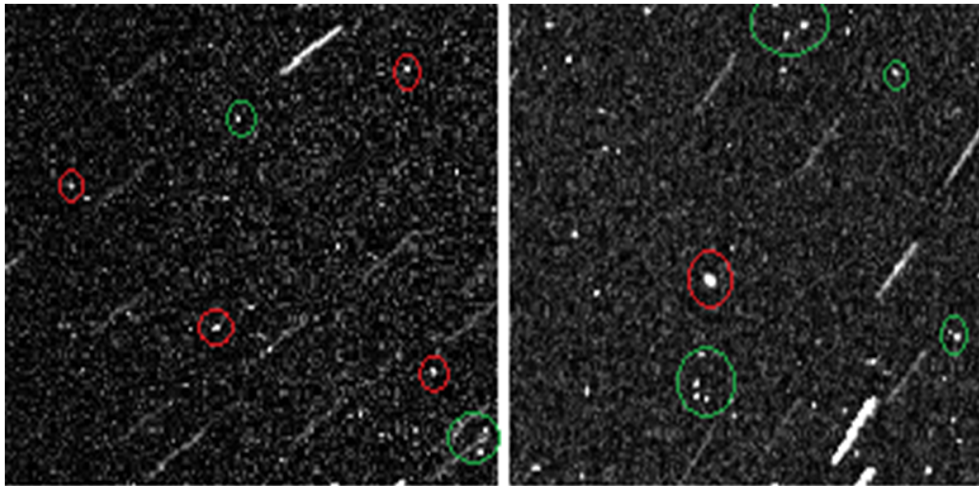
Figure 5.10: Signatures from 6 images stacked before (left) and after (right) applying drift compensation. RSO locations circled in red, noise artefacts (cosmic ray hits) in green.

The compensations applied to each image stacked in Figure 5.10 are listed in Table 5.3.

Table 5.3: Relative rates between NEOSSat and a GPS satellite and the offset values (drift matrix) in pixels for the images stacked in Figure 5.10.

Image	Time Elapsed	$\dot{\text{RA}}$	$\dot{\text{DEC}}$	$D_{i,x}$	$D_{i,y}$
	(s)	(arcseconds/s)	(arcseconds/s)	(pixels)	(pixels)
1	0	-12.8	-29.8	0	0
2	30	-12.3	-31.2	-14.87	2.00
3	60	-11.9	-32.0	-28.28	-1.17
4	90	-11.4	-33.8	-33.94	-3.31
5	120	-10.9	-35.1	-29.39	-2.94
6	180	-9.8	-37.6	-7.67	-3.77

5.5.1 RSO Detection in the Stacked Frame

In a stacked image with star streaks removed and RSOs presumably stacked in a common location, an image segmentation is performed labelling all possible signatures in the stacked image. For the stacked image segmentation, a signal cut-off of $SNR_{cut} = 3\sigma_{bg}$ is used, all sources passing this cut are then investigated in each individual image. For an N image sequence, an SNR cut-off at the persistent signal location can be reduced to SNR_{cut}/N.

As a final check for RSO detection, a persistent signal at the location of the stacked signal has to be found in each individual image. This discrimination screens out cosmic ray artefacts as false positives as they appear in random locations, and only contribute signal to one image in a sequence. By compensating for the relative motion between NEOSSat and the RSO, the stacking algorithm is able to increase the signal to noise ratio of a detectable RSO in an N image sequence by a factor of $\sqrt{N}$ compared to analysing each image individually. A $\sqrt{N}$ SNR increase is achieved through stacking as each added image effectively increases the exposure time duration of signal integration to N times, while the noise increases as the root of the exposure length.

5.5.2 Centroiding

Once a persistent signal is identified its centroid in each image is then determined. This is performed by taking a box around the persistent signal location in each image totalling 40 pixels per side (then reduced by the binning level if present). This large size is not chosen to search for the RSO again in each image but to ensure that the full RSO signature is scrutinized as RSO signatures can be elongated due to TRM rate mismatches (Figure 4.4).

Again, on each small region, an image segmentation is performed and sources are discriminated for minimum possible size, minimum length frame rate mismatches and for PSF like shape tapering to ensure that the signal is not a cosmic ray hit. A source passing all these criteria, and persistent in each image is determined to be an RSO. Its centroid is determined from a centre of mass algorithm weighing each pixel contribution in the masked region of the detected source to the total number of pixels in the source. This provides an (X,Y) coordinate of the RSO source at the middle exposure time, which is then converted into sensor centric right ascension and declination from the astrometic solution calculated by PinPoint.

5.6 Post Processing

5.6.1 Observation Correlation

When an RSO is detected in an image, it is not necessarily assumed to be the RSO that was tasked to be imaged. Instead, the metric position of the RSO is measured against all objects in the SSN catalog to determine which object it most likely is. This process is known as correlation and is done using the SGP4 propagator described in Section 5.1.2. This is performed because many images contain more than one RSO, especially in the GEO region where satellites can be heavily clustered due to stationkeeping arrangements used for GEO services (eg. the close clustering of Anik and Astra geostationary satellites in Figure 2.4). Also, correlation scrutinizes the detected location

of an RSO and provides a further method to ensure no false positives are generated (eg. no observations from cosmic ray hits).

For images with only one observation, correlation is performed by propagating the deep space portion (everything above LEO, here as RSOs with a period of more than 225 minutes) of the TLE catalog to the observation time, and assembling the locations and rates of all RSO candidates near the field of view. RSOs with angular rates prohibiting the motion seen by the observation between the frames are discarded, these would be RSOs whose motion across images could not have reasonably stacked to a persistent signal. Correlation candidates were limited to within 1000 arcseconds between the predicted RSO position from the TLE and the detected RSO position in the image frame. This angular cut-off corresponds to a separation distance of about 200 km at geostationary ranges, well above the position error of a well maintained TLE, but not an unreasonable separation for an RSO that may have manoeuvred. The nearest candidate RSO to the observations remaining after these cut-offs is then chosen for correlation.

For images with multiple detected RSOs, such as geostationary satellite clusters, a nearest neighbour approach does not suffice. Instead, the geometric configuration of the detected RSO is compared to all possible geometric permutations of similar number groups of candidate RSOs. This is simplified by projecting the RSO locations onto the celestial equator and examining the relative RA between each possible group.

5.6.2 Aberration correction

A common error encountered when supplying observations are errors compensating for stellar aberration. The last step before creating B3 Type 9 observations is to correct the apparent position of the RSO's measured RA and DEC for stellar aberation.

Planetary aberration is a phenomenon known since the beginning of stellar astrometry [51] and is the combination of the aberration of light (due to

79

Earth's and NEOSSat's combined velocity) and light-time correction (due to the RSO's motion and distance), as calculated in the rest frame of the Solar System. Both are determined at the instant when the RSO's light reaches NEOSSat.

A method to correct right ascension (α) and declination (δ) apparent positions for stellar aberration is detailed in [52]. The correction begins with the J2000 unit position vector ($\mathbf{r}_{app}$) from the RA and DEC of the observation:

$$\mathbf{r}_{app} = \begin{pmatrix} \cos(\alpha)\cos(\delta) \\ \sin(\alpha)\cos(\delta) \\ \sin(\delta) \end{pmatrix} \tag{5.7}$$

At each NEOSSat observation time the Earth's barycentric velocity is calculated using the NOVAS Kepler scriptable software (http://www.ascom-standards.org/). The J2000 NEOSSat velocity is retrieved from the image FITS header. Combining the Earth's $\mathbf{V}_E$ and NEOSSat's $\mathbf{V}_N$ velocities we get the velocity of the observer in the Barycentric frame $\mathbf{V}_b$, scaled to the speed of light c:

$$\mathbf{V}_b = (\mathbf{V}_E + \mathbf{V}_N)/c \tag{5.8}$$

The Lorentz scaling factors are:

$$\beta = \sqrt{1 - |\mathbf{r}_{app} \cdot \mathbf{V}_b|^2} \quad and \quad \chi = \frac{\mathbf{r}_{app} \cdot \mathbf{V}_b}{1 + \beta} \tag{5.9}$$

And the corrected unit position vector is:

$$\mathbf{r}^{'} = \beta\mathbf{r}_{app} + (1 + \chi)\mathbf{V}_b \tag{5.10}$$

As $\mathbf{r}^{'}$ is already normalized we can now compute the corrected right ascension and declinations (α') and (δ'):

$$\alpha' = \mathrm{atan2}(r'_x, r'_y) \tag{5.11}$$

$$\delta' = \text{atan}\left(\frac{r'_z}{\sqrt{r'^2_x + r'^2_y}}\right) \tag{5.12}$$

With an aberration corrected RA and DEC a B3 Type 9 format observation can now be made.

6 Metric Results and Limiting Magnitude

In this chapter the metric assessment of HEOSS observations produced by SQUID3 is presented, along with an assessment of the NEOSSat sensor sensitivity in a space surveillance capacity. The implications of these findings on the orbit determination process is also discussed, along with sources of uncertainty.

6.1 Metric Observations

In the fall of 2016 the OPS6 version of NEOSSat's flight software enabled routine collection of HEOSS TRM imagery and NEOSSat began a metric accuracy assessment campaign by tasking imagery on GPS satellites, which are excellent calibrators for space surveillance sensors. From the period of 15 September 2015 to 3 February 2016, GPS satellite imagery was acquired for metric data assessment in both 1x1 and 2x2 binning modes. Each imaging sequence was processed by SQUID3. In total 414 observations were produced in 1x1 binning and 183 observations in 2x2 binning. Table 6.1 provides a summary of the observations that came from individual GPS satellites.

Metric observational data produced by SQUID3 are B3 Type 9 formatted text files, which can be analysed by ODTK. ODTK can determine relative accuracy of observations with respect to reference ephemerides to below the

Table 6.1: GPS satellite metric observation counts.

SSN #	29601	32260	32384	35752	36585	37753	39166	39741	40105
# Obs. (1x1)	4	8	60	37	4	101	80	83	37
# Obs. (2x2)	0	5	37	16	7	0	0	100	18

arcsecond level provided its Earth orientation parameters are kept up to date. This provides insight or an indication of the accuracy of the measurements produced by the HEOSS science mission.

For GPS calibration satellites, 24-hour precision ephemerides are downloaded for the day of each observation from the National Geodedic Service webpage [53]. This data is available as 'SP3' formatted text files, consisting of time, position, and velocity of the GPS calibration satellite orbit, which can be converted into AGI formatted ephemeris files and read into ODTK. The quality of these reference orbits is stated as accurate to within 2.5cm, well below any other contributions to NEOSSat's error budget and much smaller than the physical size of a GPS spacecraft bus.

Once a reference GPS ephemeris is uploaded to ODTK, the observations are processed with ODTK's Extended Kalman Filter in 'filterless mode', where observations are not used to update the observed satellite's orbit. In filterless mode the observation residuals to the reference orbit are computed and output. Residuals are the deviation of a measurement to truth data, ie:

$$\begin{pmatrix} \Delta\alpha \\ \Delta\delta \end{pmatrix} = \begin{pmatrix} \alpha_{measured} - \alpha_{true} \\ \delta_{measured} - \delta_{true} \end{pmatrix} \tag{6.1}$$

where the truth observations are modelled (apparent) observations of the calibration satellite's position. By analyzing the statistics of $\Delta\alpha$ and $\Delta\delta$ a space surveillance sensor's accuracy and biases can be assessed.

For each day's worth of TRM GPS observations that were collected an ODTK scenario containing the reference ephemerides of the GPS satellites was created. The B3 Type 9 data file contained NEOSSat's ECEF Cartesian

position, which is used as the sensor location for each observation. Residuals for each observation in terms of right-ascension and declination were outputted and compiled.

The HEOSS metric error budget, calculated in Section 4.3 consisted of uncertainty contributions from sensor location, observation timing, RSO centroiding, and boresight pointing. The true metric accuracy of the sensor is determined from investigating the bulk statistics of observation residuals. Figure 6.1 shows the histograms of residuals in RA and DEC for both 1x1 and 2x2 binned images.
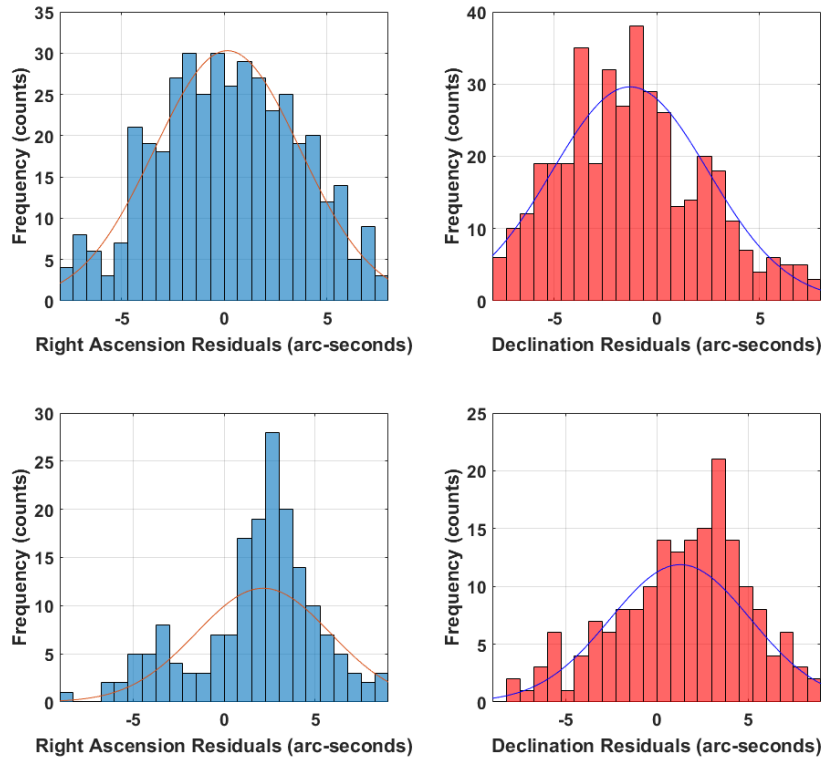
Figure 6.1: (Top): RA and DEC residuals for GPS observations and modelled Gaussians for 1x1 and (bottom): 2x2 binning using TRM imagery.

Table 6.2 shows the bulk statics from the RA and DEC component residual analysis of Figures 6.1. They are both modelled as Gaussian distributions, and have a similar standard deviation in either component.

Table 6.2: Bulk RA and DEC residual error statistics, all values in arcseconds.

	RA	DEC	RA	DEC
	1x1 binning		2x2 binning	
σ	3.5	3.8	3.7	3.8
Bias	0.15	-1.3	2.1	1.3

One noticeable feature in Figure 6.1 is a slight bias increase in 2x2 residuals, while no substantial bias is present in 1x1 residuals. An increase in the binning mode of the imagery should create a corresponding increase in centroiding error as the pixel sizes are larger, and a small error increase from astrometry, but these sources of error should be random, not biased. One possible explanation for the increase in bias in 2x2 imagery is that the imaging campaign took fewer 2x2 images overall, and was typically tasked day to day on the same GPS satellites near the same times. This means that the relative rates of the GPS satellites to NEOSSat were often repeated and not distributed randomly. In this type of situation, an error or bias in timing could manifest itself as a bias in residual histograms, as positions would consistently be offset in the same direction.
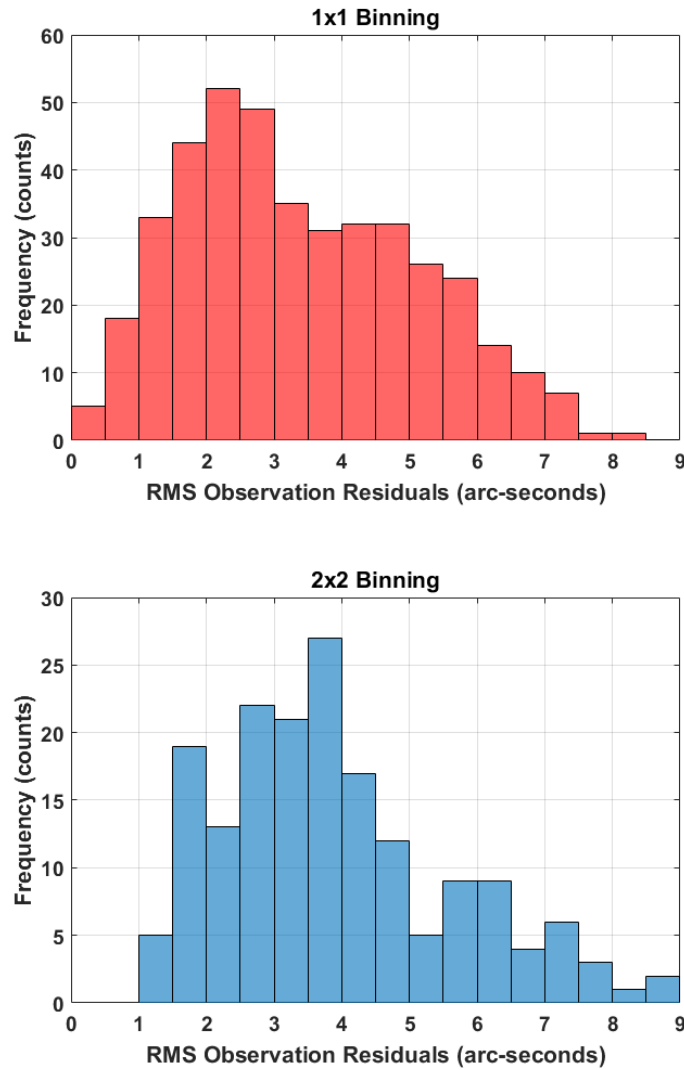
Figure 6.2: (Top): Total RMS residuals for GPS observations for 1x1 binning (bottom): 2x2 binning using TRM imagery.

Figure 6.2 shows the combined total angular error of each observation. Like the metric results from SBV (Figure 3.6), the combined RA and DEC

RMS residuals in Figure 6.2 are more tightly spread than their individual components. They are modelled as a Rayleigh distribution, with a mean error of 2.8 arcseconds for 1x1 binned images and 4.4 arcseconds for 2x2 images (Table 6.3). This is about an arcsecond larger than the predicted error budget calculated in Section 4.3, reproduced in Table 6.4. Both of these values are in-line with SSN accuracy requirements for non-traditional sensors to contribute metric data for space surveillance.

Table 6.3: Total RMS residual error statistics, all values in arcseconds.

Total residual	Mean	Stdev
1x1 binning	2.76	1.71
2x2 binning	4.37	1.79

The mean metric accuracy of HEOSS raw TRM imagery derived from SQUID3 image processing has been calculated to be a 2.76 arcseconds, and 4.37 arcseconds at 2x2 binning.

Table 6.4: NEOSSat TRM error budget and metric performance.

Binning mode	Error budget (arcseconds)	Total residuals (arcseconds)
1x1	1.75	2.76
2x2	3.12	4.37

NEOSSat's 2.76 arcsecond accuracy in 1x1 binned imagery would provide measurement precision of approximately 550 metre accuracy at geostationary range. This is suitable for orbit determination and general catalog maintenance as it represents an improvement on a TLE's at epoch error of approximately 1 km. Furthermore each successive observation would provide a further orbital accuracy improvement. One should note that the small biases present were for GPS observations and may be at different levels for GEO observations. In the GEO regime, a positive bias in RA would result in an eastward longitude offset after orbit determination, while a positive bias in DEC would

manifest as an northern inclination offset.

6.1.1 Sources of Metric Error

While NEOSSat's error budget was calculated in Section 4.3, there are some factors that could contribute to the higher residuals determined in this assessment. After launch of NEOSSat, several in-orbit findings affecting system accuracy were found and are discussed below.

Timing

Timing errors are assumed to be negligible, as NEOSSat's clock is calibrated with GPS observations and the triggering of CCD exposure start and stop times is recorded down to the millisecond by the read-out electronics. That said, a method of calibrating NEOSSat's timing on orbit is unavailable. On the ground it is feasible to calibrate an imaging systems timing by imaging the output of a known time varying signal (say from an oscilloscope [9]) and measurement the differences in timing offsets. Such a calibration was not done before launch, and no reference objects with timing events known to millisecond accuracy are available on orbit.

NEOSSat routinely imaged RSOs at angular rates up to 60 arcsecs/s and every millisecond of error in timing could lead up to 0.06 arcseconds of metric error. Furthermore as NEOSSat is a space-based platform its sensor location is time dependent, any errors in observation timing would be compounded by an error in NEOSSat location.

One should note that the metric assessment was done on GPS satellites, orbiting in MEO with a 12 hour period at roughly half the distance of GEO satellites. As the primary RSOs of interest to HEOSS are in GEO the relative rates experienced in routine imaging would be lower than for GPS satellites. Any errors in timing would therefore be less pronounced overall when tracking GEOs.

Centroiding

When centroiding an RSO, the accuracy is maximal when the signature is most compact, ie. when NEOSSat's angular slew rate is best match to that of the RSO. As RSO signature elongates due to angular rate mismatches centroiding is made more difficult, not only because the spatial extent of the signature is larger, but because its SNR is decreased some signal may be cut during thresholding leaving an incomplete signature to be centroided. Furthermore, if the angular acceleration of the RSO across the image plane changes substantially during the exposure interval then the true location of the RSO at the middle exposure time of the image is not directly in the RSO signature centroid.

Accuracy of centroiding is also dependent on the PSF, or straddle factor, of an imaging system. As shown in Figure 6.9, NEOSSat's PSF was not static, but dependent on bus temperature. Thermal defocus of NEOSSat's telescope broadens the PSF shape and, in the worst case scenario, can double the FWHM of the PSF (nominally 6.2 arcseconds) to 12.5 arcseconds. While care was taken during before imaging campaigns to maintain NEOSSat in an ideal focus, some degradation of the PSF occurred during HEOSS operations.

Observation Corruption

Observations could have been corrupted by cosmic ray hits that overlapped the RSO signature, leading to residual biases in unpredictable ways. Contributions from hot pixels could also corrupt a centroid value. While care was taken to remove hot pixel influences via minimum dark frames, not all images could be background reduced in this fashion, leaving hot pixels intact. Figure 6.3 shows a detected RSO signature from the GPS metric data campaign from an image that was not minimum dark frame subtracted. One can see how the inclusion of hot pixels could skew the centroid centre of mass value for this signature. In this particular observation the metric residuals were 1.6 arcseconds in RA and 12.5 arc-seconds in DEC.

Hot pixel corruption was seen as a limiting factor to SBV metrics [38], and
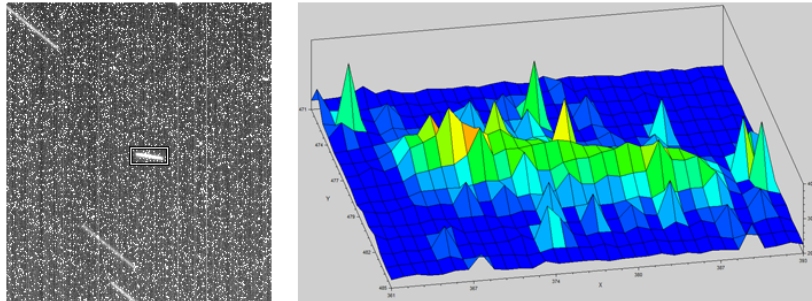
Figure 6.3: Corruption of an RSO signature from hot pixels.

methods were introduced to mitigate them. For HEOSS imagery, the images that could not be processed with minimum dark frame subtraction could be removed for consideration for metric data production. This would increase the overall metric accuracy of HEOSS observations, at the cost of throughput of the sensor. Alternatively, when minimum dark frames are unavailable imagery could be processed with a median value kernel filter. This would degrade the SNR sensitivity to sources in the image but not degrade metric accuracy substantially given NEOSSat's oversampled PSF.

The star streak subtraction algorithm, although designed to completely erase a star signature, leaving any overlapping signatures (such as an RSO) intact [30] sometimes leaves portions of star streaks present in an image. The cause of this is either improper modelling of the star streak length and orientation from Fourier processing (Section 5.3), or from an inaccurate estimate of the PSF of an image.

B3 Type 9 Precision

The B3 Type 9 format uses a limited number of digits to preserve RA and DEC values. RA values are measured in hours, minutes and seconds, with one decimal place of precision. This leads to a worst case truncation error (half of

90

the last digit's precision) in RA of:

$$\left(0.1 * 15\frac{\text{deg}}{\text{hr}}\right)/2 = 0.075 \quad \text{arcseconds} \tag{6.2}$$

For DEC values the data is stored in decimal degrees, with four decimal places of precision, giving a truncation error of:

$$\left(0.0001° * 3600\frac{\text{arcseconds}}{\text{deg}}\right)/2 = 0.18 \quad \text{arcseconds} \tag{6.3}$$

While the truncation errors are small even in the worst case they contribute a significant portion to the metric residual assessment. This could be overcome by using a more modern format for metric data, such as the GEOSC format which retains more decimal precision, but B3 Type 9 format remains the standard for transmitting observations to the US SSN.

6.2 Limiting Magnitude

A test of NEOSSat's sensitivity capabilities was performed by tracking small, faint space objects. Stellar visual magnitudes are included in the UCAC3 catalog and during astrometry a photometric calibration is performed computing the zero point magnitude of an image, from which detected object apparent magnitudes can be calculated using Equation 3.4.

Figure 6.4 shows the histogram of the apparent visual magnitudes of detected GPS satellites in 1x1 binning during the metric imaging campaign of Section 6.1.

From the GPS observation campaign, one can observe that this class of RSOs is detectable by SQUID3 down to 15th magnitude (Figure 6.4). This data was generated with an SNR cutoff of 4.3, chosen to reject false positives for metric assessment. The data was also taken mostly at lower phase angle where access times between NEOSSat and a GPS satellite were prolonged, and the RSOs at their brightest. The 15th magnitude limit of the GPS imaging

91
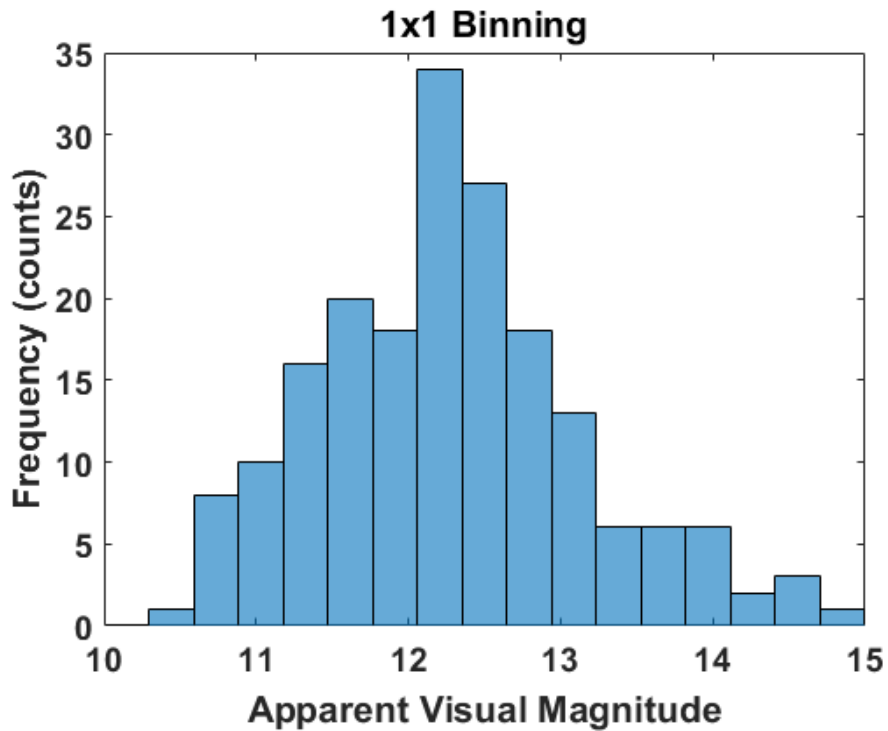
Figure 6.4: Histogram of apparent visual magnitudes of GPS satellites in 1x1 binning.

campaign match closely with the limiting magnitude of SBV imaging all RSOs (Figure 3.10).

To determine the true limiting magnitude of NEOSSat in TRM, a series of tracks on faint RSOs was taken at various phase angles. Because of their small size and deep space orbit the RSOs chosen were early Anik-A class satellites: geostationary satellites with a small cylindrical buses now in graveyard orbits just beyond the geostationary belt. There were three Anik A class satellites (details in Table 6.5), each sharing the widely used spinning geostationary Hughes Aircraft Company model 333 satellite bus (Figure 6.5). Each satellite's bus was a cylinder 1.9 meters in height and 1.81 meters in diameter. An imaging campaign on 27 October, 2015 was focused on these satellites. In this

test, NEOSSat imaged the satellites from a minimal solar phase angles within the CVZ up to 90 degrees solar phase angle, anticipating that the satellites would fade due to the changing illumination conditions.

Figure 6.5: Anik-A1 satellite before launch.

Table 6.5: Anik-A class satellite details.

Satellite	Anik-A1	Anik-A2	Anik-A3
SSN #	6278	6437	7790
Launch Date	10.11.1972	20.04.1973	07.05.1975

Imagery from these trials were processed with SQUID3, which was first run with an stacked image SNR cut-off of 4.3, which was the value used in the concurrent GPS metric data collection campaign. Of the 120 images taken on 27 October, 2015 only three observations were detected at this setting. The stacked image SNR cut-off was lowered to 2.0 and detections were manually verified for false positives and 33 observations were formed, the histogram of

which is presented in Figure 6.6.
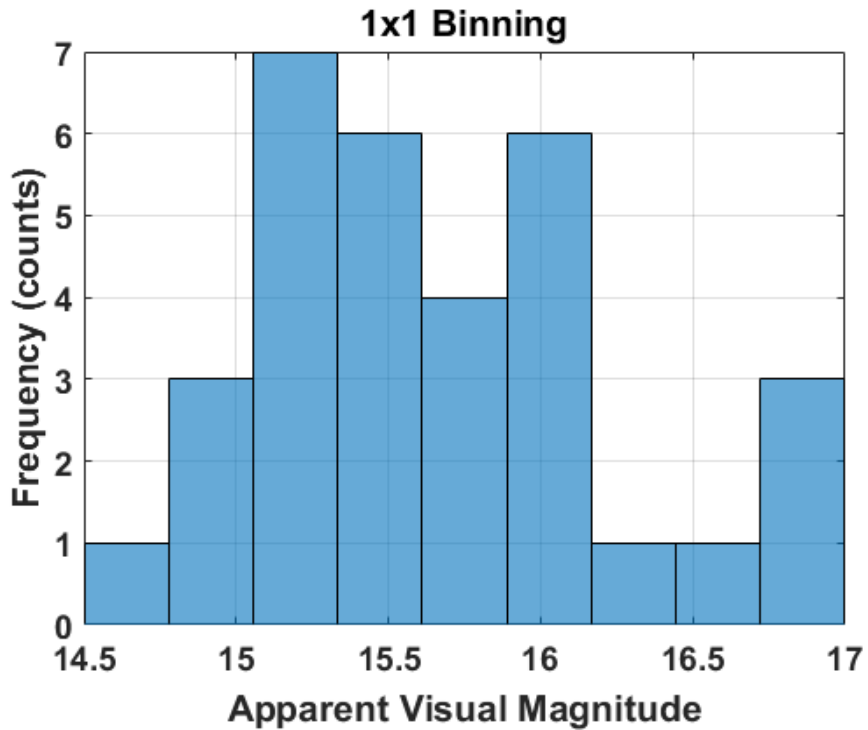
Figure 6.6: Detected apparent visual magnitudes of Anik-A class satellites on 27 Oct 2015.

To illustrate the expected limiting magnitude of this trial Table 6.6 gives the theoretical limiting magnitude M_v using NEOSSat's detectability modelling parameters from Section 4.4 using Equation 3.7 with values of SNR_{cut} of 4.3 (used for automated HEOSS SQUID3 processing), 3.0 and 2.0 (used in this trial with manual verification) for 5 second exposure TRM images.

For the SNR_{cut} of 2.0 used in this trial, the maximum detected apparent visual magnitude was 16.9, in excellent agreement with the theoretical predication of magnitude 16.8. The automated image analysis SNR_{cut} of 4.3 used in GPS image processing producing Figure 6.4 only produced observations down to magnitude 15, but the GPS satellites were not imaged at high phase

Table 6.6: Theoritical limiting magnitude of 5 second TRM exposures at various SNR detection cut-offs.

SNR_{cut}	V_{lim}
4.3	15.9
3.0	16.3
2.0	16.8

angle in that trial. Furthermore the initial processing run of Anik-A data only produced three observations at an SNR_{cut} of 4.3, while data in in Table 6.7 show only three observations with apparent magnitude brighter than 15. This further shows that SQUID3 can produce observations meeting theoretical detectability limits at a given SNR_{cut}.

Figure 6.6 show detections of brightnesses down to almost at 17th magnitude are possible in ideal case HEOSS imaging. Figure 6.7 show the apparent visual magnitudes of detected Anik A satellites as a function of their solar phase angle. As expected from Figure 4.8, the RSOs are at their dimmest near a phase angle of 90 degrees. The large spread of visual magnitudes at a given phase angle seen in Figure 4.8 is likely due to the fact that the Anik-A class satellites have long since stopped being attitude stabilized and their rotation presents a changing reflecting area to NEOSSat.

Table 6.7: Detected observation data for Anik-A satellites taken on 27 Oct. 2015.

SSN	Length	Zero Point	App. M_v	Ang. Rate	Phase Angle	Exp.
ID	(pixels)			(arcsec/s^2)	(degrees)	Time (s)
6278	5.0	20.72	15.29	45.59	58.50	4
6278	3.61	21.36	16.10	44.88	59.47	4
6278	4.24	21.40	16.24	46.04	60.51	4
6278	4.47	21.39	15.56	39.65	61.59	4
6278	2.24	21.30	16.82	46.71	-63.18	4
6278	4.47	21.12	16.01	49.36	-62.24	4
6278	4.47	21.21	15.69	51.68	-61.30	4
6278	5.83	21.18	15.51	47.02	-60.38	4
6278	2.83	21.46	16.01	43.47	-88.27	4
6278	5.66	21.30	15.41	50.90	-87.39	4
6278	5.0	21.24	15.70	51.17	-86.50	4
6437	4.47	21.42	16.94	36.48	-88.82	5
6437	4.24	21.49	16.08	34.10	-87.10	5
6437	4.47	21.30	16.74	39.53	-86.29	5
6437	5.83	21.20	15.45	50.03	-22.52	4
6437	5.39	21.03	15.30	48.20	-21.25	4
6437	5.0	20.34	14.86	50.16	-19.96	4
6437	7.21	20.69	15.16	45.56	-13.41	5
6437	7.81	20.85	14.52	46.80	-12.20	5
6437	7.81	21.15	15.06	43.67	-11.05	5
6437	6.40	20.55	14.78	43.12	-10.01	5
7790	7.07	21.32	15.64	47.06	-68.44	5
7790	5.0	21.30	15.57	46.02	-67.53	5
7790	7.62	21.23	15.19	47.37	-66.59	5
7790	7.81	21.07	15.15	44.90	-65.65	5
7790	5.83	21.14	15.42	41.83	-60.42	5
7790	6.40	21.13	15.15	44.31	-59.71	5
7790	7.62	21.27	15.78	43.74	-59.06	5
7790	7.21	21.15	15.96	44.26	65.14	5
7790	5.0	20.99	15.23	43.61	65.78	5
7790	5.0	21.36	15.97	45.57	66.49	5
7790	4.47	21.40	16.55	42.56	67.28	5
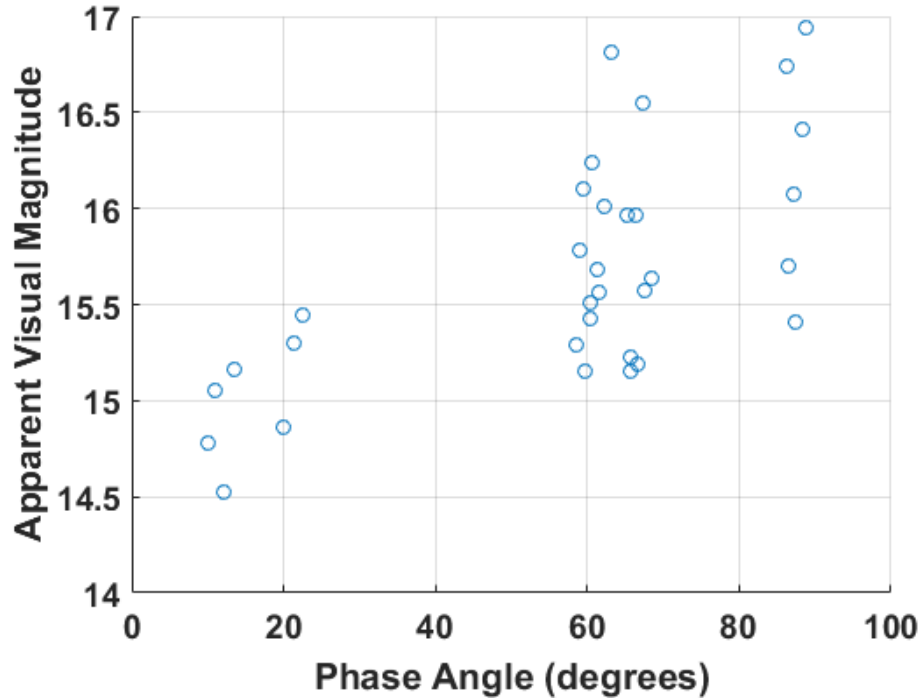
Figure 6.7: Apparent visual magnitude plotted against solar phase angle.

6.2.1 Sensitivity Performance

The results of the limiting magnitude assessment show that NEOSSat is limited to 15th magnitude under best case circumstances in automated detection, with 17th magnitude achievable with manual verification. From Equation 3.2, the detection of a 15th magnitude object is equivalent to detecting a 0.4 meter diameter object at geostationary range, with 100% reflectivity and zero phase angle (idealized conditions maximizing brightness). This is below the size of typical geostationary satellites. Under more realistic conditions, such as a reflectivity ρ of 0.2 and phase angle of 30 degrees this diameter increases to 1.7 meters, about the size of the Anik-A class satellites imaged. Figure 6.7 reflects this showing NEOSSat detected objects of this size at 15th magnitude at similar phase angles. This shows that NEOSSat is suitable for space surveillance

97

activities of active and inactive satellites in the geostationary regime, however the majority of newly discovered smaller debris objects are at magnitude 17th or fainter [54], cannot be tracked by NEOSSat.

In HEOSS trials the SNR_{cut} was set at 4.3 and produced few false positive observations within a reasonable correlation limit. Rare cases where false positives were generated at this limit were from cosmic ray signatures while NEOSSat was tasked to image while near the SAA.

The influence of RSO signature length on each image, due to rate mismatches during exposures, can be seen in Figure 6.8. As expected with TRM imagery, the more compact the RSO signature, the higher the probability of detection as the signature is spread over fewer pixels. Most of the very faint objects detected in this campaign had good rate matches, whereas when the signature was spread over many pixels, only higher magnitude objects could be detected. In Figure 6.8 the length in pixels is computed from the maximum length of the signature containing mask remaining after the SNR cut of 2.0 was applied.

Lastly, the limiting magnitude of the system is dependent on NEOSSat's focus level. As mentioned in Section 6.1.1, care was taken to ensure that NEOSSat was placed in an attitude that ensure good focus prior to imaging campaigns, however some internal cooling likely took place during TRM operations. Figure 6.9 shows the evolution of NEOSSat's focus for a series of 2 second exposures taken over two days in late 2014. During this trial the satellite was slewed from a southward pointing (with a large surface NEOSSat body area exposed sunward), to an anti-sunward attitude (with a minimum surface area exposed to the sun). It remained in that orientation for 24 hours and was slewed and back to its original pointing. The average thermal load decreases in anti-sunward attitudes (blue line) and correspondingly degrades the focus. The CCD temperature is used as a proxy for telescope payload temperature in this figure, as no temperature data for the payload structure is available in NEOSSat telemetry.
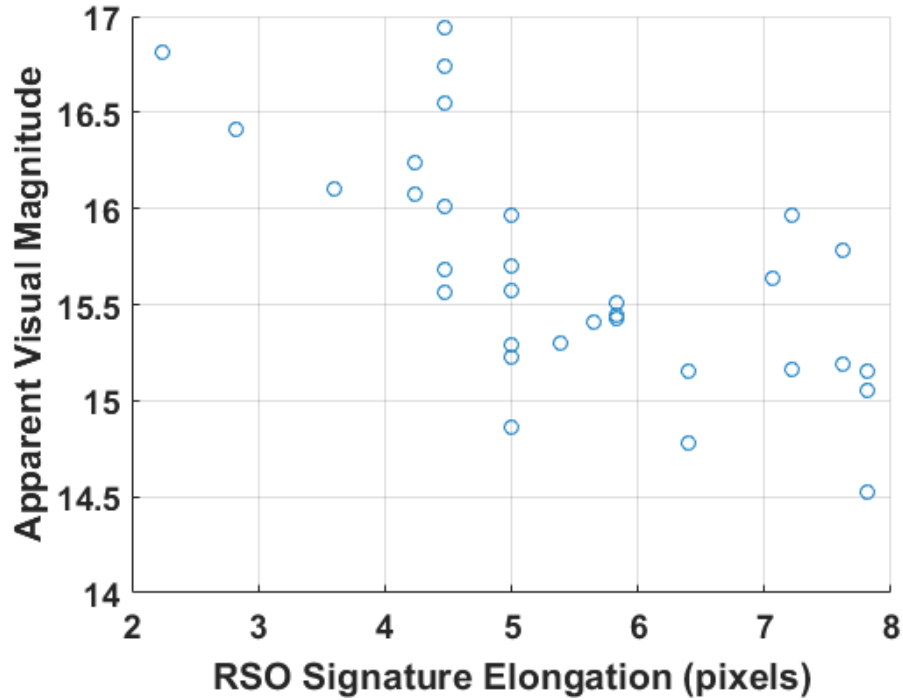
Figure 6.8: Apparent visual magnitude of Anik A satellites as a function of RSO signature length.

To measure the focus levels in Figure 6.9, the fraction of intensity of the brightest pixel in a detected star to its total intensity is used. A well focused image will have more energy deposited on the central pixel of a star, and this value will diminish as focus devolves. From the curve it can be seen that it takes about 12 hours for NEOSSat to reach peak focus from a defocused state and vice versa. If NEOSSat imaged in a completely defocused state this in effect causes a doubling of the point spread function from 6.25 to 12.5 arcseconds, which lowers the straddle factor k_f in Table 4.2, going from a value of 1.85 to 0.05 and effectively changing the theoretical limiting magnitude at an SNR_{cut} of 3 from $M_v = 16.3$ to $M_v = 15.12$ for a four second TRM exposure in a defocused state.
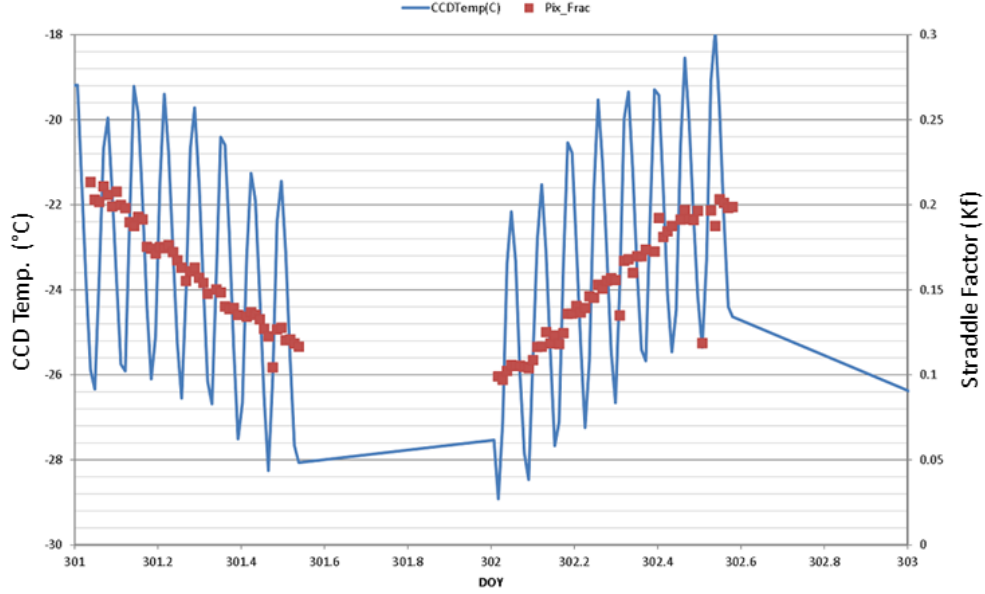
Figure 6.9: NEOSSat's PSF evolution: fraction of enclosed energy contained in the central pixel of a star (red blocks), over two days variation of CCD temperature (blue).

6.3 Summary of Results

This chapter analysed the performance of NEOSSat in a space surveillance capacity. Through residual analysis of metric data between HEOSS observations produced by SQUID3 processing of TRM images and highly accurate reference GPS orbits NEOSSat's metric accuracy was determined to be 2.8 arcseconds for 1x1 binned images and 4.4 arcseconds for 2x2 images at a 1σ confidence level. These values are in excess of NEOSSat's metric error budget by 1 arcsecond, with unmodelled sources of metric error including thermal defocus of the telescope, timing, and RSO signature corruption.

The limiting magnitude of NEOSSat when imaging routine HEOSS observations at an SNR cut-off of 4.3 is 15th magnitude, and observations were shown to be possible down to 17th magnitude with a relaxed SNR cut-off of 2.0. Both of these values are in excellent agreement with the predictions calcu-

lated in Section 3.5. While this limiting magnitude does not permit detection of small debris objects in GEO, NEOSSat's metric accuracy and sensitivity levels make it a suitable platform for performing SSA observations on deep space satellites.

7 Conclusion

The primary aim of this work focused on implementing and evaluating an image processing system for NEOSSat HEOSS imagery. This was done with the intent to validate a microsatellite as a suitable sensor platform for space surveillance. To this end NEOSSat's capabilities to acquire TRM imagery were assessed and tools to task NEOSSat to image deep space RSOs developed. For NEOSSat TRM imagery, a novel image stacking technique was employed to detect RSOs which simultaneously increased automated SNR detectivity and rejected energetic cosmic ray signatures as false positives.

The secondary aim of this thesis, to assess the quality of metric data produced by NEOSSat, was accomplished by a comparison of TRM observations to reference GPS ephemerides. Finally the limiting magnitude of NEOSSat was determined.

This work has shown that space surveillance is feasible from a microsatellite. The remainder of this chapter summarizes the results from this thesis and suggests recommendations for future work.

7.1 Summary of Conclusions

7.1.1 HEOSS Image Processing

The primary aim of this thesis was to develop a method to produce metric observations of RSOs from NEOSSat's space-based space surveillance imagery in a manner that maximized metric accuracy, utilized all available imagery,

and did not produce false positives from the energetic cosmic ray background not present in ground based imagery.

Precision metric observations, dependent on platform location information, require precise ephemerides for NEOSSat at all observation times. These were determined from on-board GPS measurement processing. Background removal was performed on TRM imagery by creating a median dark frame from each TRM sequence which was then subtracted from each individual image.

Star streak detection was performed with a matched-filter based algorithm, seeded by a signature model derived from a Fourier transform. Images were astrometrically solved using the centroids of detected stars to RSS position residuals of 1.26 arcseconds for 1x1 binned imagery and 2.31 arcseconds for 2x2 binned imagery.

RSO detection used an image stacking technique that shifts images relative to the RSO motion between frames, combining RSO signal additively, independent of spacecraft motion. This method maximized sensitivity of observations while discriminating from false positive cosmic ray signatures. This permitted RSO source detection with an SNR cut-off of 4.3 in automated image processing and down to 2.0 with manual verification. Once an RSO was detected, it was correlated with a known object in the SSN catalog and metric data products created.

7.1.2 HEOSS Observation Metric Performance

HEOSS's metric accuracy was assessed from a prolonged imaging campaign of GPS satellites from September 2015 to February 2016. HEOSS TRM images were processed with SQUID3, producing metric right-ascension and declination data products consisting of 414 observations in 1x1 binning and 183 observations in 2x2 binning. These observations were calibrated against known GPS ephemerides using ODTK6. In 1x1 binned images observations have a mean residual accuracy of 2.8 arcseconds and in 2x2 binned images

observations have a mean residual accuracy of 4.4 arcseconds. Both values show NEOSSat's metric accuracy is comparable to its error budget and meet SSN accuracy requirements for non-traditional sensors contributing to catalog maintenance.

To improve metric data statistics, available HEOSS data could be reprocessed to reject imagery that could not be processed via minimum dark frames. These frames are susceptible to corruption by hot pixels. Alternatively, to maintain reasonable throughput of the sensor, images that could not be minimum dark frame subtracted could be pre-processed with a median kernel filter, removing most single pixel corruption influences.

7.1.3   HEOSS Limiting Magnitude

The limiting magnitude for HEOSS imagery was determined to be 15th magnitude through automatically detected observations of GPS satellites. This detection limit was at an integrated SNR cut-off of 4.3 to ensure no false positive detections. With an SNR cut-off of 2.0 and manual verification of observations, HEOSS was able to detect objects down to 17th magnitude from an imaging campaign of Anik-A class geostationary satellites.

NEOSSat's limiting magnitude performance is in line with its hardware's theoretical capabilities. Its automated detection of 15th magnitude RSOs is equivalent to detecting a 1.7 meter diameter object at geostationary range, making it suitable for routine RSO tracking and catalog maintenance in this regime, but less suitable for tracking debris sized objects in GEO orbit.

7.2   Recommendations for Future Work

Several avenues for future research to refine the results obtained in this thesis are recommended and included below:

1. *Geostationary Metrics:* An assessment of metric accuracy using GEO calibration satellites could be performed. The increased range of geo-

stationary orbits should give a slightly better overall metric accuracy. Reference ephemerides for GEO metric calibration could come from collaboration with a spacecraft operator, which often produce precision ephemerides from telemetry. The Tracking and Data Relay Satellite System (TDRSS) satellites are often used for GEO calibration. Alternatively, access to the SSN special perturbations state vector catalog [55], containing accurate ephemerides and their covariances, would allow for metric assessment on a range of RSOs.

2. *Lowering the SNR cutoff through improved cosmic ray rejection:* Given that NEOSSat had success imaging in the presence of numerous cosmic ray hits with few false positives, the SNR_{cut} used in routine tasking could be lowered from 4.3 to around 3.0 providing that a strict consistent integrated signal criteria is enforced on detected RSOs. As cosmic ray hits may appear in a common location during imaging stacking the odds that they have a consistent signal are minimal. Such a criteria would allow for more imagery to be acquired by NEOSSat when orbiting near the SAA.

3. Orbit determination studies could be performed from HEOSS observations. The quality of orbits resulting from extended Kalman filtered HEOSS observations could be compared to known orbits and used to determine the quantity of observations, the binning mode required, and establish the frequency of tasking needed to ensure accurate orbital data can be consistently derived from HEOSS imagery.

4. As engineering improvement for future space telescope missions with similar hardware would be to ensure the athermal design of the telescope payload, making the focus constant with changes in bus temperature. A static focus level would allow a precise determination of the optical point spread function. This would enable for better star streak detection and subtraction, leading to improved astrometry and less observation corruption from residual star signatures in RSO centroiding. It would also allow for more photometric accuracy, but more importantly better

SNR cutoff modelling, as the expected signature of an RSO would not be decimated by a varying PSF.

Furthermore, a stable focus level would give a fixed PSF from image to image, known a-priori before signature detection. Also available from NEOSSat telemetry is the ACDS wander history, computed from minute deviations initiated by the star tracker. This data is recorded in the FITS header of each image for the exposure duration at a frequency of up to 10Hz. Knowing the wander history of a point source from outside the telescope boresight and an accurate model of the PSF, it should be possible to deconvolve the signature of a source to remove the jitter component broadening the effective PSF. This would allow for better centroiding of RSOs and more accurate metrics.

7.3 Ending Statement

This work has shown that the methods developed to automatically process HEOSS imagery are a viable approach to generating high quality SSA observations from space-based optical imagery. Despite the engineering challenges that NEOSSat experienced on orbit, it has been shown here that a space surveillance mission can be conducted on a microsatellite platform and is a contribution to the body of knowledge helping to understand the space environment and ensuring access to space for future generations.

Bibliography

[1] "Orbital Debris Quarterly Newsletter," NASA Orbital Debris Program Office, March 2017.

[2] Vallado, D., *Fundamentals of Astrodynamics and Applications, Second Edition*, Microcosm Press and Kluwer Academic Publishers, 2004.

[3] Flohrer, T., Krag, H., and Klinkrad, H., "Assessment and Categorization of TLE Orbit Errors for the US SSN Catalogue," *Proceedings of the 2008 AMOS Technical Conference*, Maui Economic Development Board, Inc., Kihei, Maui, HI, 2008.

[4] Montenbruck, O. and Gill, E., *Satellite Orbits: Models, Methods and Applications*, Springer Science and Business Media, 2012.

[5] Vallado, D., Crawford, P., Hujsak, R., and Kelso, T., "Revisiting Spacetrack Report number 3: Rev 2," *AIAA/AAS Astrodynamics Specialist Conference*, No. AIAA 2006-6753-Rev2, AAS/AIAA, Keystone, CO, 2006.

[6] Hoots, F., Schumacher Jr., P., and Glover, R., "History of Analytical Orbit Modeling in the U. S. Space Surveillance System," *Journal of Guidance, Control, and Dynamics*, Vol. 27, No. 2, 2004.

[7] Lambert, J. and Kissell, K., "The Early Development of Satellite Characterization Capabilities at the Air Force Laboratories," Maui Economic Development Board, Inc., Kihei, Maui, HI, 2006.

[8] Earl, M. and Racey, T., "Progress Report for the Canadian Automated Small Telescope for Orbital Research (CASTOR) Satellite Tracking Facility," *Proceedings of the 2000 Space Control Conference*, No. STK-255, Lexington, MA, 2000.

[9] Scott, R., Wallace, B., Thorsteinson, S., Levesque, M., Maskell, P., Earle, T., Sabourin, N., and Boone, P., "The Ground Based Optical Space Surveillance System," *Proceedings of the 2012 CASI ASTRO Technical Conference*, Québec, QC, 2012.

[10] "Right ascension and declination as seen from outside the celestial sphere," https://en.wikipedia.org/wiki/Right_ascension#/media/File:Ra _and_dec_on_celestial_sphere.png, Wikimedia Commons, Accessed: 2017-07-06.

[11] "Measurement Formats in ODTK," http://help.agi.com/odtk/index.html, Accessed: 2017-03-31.

[12] Seago, J. and Vallado, D., "The Coordinate Frames of the US Space Object Catalogs," *Proceedings of the 2000 Astrodynamics Specialist Conference*, Denver, CO, 2000.

[13] Stokes, G., VonBraun, C., and Sridharam, R., "The Space Based Visible Program," *MIT Lincoln Laboratory Journal*, Vol. 11, No. 2, 1998.

[14] Colarco, R., "Space Surveillance Network Sensor Development, Modification, and Sustainment Programs," *Proceedings of the 2009 AMOS Technical Conference*, Maui Economic Development Board, Inc., Kihei, Maui, HI, 2009.

[15] Maskell, P. and Oram, L., "Sapphire: Canada's Answer to Space-Based Surveillance of Orbital Objects," Maui Economic Development Board, Inc., Kihei, Maui, HI, 2008.

[16] Wallace, B., Pinkney, F., Scott, R., Spaans, A., Bédard, D., Rody, J., Lévesque, M., Buteau, S., Burrell, D., and Hildebrand, S., "The High Earth Orbit Space Surveillance Mission," *Proceedings of the 55th International Astronautical Congress of the International Astronautical Federation (IAF)*, American Institute of Aeronautics and Astronautics, Vancouver, BC, 2004.

[17] Wallace, B., Scott, R., and Spaans, A., "The DRDC Ottawa Space Surveillance Observatory," *Proceedings of the 2007 AMOS Technical Conference*, Maui Economic Development Board, Inc., Kihei, Maui, HI, 2007.

[18] Harvey, W. and Morris, T., "NEOSSat : A Collaborative Microsatellite Project for Space Based Object Detection," *Proceedings 22nd annual AIAA/USU Conference on Small Satellites*, Logan, UT, 2008.

[19] Walker, G., Matthews, J. ., Kuschnig, R. ., and Johnson, R., "The MOST Astroseismology Mission: Ultraprecise Photometry from Space," *Publications of the Astronomical Society of the Pacific*, Vol. 115, No. 1023-1035, September 2003.

[20] "NEOSSat (Near-Earth Object Surveillance Satellite) Spacecraft Description," https://directory.eoportal.org/web/eoportal/satellite-missions/n/neossat, [Online; accessed 17-Jun-2017].

[21] Bédard, D., Wallace, B., Scott, R., Thorsteinson, S., Harvey, W., Tafazoli, S., Fortin, M., Matthews, J., Kuschnig, R., and Rowe, J., "Risk Reduction Activities for the Near-Earth Object Surveillance Satellite Project," *Proceedings of the 2006 AMOS Technical Conference*, Maui Economic Development Board, Inc., Kihei, Maui, HI, 2006.

[22] *E2V CCD 47-20 product specification sheet*.

[23] Wallace, B., Scott, R., Sale, M., Hildebrand, A., and Cardinal, R., "The Near Earth Object Surveillance Satellite: Mission status and CCD evolution after 18 months on-orbit," *Proceedings of the 2014 AMOS Technical Conference*, Maui Economic Development Board, Inc., Kihei, Maui, HI, 2014.

[24] Thorsteinson, S., Wallace, B., and Scott, R., "NEOSSat: Microsatellite based Space Situational Awareness," *Proceedings of the 2015 AAS Guidance, Navigation and Control Conference*, American Astronautical Society, Breckonridge, CO, 2015.

[25] Landolt, A., "UBVRI Photometric Standard Stars in the Magnitude Range of 11.5 to 16.0 Around the Celestial Equator," *Astronomical Journal*, Vol. 104, No. 1, 1992.

[26] Hansen, J., *Wide Field of View Satellite Tracking*, Master's thesis, Royal Military College of Canada, August 2000.

[27] van Ginkel, M., Hendriks, C. L., and van Vliet, L. J., "A short introduction to the Radon and Hough transforms and how they relate to each other," *Quantitative Imaging Group, Imaging Science & Technology Department, TU Delft*, 2004.

[28] Scott, R. and Wallace, B., "Satellite characterization using small aperture instruments at DRDC Ottawa," *Proceedings of the 2008 AMOS Technical Conference*, Maui Economic Development Board, Inc., Kihei, Maui, HI, 2008.

[29] Lévesque, M. and Buteau, S., "Image processing technique for automatic detection of satellite streaks," Tech. Rep. DRDC Valcartier TR 2005-386, Defence Research & Development Canada, Valcartier, Québec, 2007.

[30] Lévesque, M., "Detection of Artificial Satellites in Images Acquired in Track Rate Mode," Maui Economic Development Board, Inc., Kihei, Maui, HI, 2011.

[31] Koblick, D., Goldsmith, A., Klug, M., Mangus, P., Flewelling, B., Jah, M., Shanks, J., Piña, R., Stauch, J., and Baldwin, J., "Ground Optical

Signal Processing Architecture for Contributing Space-Based SSA Sensor Data," *Proceedings of the 2010 AMOS Technical Conference*, Maui Economic Development Board, Inc., Kihei, Maui, HI, 2014.

[32] Heirtzler, J. R., Allen, J. H., and Wilkinson, D. C., "Ever-present South Atlantic Anomaly damages spacecraft," *EOS, Transactions American Geophysical Union*, Vol. 83, No. 15, 2002, pp. 165–169.

[33] Sharma, J., von Braun, C., and Gaposchkin, E., "SBV Data Reduction," *Proceedings of the 1997 Space Control Conference*, Vol. 2, Lexington, MA, 25-27 March 1997.

[34] Opar, T., "SBV Data Collections in Support of Space Control," *Proceedings of the 1997 Space Control Conference*, Vol. 1, Lexington, MA, 25-27 March 1997.

[35] Windhorst, R., Franklin, B., and Neuschaefer, W., "Removing Cosmic-Ray Hits from Multiorbit HST Wide Field Camera Images," *Publications of the Astronomical Society of the Pacific*, Vol. 106, No. 798-806, July 1994.

[36] Scott, R., Wallace, B., and Bédard, D., "Space-Based Observations of Satellites from the MOST Microsatellite," Tech. Rep. DRDC Ottawa TR 2006-199, Defence Research & Development Canada, Ottawa, ON, 2006.

[37] Vrba, F., Fliegel, H., and Warner, L., "Optical Brightness Measurements of GPS Block II, IIA, and IIR Satellites," *Proceedings of the 2003 AMOS Technical Conference*, Maui Economic Development Board, Inc., Kihei, Maui, HI, 2003.

[38] von Braun, C., Sharma, J., and Gaposchkin, E., "SBV Metric Accuracy," *Proceedings of the 1997 Space Control Conference*, Vol. 2, Lexington, MA, 25-27 March 1997.

[39] Williams, J. and McCue, G., "An analysis of satellite optical characteristics data," *Planetary and Space Science*, Vol. 14, No. 9, September 1996.

[40] Hejduk, M., "Catalogue-Wide Satellite Photometric Behavior Paradigms," *Proceedings of the 2010 AMOS Technical Conference*, Maui Economic Development Board, Inc., Kihei, Maui, HI, 2010.

[41] Sydney, P., Africano, P., and Kelecy, T., "High Precision Satellite Astrometry and Photometry," *Proceedings of the 2013 AMOS Technical Conference*, Maui Economic Development Board, Inc., Kihei, Maui, HI, 20043.

[42] Hejduk, M., Lambert, J., Williams, C., and Lambour, R., "Satellite Detectability Modeling for Optical Sensors," *Proceedings of the 2004 AMOS Technical Conference*, Maui Economic Development Board, Inc., Kihei, Maui, HI, 2004.

[43] Lévesque, M., "Image and processing models for satellite detection in images acquired by Space-based Surveillance-of-Space sensors," Tech. Rep. DRDC Valcartier TR 2009-095, Defence Research & Development Canada, Valcartier, Québec, 2009.

[44] Pence, W., Chiappetti, L., Page, C., Shaw, R., and Stobie, E., "Definition of the Flexible Image Transport System (FITS), version 3.0," *Astronomy and Astrophysics*, Vol. 524, 2010.

[45] Stöveken, E. and Schildknecht, T., "Proceedings of the 4th European Conference on Space Debris," *Proceedings of the 2015 AAS Guidance, Navigation and Control Conference*, No. ESA SP-587, Darmstadt, Germany, 2005, pp. 637–640.

[46] "Space Track SSN Data Repository," www.space-track.org, [Online; accessed 20-May-2017].

[47] Zacharias, N., "The Third USNO CCD Astrograph Catalog," http://tdc-www.harvard.edu/catalogs/ucac3.html, 2009, [Online; accessed 16-Feb-2017].

[48] Zacharias, N., "The USNO CCD Astrograph Catalog (UCAC) Project and Beyond," *Small Telescopes in the New Millennium II. The Telescopes We Use.*, edited by T. Oswald, Kluwer Acad. Publ, 2003.

[49] Denny, B., "PinPoint Astrometric Engine 6.1," http://pinpoint.dc3.com/, [Online; accessed 30-May-2017].

[50] Greisen, E. W. and Calabretta, M. R., "Representations of world coordinates in FITS," *Astronomy & Astrophysics*, Vol. 395, No. 3, 2002, pp. 1061–1075.

[51] Price, R., "A Letter from Richard Price, D. D. F. R. S. to Benjamin Franklin, L L. D. F. R. S. on the Effect of the Aberration of Light on the Time of a Transit of Venus Over the Sun," *Philosophical Transactions (1683-1775)*, Vol. 60, 1770, pp. 536–540.

[52] Siedelmann, P. e., *Explanatory Supplement to the Astronomical Almanac*, University Science Books, 2005.

[53] "National Geodedic Service webpage," https://www.ngs.noaa.gov/orbits/orbit_data.shtml, [Online; accessed 1-May-2017].

[54] Schildknecht, T., Musci, R., Flury, W., Kuusela, J., de Leon, J., and Dominguez Palmero, L. D. F., "Optical Observations of Space Debris in High-Altitude Orbits," *4th European Conference on Space Debris*, Vol. 587 of *ESA Special Publication*, Aug. 2005, p. 113.

[55] Schumacher, P. and Hoots, F. R., "Evolution of the NAVSPACECOM Catalog Processing System Using Special Perturbations," *Proceedigns of the Fourth US/Russian Space Surveillance Workshop, US Naval Observatory, Washington, DC*, 2000.

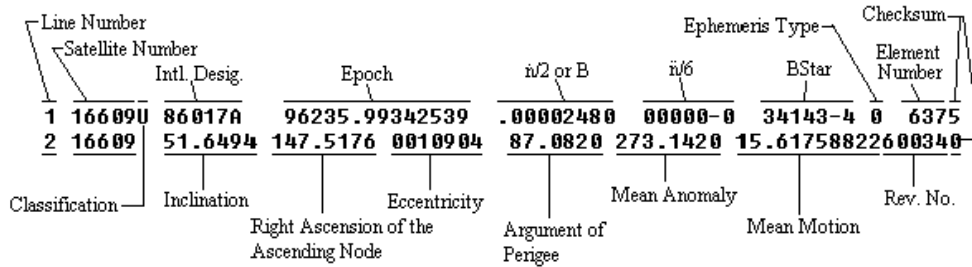# Appendices

A Appendix A: Two Line Element Sets

Figure A.1: A sample TLE with its terms explained.

Figure A.1 shows a sample TLE with the terms named denoting the column based formatting. The coordinate system is True Equator Mean Equinox, providing mean elements, unlike conventional osculating elements. The individual terms are defined as follows:

- The Satellite Number is issued in increasing numeric order for every new RSO detected, whether from a launch, payload separation, breakup event, or newly discovered unknown object.
- The International Designator lists the year and DOY of the RSO's launch, with a separate letter (or two) for each RSO associated with that launch.
- The Epoch, listed in YYDDD and decimal fraction of the day, is the time the RSO can be found at the mean anomaly listed in the TLE.
- The $\dot{n}/2$ term is the mean motion rate, divided by two represented in revolutions per day^2. This is mainly analogous to drag influences.
- The $\ddot{n}/6$ term is the second derivative of the mean motion, divided by 6. This is usually set to zero for SSN produces TLEs.

- The BStar term is a further drag analogue, which combined with the $\dot{n}/2$ term provides two independent parameters to model atmospheric drag and solar radiation pressure.
- The Element Number is the historical release number of the TLE for this RSO.
- The Inclination and RAAN and Argument of Perigee are the standard classical orbital elements in degrees.
- The Eccentricity is the standard classical orbital element.
- The Mean Motion is the number of orbits the RSO completes in a 24 hour period from which the semi-major axis can be calculated.
- The Mean Anomaly is similar to the true anomaly but adjusted so that the RSO changes mean anomaly at a constant rate throughout its orbit, rather than at the varying rate of the true anomaly which varies faster at perigee and slower at apogee.
- The Revolution Number is how many orbits the RSO has completed since launch (estimated if not known).